POWER AMPLIFIERS AND ANTENNAS FOR IMPLANTABLE BIOMEDICAL TRANSCEIVERS

Power Amplifiers and Antennas for Implantable Biomedical Transceivers

By

Samar M. Abdelsayed

B. Eng., Cairo University, July 2003

A THESIS SUBMITTED TO THE SCHOOL OF GRADUATE STUDIES IN PARTIAL FULFILLMENT OF THE REQUIREMENTS FOR THE DEGREE MASTER OF APPLIED SCIENCE

McMaster University
Hamilton, Ontario, Canada

MASTER OF APPLIED SCIENCE (2006) McMaster University
(Electrical and Computer Engineering) Hamilton, Ontario

TITLE: Power Amplifiers and Antennas for Implantable Biomedical Transceivers

AUTHOR: Samar M. Abdelsayed, B. Eng. (Electronics and Communications Eng., Cairo University, Egypt)

SUPERVISORS: Profs. M. Jamal Deen and Natalia K. Nikolova

NUMBER OF PAGES: XXIV, 130

Abstract

Recently, there has been a strong trend in medicine to use implanted electronic devices for diagnostic and/or therapeutic purposes. These devices usually involve a one- or two-way communication link, allowing communication with the implant. One revolutionary implanted system that was recently launched into the healthcare market is the wireless imaging capsule for monitoring the gastrointestinal tract. Among the application-specific design challenges of such a wireless system are the severe constraints on low power and on small physical size. Besides, the allowed power levels of signals due to in-body radiating devices are restricted to very low values due to human safety concerns. To meet the requirements of such a wireless system, highly efficient, small-size, low-power transmitting radio frequency (RF) blocks are needed.

This thesis focuses on the design, implementation and measurements of the last two blocks in the transmitter, namely the antenna and the power amplifier (PA). Three PA circuits have been designed and measured, all of class AB topology. The first two PAs operate at 2.4 GHz, while the third is designed for 405-MHz operation. All designs are fully integrated and realized in a standard mixed-signal 0.18 μm complementary metal-oxide-semiconductor (CMOS) process. Measurement results show that at a supply voltage of 1.4 V, the circuits have a maximum drain efficiency of 32% and 40.7% for the 2.4-GHz and the 405-MHz designs, respectively, while providing an output power of 7.2 and 8 dBm to the load. These results greatly outperform similar designs in the literature, proving that class AB PAs, if properly designed, are well-suited for low-power biotelemetry application.

A simple layout design approach was developed to minimize the parasitic effects of on-silicon interconnections that cause significant degradation in the performance of RF integrated circuits (RF ICs). This approach was used to design the layouts of the three PA circuits presented in this work, and the approach was tested on a low-noise amplifier (LNA) operating at 5 GHz, since at such a high frequency the parasitics become more pronounced. Measurements on the LNA circuit show good agreement with simulations.

Thus, next to allowing for optimized circuit performance, this approach can shorten the design time of RF ICs by providing very good predictions of performance characteristics.

The last part of this thesis deals with the analysis and design of efficient in-body antennas. A study of the use of loop antennas in medical implants was conducted. Simulations and measurements have been used to characterize the radiation performance of loop antennas in terms of their radiation resistance, transmitting bandwidth and biocompatibility. At 405 MHz, the antenna has proven to be efficient in the dissipative biological tissues, to have a wide transmitting bandwidth, and a specific absorption rate (SAR) distribution that is well below the safety limits. To further verify its suitability for in-body operation, a miniature loop antenna was fabricated and measured at 405 MHz and 2.4 GHz. For measurement purposes, two body simulating chemical solutions were prepared in-house to provide the necessary radiation environment. Measurements show that small loop antennas are well matched in the medium and are thus good in-body radiators.

To the glory of His holy name, my Lord and my Shepherd, Jesus Christ.

Acknowledgements

I want to take this opportunity to express my sincere gratitude to several people who have contributed much to me and to this work during the past two years and that have taught me how to improve my technical and intellectual skills.

I would like to start by sincerely thanking my senior supervisor, Prof. Jamal Deen. I would like to thank him for giving me this opportunity to engage in such an interesting research topic and go through this treasured experience. More importantly, I would like to thank him for teaching me how to reason and be creative in research, greatly improving my mind as an engineer. Prof. Deen's high expectations and guidance have always steered me to do my best to become the best researcher I can be.

I would also want to express my sincere gratitude and appreciation to my co-supervisor, Prof. Natalia Nikolova for making me feel that she is always available for support, for being patient in guiding me all through the period of my research and experiments, and for teaching me how to better document and communicate my research work.

I would like to thank both of my supervisors for continuously providing me with fruitful comments, for guiding this research work in the right direction and for never ceasing to guide me to improve my technical weaknesses. Both of them contributed greatly to my personal growth. In fact, it was a great honor and a pleasurable experience to work under their supervision.

I am also grateful to Prof. Mohamed Bakr and Prof. Chih-Hung Chen for being members on my committee and for being outstanding mentors of two interesting courses I took towards the fulfillment of the program requirements. The two courses have added a lot to my theoretical and practical foundation, which greatly helped in conducting this research.

I would also want to thank NSERC, RIM, the Canada Research Chair Program and Micronet for funding this research, and the Canadian Microelectronics Corporation (CMC) for arranging the fabrication.

I also want to give special thanks to my research colleagues in the Microelectronics, the Computational Electromagnetics and the Simulation Optimization Systems Research laboratories for their technical input in simulations, measurements and equipments set-up, including – but not limited to – Ognian Marinov, Sasan Naseh, Rizwan Murji, Wei Ngan, Juan-Carlos Ranuarez, Hamed Mazhab Jafari, Feng Li, Waleed Shinwari, Shirook Ali, Ahmed Sayed Mohamed and Peter Basl. Special thanks are also due to Yasaman Ardershirpour and Kareem Shoukri, who gave me a more pleasurable working atmosphere.

I would like to extend my thanks to Todd Hoare, a graduate researcher in the Department of Chemical Engineering at McMaster University for his kind help in the preparation of the tissue-equivalent chemical solutions used in the antenna measurements.

Many thanks are also due to the administrative staff members in the Department of Electrical and Computer Engineering at McMaster University: Cheryl Gies, Helen Jachna, Terry Greenlay and Cosmim Coroiu.

I feel truly indebted to two special friends that I have met on my first day in the program, Tarek Sadek and Samer Rizk. I owe them lots of gratitude for contributing much to me in this transitional period of my life. I also thank them for their valuable help and endless moral and technical support in the duration of the preparation of the thesis.

Deep thanks and appreciation are inevitably due to Munir El-Desouki, my dear friend and colleague. I want to truly express to him how much I am grateful for his endless support and encouragement since the earliest steps in my research. Words are not enough to express my feeling of being fortunate to have such an exceptional research partner and treasured friend worthy of reliance.

Last, but not least, I want to express my heartfelt gratitude to my wonderful family members and friends, here and in Egypt, for continuously being there for me. Special thanks to my father, who never ceased to motivate me in my academic pursuits and to my dear mother, who did nothing but being the greatest mom.

Table of Contents

List of Figures

List of Tables

List of Symbols and Acronyms

Symbols

ω	Frequency in radians
σ	Conductivity
ε_r	Relative permittivity
a	Wire radius
b	Loop radius
BW	Bandwidth
c	Spacing between the turns of a loop antenna
C_{ox}	Oxide capacitance
C_p	Interconnection parasitic capacitance
C_{pad}	Capacitance of chip bonding pads
C_s	Coupling capacitance of spiral inductor
C_{sub}	Parasitic capacitance to the substrate
C_{tun}	Tuning capacitor
E	Electric field
e	Exponential operator
f	Frequency in Hertz
f_{max}	Maximum oscillation frequency
f_{SR}	Self-resonance frequency
f_T	Cutoff frequency
I_{DC}	DC current
I_{dq}	Quiescent current
I_m	Peak current
k	Complex propagation constant
l	Length of metal strip
L_p	Interconnection parasitic inductance
N	Number of turns

N_A	Substrate doping concentration
NF	Noise figure
P_{DC}	DC power
$P_{in,rf}$	RF input power
P_{out}	Output power
$P_{out,rf,}$	RF output power
Q	Quality factor
R_b	Bias resistance
R_D	Drain resistance
R_G	Gate resistance
R_{ohmic}	Ohmic loss resistance
R_{OPT}	Optimum load impedance in power amplifier design
R_p	Interconnection parasitic resistance
R_p	Ohmic loss due to proximity effect
R_s	Ohmic loss due to skin effect
R_S	Source resistance
R_{sub}	Parasitic resistance to the substrate
s	Spacing between metal strips
t	Thickness of metal strip
$\tan\delta$	Loss tangent
t_{ox}	Oxide thickness
V_{BD}	Breakdown voltage
V_{DD}	Supply voltage
V_k	Knee voltage
V_{th}	Threshold voltage
w	Width of metal strip
W/L	Width over length ratio
Y	Admittance
Z_{in}	Input impedance

Z_{rad}	Radiation resistance
α	Attenuation factor
β	Phase constant
γ	Euler's constant
δ	Penetration depth
η_D	Drain efficiency
λ	Wavelength
μ_0	Permeability of free space
π	Pi
ρ	Mass density

Acronyms

AC	Alternating current
ACPR	Adjacent channel power ratio
BiCMOS	Bipolar complementary metal oxide semiconductor
BJT	Bipolar junction transistor
CCD	Charge-coupled devices
CMOS	Complementary metal-oxide-semiconductor
CP	Compression point
DAC	Digital-to-analog converter
DC	Direct current
DGBE	Di-ethylene-glycol butyl ether
EER	Envelope elimination and restoration
EIRP	Effective isotropic radiated power
EM	Electromagnetic
ESD	Electrostatic discharge
FDTD	Finite difference time domain
FoM	Figure-of-merit
FSK	Frequency-shift keying

G	Power gain
GaAs	Gallium arsenide
HBT	Heterojuction bipolar transistor
HRS	High-resistivity silicon
IC	Integrated circuit
IF	Intermediate frequency
IP_3	Third-order intercept point
ISM	Industrial-scientific-medical
ITRS	International technology roadmap for semiconductors
LDD	Lightly doped drain/source
LED	Light emitting diode
LINC	Linearization using nonlinear components
LNA	Low-noise amplifier
LO	Local oscillator
MEMS	Micro-electro-mechanical systems
MICS	Medical implantable communication systems
MIM	Metal-insulator-metal
MOSFET	Metal-oxide-semiconductor field-effect transistor
MRI	Magnetic resonance imaging
NMOS	N-type metal-oxide-semiconductor
NQS	Non-quasi static
PA	Power amplifier
PAE	Power-added efficiency
PMOS	P-type metal-oxide-semiconductor
ULP AMI	Ultra low-power active medical implants
rms	Root mean square
RF	Radio frequency
RFC	Radio frequency choke
SAR	Specific absorption rate

SiGe	Silicon-germanium
SOS	Silicon-on-saphire
S-parameters	Scattering parameters
VCO	Voltage-controlled oscillator
VNA	Vector network analyzer
VSWR	Voltage standing wave ratio
WCE	Wireless capsule endoscopy
Z-parameters	Impedance parameters

CHAPTER 1

Introduction: Biotelemetry Implants

Biomedical implantable electronics, fluidic and mechanical systems (micro-electromechanical systems – MEMS) are becoming increasingly important in monitoring and treatment of specific ailments. One example of such an electronic system is the pacemaker used to provide electrical pulses to regularize heart beats. Another example is the MEMS-based system that is used to monitor the blood sugar level in diabetic patients and to deliver insulin as needed. In this work, we propose to develop components that go into an opto-electronic, wireless implantable system to screen for medical problems associated with the gastrointestinal tract, primarily because it is one of the most difficult areas to diagnose accurately in a non-invasive manner. More specifically, we concentrate on developing efficient, low-power, compact power amplifiers and antennas targeted for the transmitter subsystem of this biotelemetry implant for monitoring the gastrointestinal tract.

1.1 IMPLANTABLE ELECTRONIC BIOMEDICAL SYSTEMS

Health care is one of the many areas on which the evolution of the electronic and micro-electromechanical technologies has had a great impact. Biomedical engineering scientists not only used these technologies to provide hospitals with high technology equipment, but they also began to explore the possibility of applying these technologies in body-embedded electronic devices. Biomedical implanted devices have found wide application in the medical field, including regulating body functions, stimulating nerves and treating various diseases. Figure 1.1 shows the different locations of the human body where biomedical implants can find applications [1].

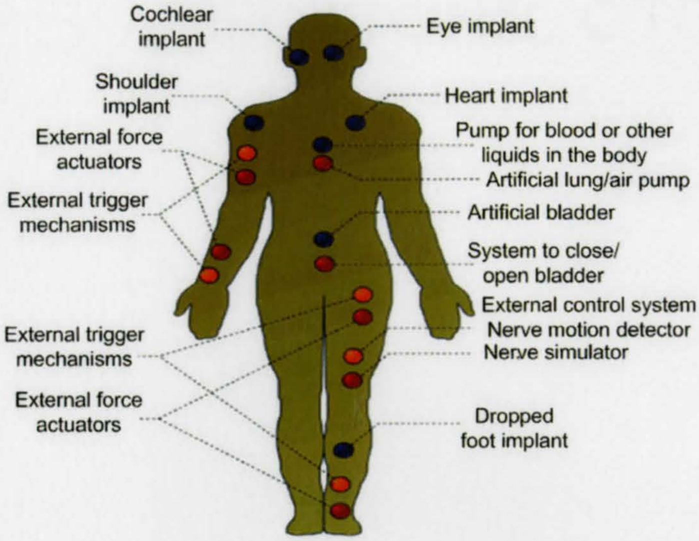

Fig. 1. 1. Various body locations where implantable electronic devices can find applications [1].

The healthcare community has even recently benefited from the newly developed biomedical implantable systems that involve a one or two-way wireless communication link, allowing communication with the implant. The success of these biotelemetry systems is a result of the remarkable advancement in the emerging submicron complementary metal-oxide-semiconductor (CMOS) processes and the development of new radio frequency (RF) circuit topologies. These two trends allowed for efficient, miniature, low-power RF transceivers that are compatible with the stringent requirements of these biomedical applications. Examples of biomedical implants that involve a telemetry system are: cardiac pacemakers, hearing aids, defibrillators, as well as pressure, pH, temperature or blood glucose sensors. These implanted devices present a true breakthrough in medical therapy and diagnosis and have found an obvious appeal to patients and physicians, since they present a cost-effective and a patient-friendly alternative to the more painful, uncomfortable, time consuming and expensive methods for diagnosis or treatment.

Biomedical implantable devices with wireless capabilities were previously limited to locations close to the patient's skin; but they are now placed deeper inside the human body reaching even internal organs. The deeper the point inside the body from which the implant radiates, the more pronounced become the challenges faced in the design of its RF subsystem. One recent revolutionary medical implant with RF capabilities is the wireless capsule endoscopy (WCE) system intended for the diagnosis of the small-intestinal disorders. In this system, the implant operates deep from the inside of the human abdomen. The full system will be presented in the next section, highlighting its main components, intended functionality and the available commercial products.

1.2 DIAGNOSTIC GASTROINTESTINAL WIRELESS CAPSULE ENDOSCOPE

1.2.1 Medical Background

The medical information given in this section is based on references [2-5].

It is generally agreed by medical practitioners that disorders in the small intestine are among the most difficult to diagnose gastrointestinal disorders. The small intestine is about five meters long and has many complex loops; hence it is anatomically very difficult to access and to monitor. Crohn's disease (gut/mucosa inflammation), benign and malignant small intestine tumors and bleeding abnormalities arising from obscure sources in the small intestine (obscure gastrointestinal bleeding) are the most common, but hard to diagnose small intestine disorders.

Push enteroscopy, which uses a camera attached to a flexible endoscope, small-bowel follow through (SBFT), endoscopic ultrasound, radiological imaging (X-rays) or even surgeries are used for examining the small intestinal tract for identifying its disorders. However, these conventional diagnostic techniques have many complications and limitations. Push enteroscopy and SBFT are painful to patients and can only reach the upper third of the small intestine. X-rays and ultrasound have the limitation of exposing the patient to large radiation doses. To the patients, all the above methods are uncomfortable, expensive and require hospitalization. To the physicians, they provide limited diagnostic results and have low diagnostic yield. Thus, they usually have to follow a large number of gastrointestinal examination procedures before they can make a conclusive diagnosis. So, there was an urgent clinical need for an alternative technology before the WCE was introduced to the healthcare market.

The WCE technology relies on an encapsulated miniature video camera that is swallowed by the patient after an eight-hour period of fasting. Along the capsule's journey, it takes pictures of the human's digestive tract (Fig. 1.2). It continuously transmits these images through an RF link to a receiver close to the patient's skin. These images are then observed by a gastroenterologist and further medical actions are taken according to the case. The capsule is carried by the natural peristalsis (contraction and relaxation) of the small intestine through the gastrointestinal tract. It is disposable and the passage time is 8-73 hours.

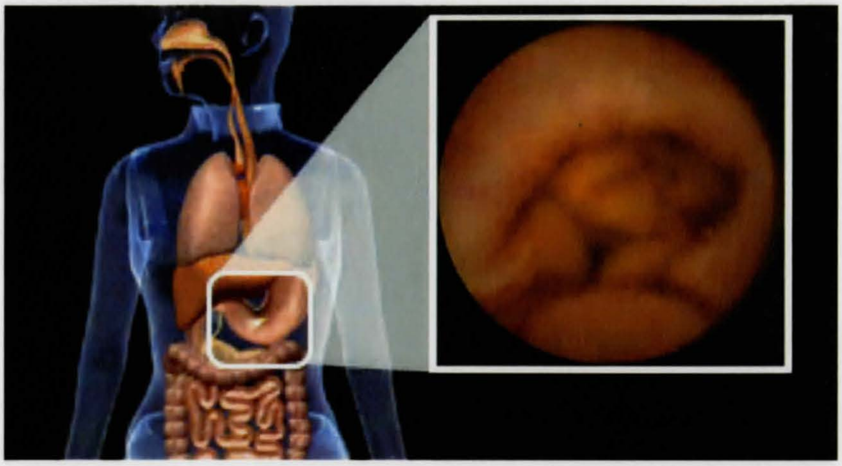

Fig. 1. 2. Monitoring the gastrointestinal tract using the WCE technology (modified from [6]).

Compared to the traditional diagnostic methods, the WCE is easy to use, monitors the entire small intestine, is painless and comfortable to patients, and it features a high diagnostic yield. But, as any medical technique, the WCE has its own medical risks and complications. The main complications associated with the WCE system are: imaging or transmission failure due to defective components, delayed or failed natural excretion due to narrowing or blockage in the small intestine, poor visualization, discontinuity of the operation before the pill completes its journey due to limited supply power and interference with other implanted RF devices like cardiac pacemakers.

1.2.2 System Components, Functionality and Market Overview

The WCE system consists of three key subsystems: an imaging capsule, a wireless data recorder and a computer workstation. The fundamental system requirements are: high image quality, reliable data transmission, cost effectiveness and minimal medical complications. The WCE system is currently manufactured by very few companies. The two leading ones are: the Israeli Given Imaging Ltd. and the Japanese RF System Lab.

The complete system is shown in Fig. 1.3, as implemented by (a) RF System Lab [7] and (b) Given Imaging Ltd. [4].

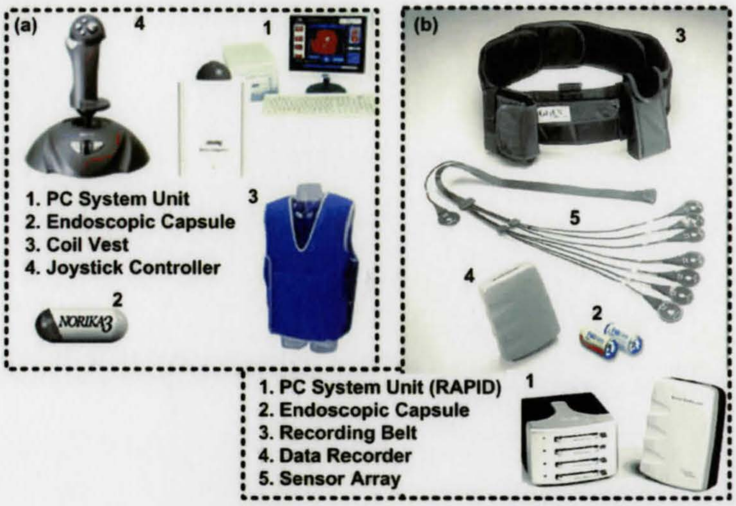

Fig. 1. 3. Main components of the WCE system, as implemented by (a) RF System Lab [7] and (b) Given Imaging Ltd. [4].

The main, revolutionary subsystem of the WCE system is the swallowable camera capsule with its RF and imaging capabilities. The intended system functionalities are:

- remote imaging,
- wireless data transmission,
- data processing,
- tracking capability (localization),
- locomotion facility (stopping or steering),
- therapeutic capabilities (localized medication delivery, laser radiation),
- and biopsy (tissue sampling).

The whole subsystem is to be encapsulated in a pill-size case made of a biocompatible material that resists the digestive acids. The main subcomponents of the system are:

- the image capturing components: image sensors or microchip camera, light emitting diodes (LEDs) and camera lens,
- an energy source – miniature batteries or an inductive coil in the case of inductive power coupling,
- and the RF components: RF transceiver and antenna.

Table 1.1 and Fig. 1.4 show the main characteristics of Given Imaging's PillCam (previously known as M2A) and RF System Lab's Norika3 [7].

As can be seen from the comparison given in Table 1.1, the main differences between the two pills are the power supply mechanism and the implemented imaging technology. Power is supplied to PillCam using two silver-oxide batteries, while Norika3 is powered by external power coupling. Using power coupling for providing the power to the pill, Norika3's designers were able to save the battery space to implement added functionality. Their pill has two tanks that can be used for drug delivery, laser radiation or tissue sampling. In addition, it provides the locomotion facility to the physician, who can stop or steer the pill inside the human body. With regard to the imaging technology, PillCam uses the CMOS technology, while Norika3 uses the charge-coupled device (CCD) technology. The CCD technology allows for saving space, since the step of image processing can be done separately from that of image capturing and hence, can be implemented in one of the other subsystems outside the body (recorder or computer workstation). On the other hand, the CMOS imaging technology is known to provide lower power consumption, is less expensive and allows for implementations in a smaller area. However, the main advantage of using a CMOS image sensor is the full integration of the sensor, the RF transceiver and the processor on a single chip. This reduces the area and cost significantly.

Table 1. 1. System characteristics of PillCam and Norika3 [7].

Characteristic	**PillCam (M2A) by Given Imaging Ltd.**	**Norika3 by RF System Lab**
Power Supply	2 silver-oxide batteries	external power coupling
Image Transmission Rate	2 images/sec	30 images/sec
Size	11 mm x 27 mm	9 mm x 23 mm
Image Sensor Technology	CMOS	CCD
Camera Flash	white LEDs	4 colored LEDs
Capsule Enclosure	plastic case	resin case

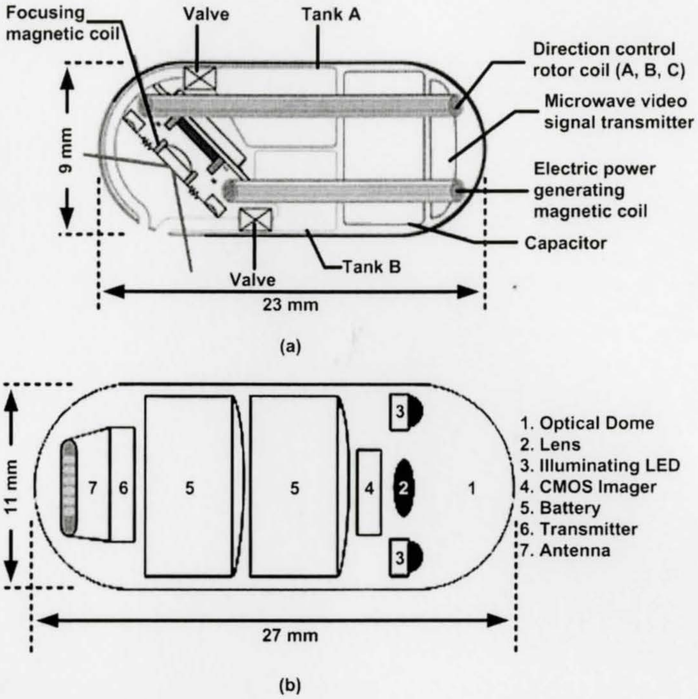

Fig. 1. 4. (a) Norika3 and (b) Pillcam imaging pills [7].

The second subsystem of the WCE system is the wireless data recorder. It has the main functionality of receiving the captured images and storing them. It mainly consists of an antenna (or antenna array) and a highly sensitive RF receiver. For additional control capabilities, a two-way RF communication link can be provided. The data recorder is implemented in Norika3's system in the form of a vest that is worn by the patient and is equipped with an additional power coupling coil for supplying power to the pill. PillCam's recorder is contained in a handheld device that is mounted on a belt that is wound around the patient's waist (refer to Fig. 1.3).

The last subsystem of the WCE system is the computer workstation or the base station. It presents the end-user interface and provides post-processing to the captured images. The software should allow the physician to browse the individual images or watch a constructed streaming video. RF System Lab provides a computer workstation with a joystick controller for focusing, light and posture control.

1.3 MOTIVATION

The research described in this thesis was conducted as part of a larger project on the design, implementation and testing of a prototype transceiver system for the imaging capsule. The work in this thesis focuses mainly on the design, implementation and testing of the last two elements of the embedded transmitter, namely the power amplifier (PA) and the antenna.

As will be discussed in Chapter 2, there are two candidate frequency bands for operating biotelemetry systems, the 402-405 MHz and the 2.4-GHz bands. Since it is still debatable which frequency band is more suitable, this work attempts to answer this question and has three main goals:

- designing and testing low-power highly-efficient PAs operating at both frequencies,
- choosing an antenna type that is suitable for the application and analytically and experimentally determining its suitability for this application,
- and based on the performance of the PA circuits and the antenna at both frequencies, a final goal of this work is to recommend a frequency for the transmitter system operation.

Among all the transceiver blocks, the PA is known to dominate the power consumption budget. Thus, its efficiency impacts directly on the efficiency of the whole transmitter. According to the system requirements discussed in following chapter, the PA should satisfy the following specifications:

- It should be fully integrated in a standard CMOS process with all its passive components on the same chip.
- It should be highly efficient.
- It must operate at low supply voltages.
- The output power level it delivers to the antenna should be in the range of few milliwatts. The use of a class AB PA is investigated in this work.

As for the antenna, it should have the following specifications.

- The radiation leaving the antenna should be safe for the human body by complying with the safety limits stated in the standards.
- It should be of compact size.
- It should have high radiation efficiency.

Unlike in free-space, research studies have shown that small loop antennas are very efficient when radiating in a lossy medium [76]. Thus, in this work, the use of loop antennas for biomedical implants will be investigated through analytical design and experimental set-up.

In silicon-based circuits, layout parasitics at RF present a serious issue and if not properly taken into account in the layout design stage, they may degrade the performance of the circuits significantly. Hence, out of the need for a layout design approach that ensures good performance of CMOS RF integrated circuits (ICs), one other goal of this work was to develop a systematic layout design approach that helps reducing and predicting layout-related losses in CMOS RF ICs.

1.4 THESIS ORGANIZATION

This thesis is divided into nine chapters and is organized as follows. Chapter 2 presents a brief preview of the challenges met and the decisions involved in designing transceivers for biomedical implanted systems. In Chapter 3, the modern submicron CMOS process is explored as the implementation technology for RF ICs.

In Chapter 4, a parasitics-aware layout design technique is proposed for the layout of CMOS RF ICs. This technique was used in the layout design stage of the PA circuits presented in this work. For illustration purpose, this layout design methodology has been applied to a 5-GHz low-noise amplifier (LNA), since at 5 GHz, the layout parasitics become more pronounced.

Chapter 5 presents a concise overview of the PA basics, their performance characteristics and their classes of operation. Chapter 6 presents the designed and implemented prototype PA circuits. Two PAs operating at 2.4 GHz have been implemented and tested, with the second being just a modified version of the first. It is implemented using a thicker top metal layer, hence suffers from less layout parasitics and exhibits better performance. A third PA circuit is designed for 405-MHz operation to cover the second alternative frequency band and is compared to the thick top-metal 2.4-GHz PA. The layouts of the three PA circuits have been designed using the layout design technique presented in Chapter 4. This layout methodology allowed for obtaining high performance PAs and excellent match between measurements and simulations.

Chapter 7 presents a compact collection of topics related to the in-body radiation problem. The chapter involves characterizing the human body as the medium for RF wave propagation. It also introduces the reader to the regulatory systems concerned with radiation safety, the most popular safety standards and the regulations related to in-body radiation from biomedical implants. A discussion of the assessment of the in-body radiation problem using both numerical simulations and experiments is also presented (electromagnetic or EM dosimetry). The chapter also briefly discusses the concept of modeling the human body for EM dosimetry.

Chapter 8 presents the analytical and numerical investigation of the use of small wire loop antennas for biomedical implants. The loop is characterized at 405 MHz, in terms of its radiation resistance, its safety compliance and its radiation bandwidth. The chapter also presents measurements of the return loss of a small fabricated loop antenna at 2.4 GHz and 405 MHz. These measurements are used to calculate the loop radiation resistance to prove the suitability of loop antennas for biotelemetry implants.

Finally, Chapter 9 lists the important conclusions and recommendations resulting from the work presented in this thesis. The chapter presents and discusses possible further research in power amplifiers and antennas for biotelemetry implanted systems.

CHAPTER 2

Transceivers for Biotelemetry Implants

One of the major challenges in building the WCE system is the design of the in-body RF transceiver of the imaging pill. In the design of any transceiver system, the first step is defining the application-related specifications and constraints – linearity, available bandwidth, data rate, power budget, size, cost, allowable transmit power, etc. The design then involves choosing the proper frequency of operation, the implementation technology, the modulation scheme and the transmitter/receiver architectures. The goal of this chapter is to introduce the reader to the specifications and design challenges of implanted RF transceivers.

For wireless communications systems used in biomedical implants, the required range of operation is only few tens of centimeters depending on the patient's body size and structure. Due to safety issues and spectral compliance concerns, the allowable power level transmitted from the implant is in the order of milliwatts, -2 to 10 dBm. With the above characteristics, biomedical telemetry implants are classified as ultra low-power, short-range devices. These devices operate at relatively low data rates, have low duty cycles, relaxed bandwidth and linearity requirements, and they require simple network protocols. The deeper the implant, the more challenging is the transceiver design and the more sophisticated is the system design and test. Transceivers for biomedical implants must be small, of ultra low-power consumption and their radiation amounts should be safe for the human body.

Section 2.1 presents the design challenges met in designing these transceiver systems and Sections 2.2 to 2.4 discuss possible choices of their frequency of operation, implementation technology and architecture.

2.1 DESIGN CHALLENGES

2.1.1 Size and Power Constraints

The RF transceiver, like all the remaining subsystems of the WCE system, is powered from a very limited source and should be of miniature size. To realize an ultra-small, ultra low-power RF transceiver system, the following has to be considered:

- Simple transceiver architecture.
- RF blocks that are fully integrated in a standard CMOS process.
- A simple constant-envelope modulation scheme with relaxed linearity performance and hence more efficient transmitting amplifiers.
- Modified circuit topologies with ultra low-power consumption and a reduced number of lossy large-area on-chip passive elements.
- Applying power management techniques in the RF transmitter.
- Designing high-performance, power-efficient RF components with ultra low-power consumption that can operate at low supply voltages.
- Small, low-loss and highly-efficient antennas.

2.1.2 Human body as a Medium for RF Wave Propagation

This communication system differs from other communication systems mainly in the complex nature of its radiation environment, which imposes additional challenges.

A challenge that is of utmost importance is characterizing the human body as a medium for EM wave propagation. The body is known to have more than 32 tissue types with a very complicated tissue structure. Thus, it presents an extremely complex radiation environment, which is difficult to model accurately. This can be seen in Fig. 2.1 for a cross-section of the human abdomen [8]. Consequently, the antenna should be designed to operate in this complex, lossy environment and its radiation characteristics should be developed numerically and experimentally in a human-like situation.

A precise calculation of the link power budget and the allowable power levels is another important challenge. The biological tissues are known to be highly dissipative at radio frequencies, so high-power signals should be transmitted to have a detectable signal outside the body. However, from safety considerations, the amount of radiation that human tissues can be exposed to is regulated by international committees[1]. Consequently, there is a major design tradeoff in the link characterization and power calculation problem of this application: the signal power should be chosen not too high, so that it does not raise safety concerns, and not too low, so that the signal is strong enough to be detected by the receiver outside the body.

Fig. 2. 1. Cross-section of the human abdomen showing the complexity of its tissue structure [8].

2.2 FREQUENCY OF OPERATION

There are several possible frequency bands at which this system can be operated. A practical choice would be one of the license-free bands allocated for short-range personal communications networks. These are the 902-928 MHz industrial, medical and scientific (ISM) band in North America, the 433 MHz and the 868 MHz ISM bands in Europe, and the 426, 449 and 469 MHz bands in Japan. The 2.4-GHz ISM band used for Bluetooth applications has also proven to be suitable for short-range wireless communications and is thus another good alternative. On the other hand, with the continually widening range of applications of biomedical implants, international frequency allocating organizations have recently considered allocating a specially-dedicated frequency band for biomedical implants communications, which is the 402-405 MHz frequency band. This choice resulted from studies on the possible RF effects on humans and EM interference issues.

This same band has been allocated by the Federal Communication Commission (FCC) in North America and is called the medical implants communication services (MICS) band; and by the European Radio-Communication Commission (ERC) in Europe

---

[1] *Committees that are in charge of developing the human EM safety criteria.*

and is called the ultra low-power active medical implants (ULP AMI) frequency band. Regulations set by the ERC for ULP AMI communications are given in Annex 12 of the ERC/REC 70-03 [9], while regulations set by the FCC can be found for the MICS band in [10]. The technical regulations and the operational rules set by the two organizations are very similar and are summarized in Table 2.1 according to the FCC document [11].

The regulating bodies have set a limit on the effective isotropic radiated power[2] (EIRP) level. The maximum permissible EIRP from biomedical implants operating in the MICS band is 25 μW in free space. This limit is set to prevent the interference of signals radiated by the implanted devices with signals of other services in the same frequency band. In the USA, the services that use the same frequency band are meteorological aids, meteorological satellite, and earth exploration satellite services [12]. The implanted device should not interfere with other stations, whereas it has to receive interference signals from stations dedicated to one of the previously mentioned services.

An important consequence of choosing the MICS band for the WCE system is that only a one-way communications link would be possible from the implant to the outer receiver. Body losses through the human abdomen are estimated to be in the range of 15-18 dB [13]. If the implant is to radiate few milliwatts, the signal power level at the outer receiver will be in the range of microwatts and will hence comply with the regulations. However, due to the high body losses, a signal with an EIRP limited to 25 μW targeting the deep implant will not possibly reach it; it will be dissipated within a few millimeters from the surface of the body. Thus, the communications from the outside to the implant will have to be realized utilizing a different frequency band. So, if only an RF transmitter is sufficient, then the MICS band can be used. Nevertheless, if two-way communications is desirable, then either a 2.4-GHz or a multi-band RF transceiver should be used. PillCam uses the 402-405 MHz MICS frequency band for RF transmission of the

[2] *Effective isotropic radiated power (EIRP) is the equivalent power of a transmitted signal in terms of an isotropic (omnidirectional) radiator. Normally the effective isotropic radiated power equals the product of the transmitter power and the antenna gain. It is expressed as*

$$EIRP = G * P = 10^{(g/10)} * P \quad [\mathrm{W}],$$

where G is the antenna gain, g the antenna gain in dBi, and P is the power in W.

captured images, while Norika3's transceiver is designed to operate in the 2.4-GHz ISM band.

Table 2. 1. Regulations for the biomedical MICS band as given by the FCC [11].

MICS transmitters may not operate with an effective EIRP greater than 25 μW
MICS transmitter emissions are limited to an authorized bandwidth of 300 kHz.
MICS transmitters may transmit any emission type appropriate for communications in this service, but may not be used for voice communications.
MICS transmitters must be tested for emissions and EIRP limit compliance while enclosed in a medium that simulates human body tissue in accordance with FCC-specified procedures.

2.3 Modulation Technique and the Transceiver Architecture

The choice of the modulation scheme and the transceiver architecture depend on the specifications. Given the previously mentioned specifications of biomedical implanted transceiver systems, the most suitable modulation scheme is the constant-envelope frequency shift keying (FSK) modulation technique. At the expense of lower data rates and lower bandwidth, this modulation scheme allows for using low-complexity transceivers and for relaxed linearity requirements. These two characteristics, in turn, greatly reduce the power consumption of the system.

With regard to the choice of the in-body transceiver architecture, the low intermediate frequency (IF) or the direct-conversion (zero-IF) architectures present a more attractive choice than the complex superheterodyne architecture, since they are area and power-efficient. Thus, for ULP short-range biomedical implanted communications systems, the zero- or low-IF architecture combined with an FSK modulation scheme present the most suitable choice. The complexity, size and power are deferred to the outer transceiver, which has no strict size and power constraints. This combination has been the choice for short-range personal communications devices operating in the 2.4-GHz and the

433-MHz ISM bands [15-18]. However, the zero-IF architecture comes with many drawbacks such as the DC offset problem caused by the local oscillator (LO) and the high flicker noise level and hence, the low-IF architecture is preferable [14].

A simplified block diagram of an RF transceiver is shown in Fig.2.2. The system consists of a transmitter and a receiver. The main blocks of the transmitter are: an upconverting mixer, a voltage-controlled oscillator (VCO) and a power amplifier (PA). The receiver chain is built from a low-noise amplifier (LNA) and a downconverting mixer. An antenna is used for signal transmission and signal reception, which is controlled by a transmit/receive switch.

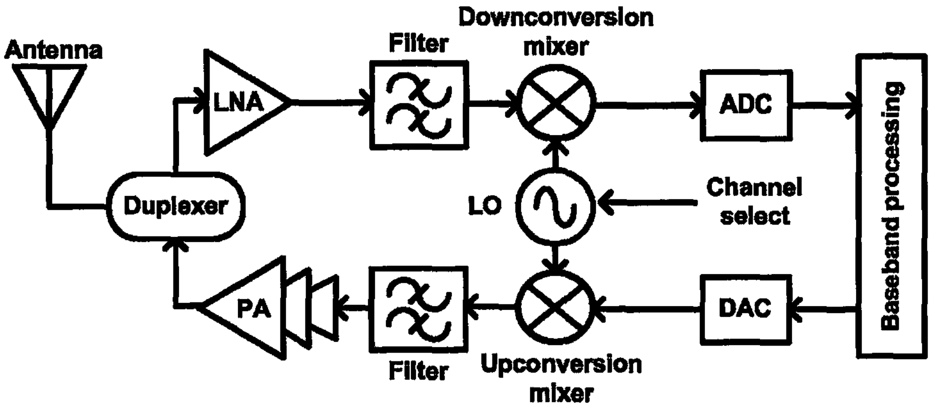

Fig. 2. 2. Simplified block diagram of an RF transceiver.

The work in this thesis is mainly concerned with the design of efficient RF blocks for the transmitter part of embedded transceiver systems. Some efforts have been made to reduce the number of transmitter blocks aiming for reduced area consumption [19], but still, the most widely used transmitter architecture for short-range device communications is the Cartesian or I/Q (In-phase/Quadrature) upconversion transmitter [14]. Figure2.3 shows the block diagram of a typical I/Q transmitter. It consists of two digital-to-analog converters (DACs), two upconversion mixers driven by quadrature phases of the LO, a PA and an antenna. As mentioned, this work deals with the design, implementation and measurements of efficient PAs and antennas for implanted biomedical transmitters.

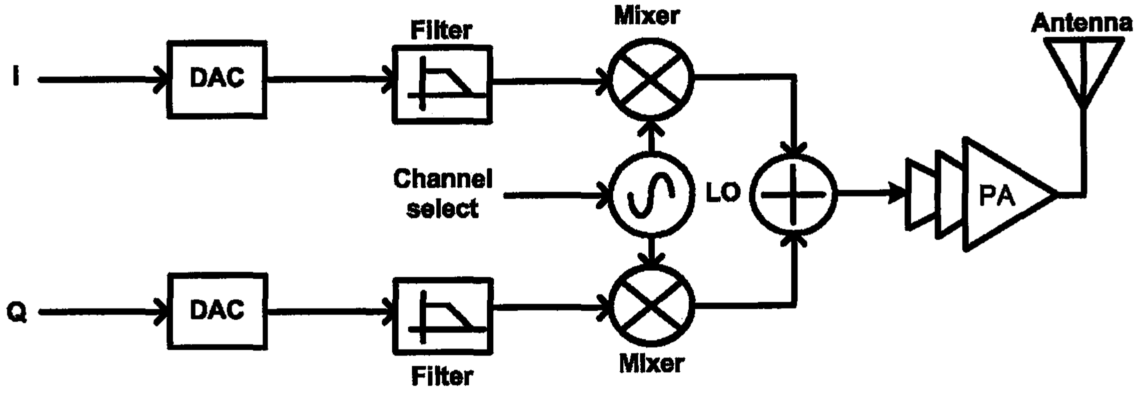

Fig. 2. 3. Cartesian (I/Q) transmitter.

2.4 IMPLEMENTATION TECHNOLOGY

A variety of technologies can be used to implement the transceiver system in implanted devices. However, for miniaturization and power saving purposes, a standard CMOS technology would be preferable. Designing the transceiver in a standard submicron CMOS technology will allow the RF circuitry to be on the same chip with the digital and image capturing circuitry; hence reducing size, power consumption and fabrication cost. Nevertheless, the CMOS process has its own limitations, which are: the insufficiently accurate models of active and passive devices at high frequencies, and the low-resisitivity substrate. The increased substrate losses at RF result in low quality on-chip passives and introduce many layout parasitic effects, while the model inaccuracy results in an increased design time of CMOS RF ICs. Despite its limitations, the great advantages of the CMOS technology over the other alternative technologies still make it the preferable technology for implementing implanted transceivers.

2.5 SUMMARY

In this chapter, the main specifications and design challenges of in-body transceiver systems have been discussed. The various possible frequency choices have been presented, emphasizing that the MICS band and the 2.4-GHz ISM band are the most suitable candidates. According to the system specifications, a simple FSK modulation technique and a simple low-IF architecture are suitable for the application. Regarding the implementation technology, the CMOS technology is the preferable technology.

CHAPTER 3

CMOS Technology for RF ICs

Among the various semiconductor technologies that are available for IC device fabrication, silicon technologies – CMOS and bipolar CMOS (BiCMOS) – are by far the most popular. These technologies have experienced a lot of attention since the very first generations of ICs, and the digital ICs are almost exclusively in silicon technologies. The main reason is the increasing number of transistors – currently in the order of 10^6 – that can be implemented on a single chip, thus allowing for very dense and highly integrated electronic circuits and systems. This increase has ever since followed Moore's law, which predicts that the number of devices per chip grows exponentially with time.

Silicon, however, was not the preferred technology for realizing RF ICs until recently. This is due to: (1) the high losses of the low-resistivity silicon substrates, which at high frequencies result in significant performance degradation of silicon devices; and (2) the lower cutoff frequencies (f_T) of silicon transistors compared to other technologies. As can be seen in Fig. 3.1, up until the late 1990's, the cutoff frequencies of devices implemented in gallium arsenide (GaAs) or silicon germanium (SiGe) technologies were significantly higher than those of CMOS and BiCMOS devices. Furthermore, between the BiCMOS and the CMOS technologies, BiCMOS was preferred for RF circuit integration, since the BiCMOS technology provides a higher resistivity substrate and bipolar transistors were known to have higher cutoff frequencies than N-channel MOS (NMOS) and P-channel MOS (PMOS) transistors [20]. Thus, before the last decade, the RF front-end was usually realized in an RF SiGe, BiCMOS, SiGe BiCMOS or in one of the group III-V semiconductor technologies, such as GaAs. Nevertheless, the vast CMOS technology scaling allowed for transistors with high frequency operation capabilities. Thus, due to its well-known advantages, CMOS has become a preferred technology of choice for implementing RF ICs. This chapter presents a review on CMOS technology for RF ICs. Section 3.1 presents the CMOS technology scaling, Section 3.2 outlines the technology limitations for RF ICs and Section 3.3 presents the most popular modeling techniques of CMOS devices at RF. Section 3.4 gives a summary of the chapter.

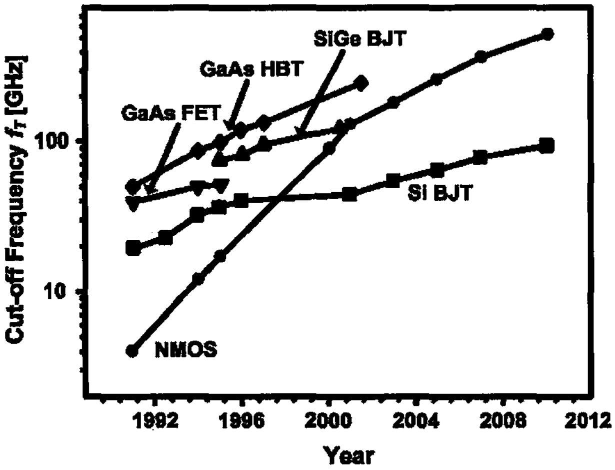

Fig. 3. 1. The evolution of the transistor's cutoff frequency (f_T) for various technologies [20].

3.1 CMOS Technology Scaling

The continual consumer market demand for high-speed, low-cost and small-size digital devices has guided the CMOS technology scaling for almost two decades up to this date. Ever since the early days of its invention in 1960 [21], the N-channel metal-oxide-semiconductor field-effect transistor (MOSFET) has had the same structure shown in Fig 3.2, but with rapidly shrinking dimensions to accommodate the digital electronics market requirements. The minimum feature size (channel length) of the technology has moved from the micrometer range to the nanometer (submicron) range. Table 3.1 lists the geometrical and process parameters of a MOS transistor, illustrating how these are varied with the scaling factor α>1.

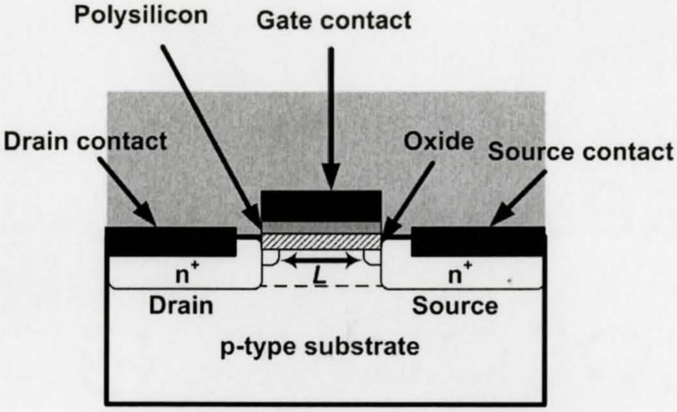

Fig. 3. 2. The structure of an N-channel MOSFET.

The operation of the transistor is characterized by the following parameters: the cutoff frequency f_T, the maximum oscillation frequency f_{max}, the transconductance g_m, the threshold voltage V_{th}, the nominal supply voltage V_{DD}, the breakdown voltage V_{BD} and the minimum noise figure NF_{min}. Table 3.2 shows how these parameters are expected to vary with the reduction of the feature dimension for an NMOSFET, as projected by the 2003 International Technology Roadmap for Semiconductors (ITRS) [22]. Devices suitable for high frequency operation – with reduced NF, power and area consumption – are now widely available.

The CMOS technology scaling comes, however, with its own limitations and drawbacks. For example, with the increase in the substrate doping concentration (N_A), the resistivity of the silicon substrate decreases, thus resulting in high losses. In addition, with the reduction of t_{ox}, the breakdown voltage of the transistor is lowered, making such devices suitable only for low-voltage, and hence low-power operation. Another reason why these devices are more suitable for low-voltage operation is the reduced nominal supply. Two additional important shortcomings of the CMOS scaling are: the sub-threshold leakage caused by the reduction of V_{th}, and the gate leakage caused by the reduction of t_{ox}.

In summary, the CMOS technology scaling not only contributed intensively to VLSI in the digital technology, but also allowed for the introduction of the revolutionary RF CMOS technology. Compared to the standard digital CMOS, the RF CMOS technology provides a thicker top metal layer, a higher resistivity substrate and allows for fabricating metal-insulator-metal (MIM) capacitors and varactor diodes.

Table 3. 1. The variation of different process parameters with constant electric field scaling.

Parameter	Scaled Parameter
Device dimensions (L, W)	L/α, W/α
Oxide thickness (t_{ox})	t_{ox}/α
Voltage (V)	V/α
Substrate doping (N_A)	αN_A
On-current (I)	αI
Electric field (E)	E
Power (P)	P/α^2

Table 3. 2. The variation of the NMOS transistor characteristics with the technology scaling as expected by the 2003 ITRS [22].

	2003	2004	2005	2006	2007	2008	2009
L_{min} [nm]	130	90	90	90	65	65	65
V_{DD} [V]	1.5	1.3	1.3	1.3	1.2	1.2	1.1
I_{ds} [μA/μm]	26	23	21	16	12	10	9
Peak f_T [GHz]	110	120	140	170	200	240	280
Peak f_{max} [GHz]	120	140	160	190	220	260	310
NF_{min} [dB]	0.8	0.7	0.6	0.6	0.5	0.4	0.4
V_{th} [V]	0.5-0.3	0.5-0.2	0.4-0.2	0.4-0.2	0.4-0.2	0.3-0.2	0.3-0.2

3.2 Limitations of Submicron CMOS for RF ICs

Although the submicron CMOS technology has become a good candidate for RF circuit implementations, it still has its own high frequency limitations. The first limitation is the increased substrate conductivity, which causes active and passive devices operating at high frequencies to suffer to a great extent from the capacitive and resistive coupling to the substrate. One way to reduce these substrate losses is to use the feature of the deep N-well provided in the modern submicron CMOS. The deep N-well acts as a guard ring that isolates the on-chip devices from the lossy substrate.

A second limitation of the CMOS technology for RF ICs is the high loss in the finite conductivity metal wires at high frequencies. The high-frequency skin and proximity effects result in a reduction in the effective area for current flow. Thus, the ohmic losses increase in form of heat dissipation, resulting in a reduced AC current. This has been overcome in newer CMOS technologies by using a higher conductivity metal for the interconnection and by increasing the thickness of the upper-most metal layer, which is most commonly used to realize circuit wiring. This limitation, together with the first one, impact strongly on the quality of the transmission line structures realized in CMOS technology – inductors, transformers, and metal interconnections.

Furthermore, short-channel MOSFETs with wide polysilicon gates have relatively high gate resistance, which results in RF performance degradation. To minimize the gate resistance, the technology providers have introduced the silicided polysilicon gates, and the RF designer can further reduce this parasitic resistance by using the multi-finger transistor structure shown in Fig 3.3.

A final important limitation of RF CMOS is the lack of highly accurate RF models. The aforementioned high frequency effects make the modeling of the active and passive devices a difficult task at RF, and there is currently immense on-going research on the accuracy and scalability issues when modeling these high-frequency effects. The insufficiently accurate models that are currently available for simulating circuits at RF result in measurement results being significantly different from the performance predicted by the simulations. This makes the design period of these circuits longer and more challenging compared to designing analog or digital circuits.

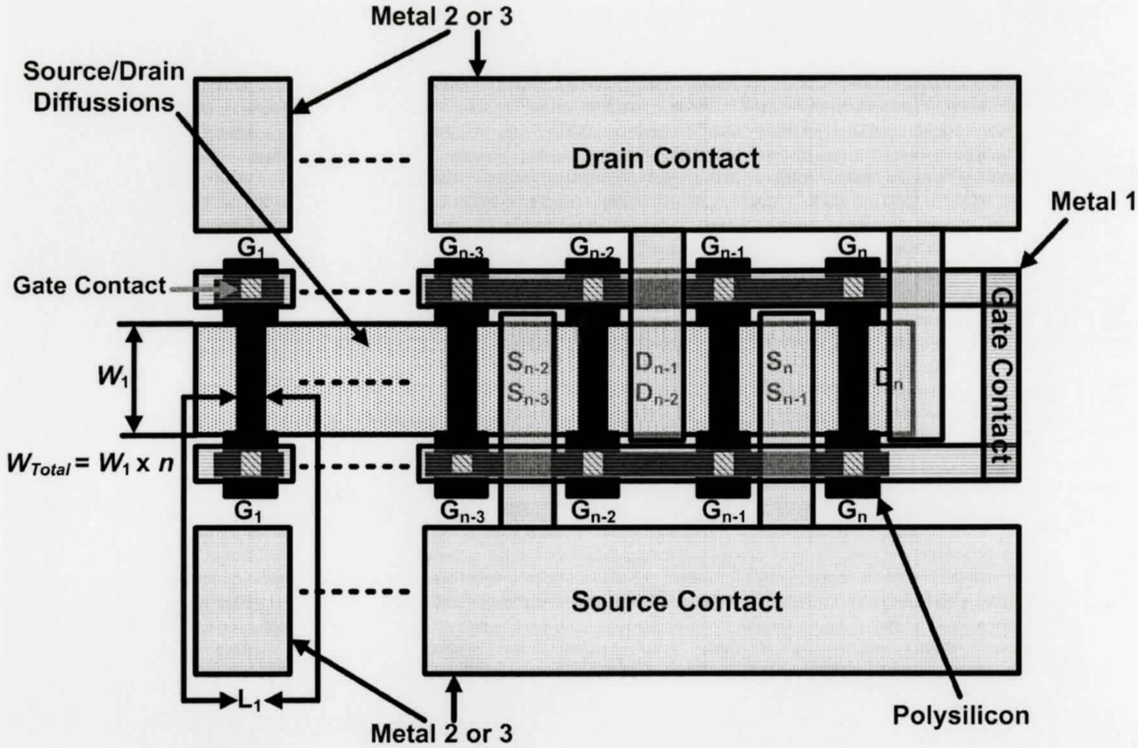

Fig. 3. 3. MOSFET layout suitable for RF operation with reduced gate resistance (some contacts including the body contact are not shown for simplicity).

3.3 RF CMOS DEVICE MODELS

As mentioned above, the availability of good reliable RF models for active and passive devices is key to accurate schematic and layout circuit simulations and hence to a reduced time-to-market for RF ICs. With the continuous CMOS technology scaling, extensive research efforts are directed to developing physics-based models that include both, the reduced-dimension effects as well as the high frequency effects. Submicron MOSFET modeling for RF operation is presented in Subsection 3.3.1. Subsections 3.3.2 and 3.3.3 present the RF models of CMOS square spiral inductors, resistors and MIM capacitors.

3.3.1 RF MOSFET Modeling

At present, the most-widely used model for submicron MOS transistors is the BSIM3v3 model developed at the University of California in Berkley [23]. The BSIM3v3 model accounts for many important physical phenomena occurring in a short-channel MOSFET. They include the short-channel and narrow-width effects, channel length modulation, gate-induced drain leakage, velocity saturation, mobility degradation due to the vertical electric field, impact ionization, non-uniform doping effects, drain-induced barrier lowering, bulk charge effect, substrate current induced body effect and the subthreshold conduction [23].

Mainly developed for the lower frequency digital circuits, the BSIM3v3 model does not account for some important high frequency effects. At high frequencies, the MOSFET behaves like a distributed device, and the major high frequency effects that need to be accounted for in models of RF MOSFETs are: the distributed losses in the gate, source and drain, the distributed channel non-quasi-static (NQS) effect and the distributed losses in the substrate. This distributed behavior of the device at high frequencies can be accurately modeled using discrete lumped element components for frequencies below 10 GHz [24].

Various ways have been presented in the literature to model the MOSFET at RF [24-27]. Most of the RF MOSFET models include an intrinsic small-signal model (e.g. BSIM3v3) as the core and additional external discrete components to model the high frequency parasitic elements. Figure 3.4 shows a simplified equivalent circuit model of a four-terminal deep-submicron RF MOSFET. The parasitic resistances, R_S and R_D represent the via-resistance, salicide resistance, salicide-to-salicide contact resistance and sheet resistance in the lightly doped drain/source (LDD) regions, while R_G models the distributed gate resistance, the gate-induced thermal noise and the NQS effects. The substrate network presents the coupling effects to the substrate and its details take several forms [24-27]. At high frequencies, the device suffers from coupling through oxide capacitance and the finite substrate resistance. The model component parameters are usually calculated using empirical formulas developed from S-parameter measurements and curve fitting procedures in terms of the geometrical and process parameters. The detailed substrate network used in our simulations can be found in the TSMC's technology document [28]. High frequency noise and distortion modeling issues are not addressed here and are not encountered in the models provided by TSMC [28].

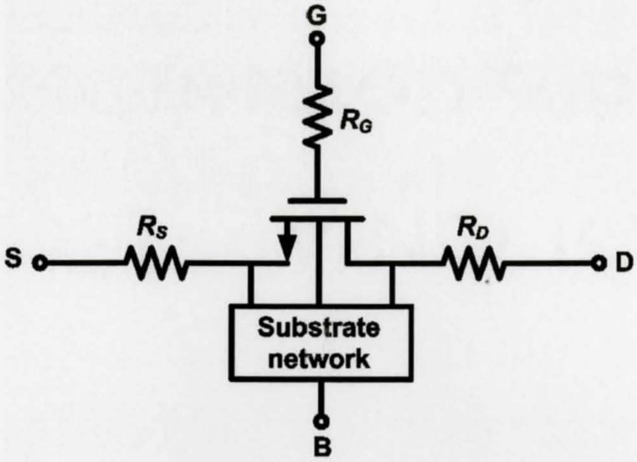

Fig. 3. 4. A four-terminal MOS transistor model for RF operation. The substrate network can take many forms [24-27].

3.3.2 Square Spiral RF Inductor Modeling

Monolithic inductors on silicon are commonly constructed by winding a planar conductor in spiral form, and it can be wound in a square, hexagonal, octagonal or circular spiral. A top view of a square spiral inductor is shown in Fig 3.5. The structure is characterized by its number of turns N, the turn's width w and the spacing between the turns s. The upper two metal layers of a technology process are used to build this structure and are connected using vias. The inductor's self-inductance is calculated using the popular Grover's formula [29].

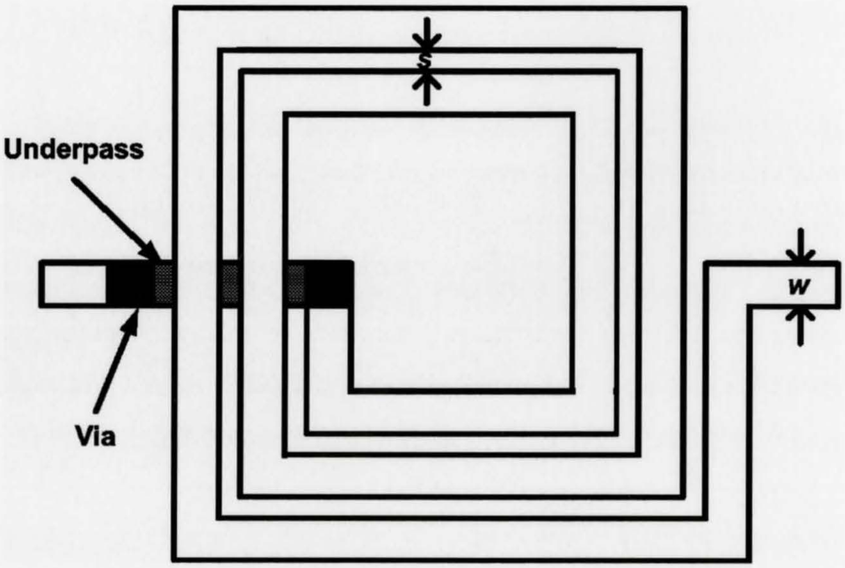

Fig. 3. 5. The layout of a square spiral inductor showing the geometrical parameters.

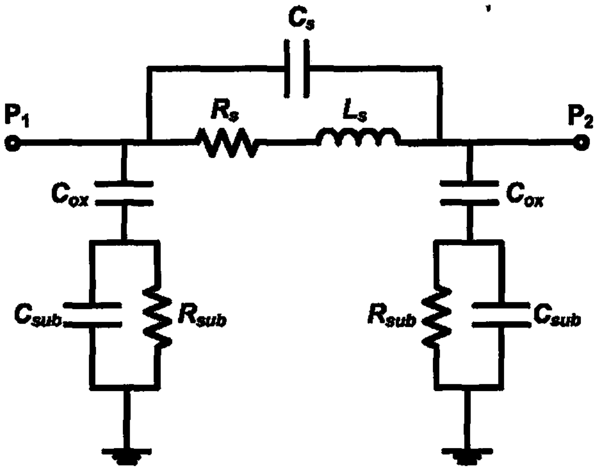

Fig. 3. 6. Compact equivalent circuit model of a square spiral inductor in CMOS [31].

Finding a compact model to model the performance of a monolithic square spiral inductor is possible because its geometrical dimensions are small with respect to the wavelength of interest. Figure 3.6 shows the most commonly used inductor model, suggested in [30] and then modified in [31]. In this model, L_s and R_s represent the series inductance and the series resistance of the conductor. C_s represents the capacitance between the inductors input and output ports, C_{ox} the capacitance between the spiral and the substrate, and C_{sub} and R_{sub} represent the losses in the silicon substrate.

Inductors are characterized in terms of their quality factor Q and self-resonance frequency f_{SR}. Since only the energy stored in the magnetic field is of interest for inductors, any energy stored in the electrical field is considered as parasitic capacitance, and any energy dissipated in ohmic form is considered as parasitic resistance. The unavoidable resistance and capacitance in a real monolithic inductor are thus counter-productive and are considered parasitics. The quality factor of an inductor Q can be expressed by [32]

$$Q = 2 \cdot \pi \cdot \frac{\text{energy stored}}{\text{energy loss in one cycle}}, \tag{3.1}$$

$$Q = 2 \cdot \pi \cdot \frac{\text{peak magnetic energy- peak electric energy}}{\text{energy loss in one cycle}}. \tag{3.2}$$

An inductor is at self-resonance when the peak magnetic and electric energies are equal. Therefore, Q is zero at f_{SR} and becomes negative for higher frequencies. To ensure that the inductance is almost independent of frequency, f_{SR} should be kept significantly above the frequency of operation.

Figure 3.7 shows the behavior of the inductor quality factor Q as a function of the operating frequency. At low frequencies, the quality factor of the inductor is dominated by the conductor losses represented in the model by R_s. At low frequencies, ωL_s is small and $(1/\omega C_s)$ and $(1/\omega C_{ox})$ are large, such that the RF signal will essentially pass through the low resistance branch containing L_s, i.e. it will pass through the spiral inductor and the quality factor will initially increase in proportion to $\omega L_s/R_s$. At frequencies beyond Q_{max} but below resonance, ωL_s is larger than $(2/\omega C_{ox}+2R_s//C_{sub})$, but still smaller than $(1/\omega C_s)$. The RF signal will flow through the substrate causing Q to decay with frequency and the substrate losses will dominate.

The increased area of inductors with a large number of turns causes the quality factor of these bulky inductors to be lower than those of inductors with smaller number of turns over the whole frequency range. The larger inductor exhibits higher losses, both at low frequencies due to the increased ohmic losses in the conductor and at high frequencies due to the larger coupling to the substrate.

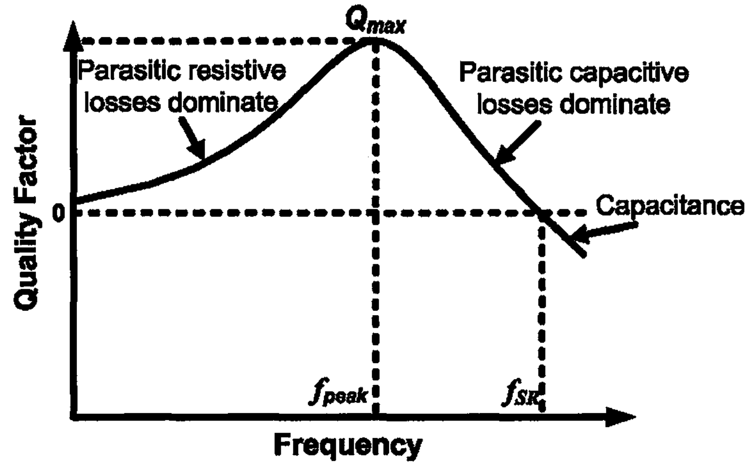

Fig. 3. 7. The behavior of the quality factor of an on-silicon inductor vs. the frequency of operation.

Inductors realized in CMOS are known to have very low quality factors due to the previously mentioned technology limitations. However, there exist many techniques to increase the quality factor of CMOS inductors, which are either conservative or innovative depending on whether or not the fabrication process is altered. In the conservative approaches, researchers tried to optimize the inductor without altering the fabrication process, e.g. using nonuniform metal width and spacing [33], exciting the inductor differentially [34], using ground planes underneath the inductor, building circular spirals, using a deep N-well, or shunting several metal layers [35]. Innovative approaches, however, offer solutions that suggest adding or altering processing steps in the original process flow for digital CMOS. Surface or bulk micromachining techniques are used to perform those innovative solutions by removing the silicon underneath the inductor, either to form suspended inductors [36], or to elevate inductors further away from the silicon substrate, and sometimes even to realize vertical inductors [37]. Thicker top metal layers and higher-conductivity metals are also utilized to reduce the conductor losses, while to reduce the losses in the substrate, it is suggested that the resistive silicon underneath the inductor be replaced by higher resistivity substrates, such as SOS (Silicon-on-Sapphire), HRS (High-Resistivity Silicon), glass, or quartz.

3.3.3 Resistors and Capacitors

Resistors in silicon technologies are realized in form of N+/P+ poly resistors with or without salicide, N+/P+ diffusion resistors with or without salicide, or in form of poly resistors with or without salicide. The resistor's value is calculated from the sheet resistance information and the resistance parasitics are usually considered insignificant.

For on-silicon capacitors, the MIM capacitors are the most widely used with a capacitance density in the range of 1 fF/μm^2 for a 0.18 μm CMOS technology [28]. As the name shows, these capacitors are constructed using two metal layers sandwiching an insulator in between. The MIM capacitor is modeled using the equivalent circuit model shown in Fig 3.8. The parameters R_s and L_s are the parasitic series resistance and the parasitic series inductance, respectively; while C_{ox}, C_{sub} and R_{sub} model the substrate losses. The values of the model parameter values are calculated using empirical formulas provided in the technology specification documents [28]. The resonant frequency f_{SR} of is given by

$$f_{SR} = \frac{1}{2\pi\sqrt{L_s C_s}}. \tag{3.3}$$

The resonant frequency (f_{SR}) of MIM capacitors realized in a 0.18 μm CMOS technology is in the range of 14-18 GHz with the smaller values for smaller area capacitances [28].

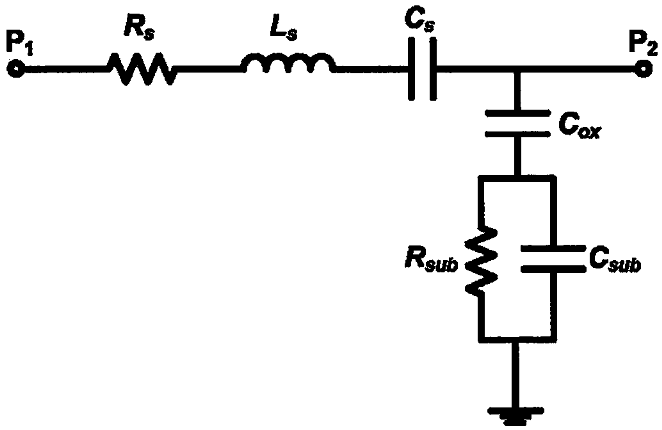

Fig. 3. 8. Equivalent circuit model of a MIM capacitor in CMOS [28].

3.4 SUMMARY

In this chapter, some background material for the CMOS technology was reviewed. CMOS technology scaling allowed for the development of RF CMOS technologies and the effects of technology scaling on the various MOS parameters were discussed. Although the RF CMOS technology is currently widely used in implementing low-power RF ICs, it comes with its own limitations, which were outlined in this chapter. Modeling issues of CMOS active and passive devices relevant to RF circuit design were also presented here above.

CHAPTER 4

Parasitics-Aware Layout Design of CMOS RF ICs

In the gigahertz frequency regime, RF circuit implementations in CMOS technology, which has a very lossy silicon substrate, suffer to a great extent from on-chip parasitics. Examples of on-chip parasitics are: parasitics due to RF pads, electro-static discharge (ESD) protection diodes, vias and most importantly, parasitics due to metal interconnections – in the form of parasitic resistances, inductances and capacitances. RF designers have to pay close attention to these parasitics in the layout design stage, in order for their circuit performance measurements to match closely those predicted by the simulations. The discrepancy between the measured and simulated circuit performance behaviors is in fact a common problem faced in the RF IC design community. With the assumption that the active and passive device models used in the simulations are accurate at RF, this discrepancy is mainly attributed to the aforementioned parasitics that arise from the actual layout of the circuit. In particular, the parasitics of on-silicon interconnections can cause an unwanted shift in the frequency of operation and a significant degradation in the circuit performance, if not properly taken into account, especially in tuned narrow-band designs.

In this work, and as presented in this chapter, we have developed a methodology to design the layout of CMOS RF ICs in a parasitics-aware manner. Parasitics of RF pads, vias and interconnection wires are considered. In the proposed layout design approach, special attention is given to the design of the metal interconnections. Each interconnection wire is designed using a simple lumped element model and the wire dimensions are varied aiming to minimize its parasitic effects on the circuit performance. The proposed methodology allows for predicting the circuit performance after fabrication and provides useful insight for the critical interconnections in the circuit. For illustration and verification purposes, the approach has been applied to the layout design of an LNA circuit operating at 5 GHz, as presented later in this chapter. The methodology has also been applied to the layout design of all PA circuits presented in this work, which are presented in Chapter 6.

In this chapter, Section 4.1 gives a brief overview of the most important high-frequency layout parasitics and suggests a simplified method to model each of them. Section 4.2 presents the proposed layout design approach and verification measurements on the LNA are presented in Section 4.3. The chapter summary is given in Section 4.4.

4.1 On-Chip Parasitic Effects

4.1.1 Probing Pads

Pads are used to interface the chip to the outside world either through bond wires or wafer probe tips and are constructed using several metal layers that are connected through vias. It must contain the top metal layer to provide external access to the chip, and it must not be covered with a passivation layer. Figure 4.1 (a) shows the pad structure in its simplest form and Fig. 4.1 (b) shows a microphotograph of a pad realized in the TSMC 0.18 µm CMOS technology. The RF pad can be modeled by a grounded capacitance to ground (C_{pad}) (Fig. 4.1 (c)) [38], which is a function of the pad area and the number of metal layers used to construct the pad. Table 4.1 shows the value of C_{pad} as a function of the number of metal layers for a 50 µm x 50 µm pad, estimated through parasitic layout extractions in the Cadence Virtuoso layout design environment. To minimize the pad capacitance at RF, they are usually realized with smaller dimensions than those used for DC connections and are constructed using fewer metal layers. However, RF IC designers sometimes prefer to use pads constructed using many metal layers to raise their life times and reliability for wafer probing, and to make them endure the frequent friction with the wafer probe tips. In the designs presented in this thesis, RF pads were constructed using the top two metal layers of the technology process – Metal 5 and Metal 6 – as a good compromise between the pad life time and its high frequencies parasitics.

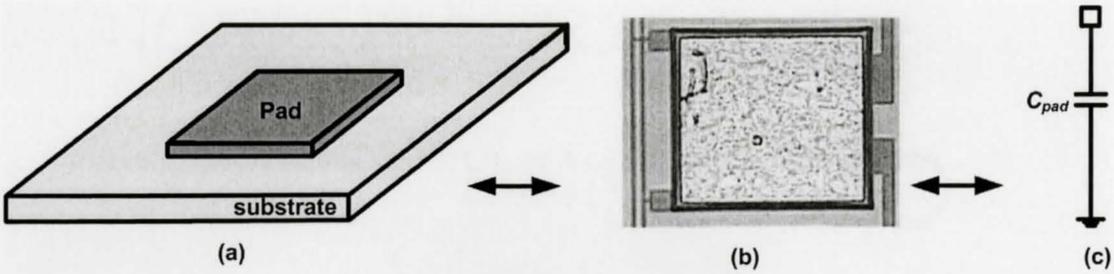

Fig. 4. 1. Bonding pad: (a) on-chip structure, (b) pad microphotograph, and (c) simplified equivalent circuit.

Table 4. 1. Extracted parasitic capacitance of RF pads.

Number of Metal Layers	C_{pad} [fF]
6 (M1-M6)	337
5 (M2-M6)	155
4 (M3-M6)	105
3 (M4-M6)	80
2 (M5-M6)	67
1 (M6)	58

4.1.2 Vias

Vias are contacts that are used to connect metal wires of different metallization layers, thus providing an underpass from an upper metal layer to the layer underneath. Figure 4.2 (a) shows a cross-section through the top four metal layers in the TSMC 0.18 μm CMOS process in which the top metal layer (Metal 6) is 0.99 μm and the remaining five metal layers are 0.53 μm thick. Vias connecting Metal 6 to Metal 5 are accordingly wider than vias between any other two metal layers. The main parasitic effect of vias is the via resistance (Fig. 4.2 (b)), which is due to confining the current flowing in narrow vias. This parasitic effect is minimized by implementing large number of vias.

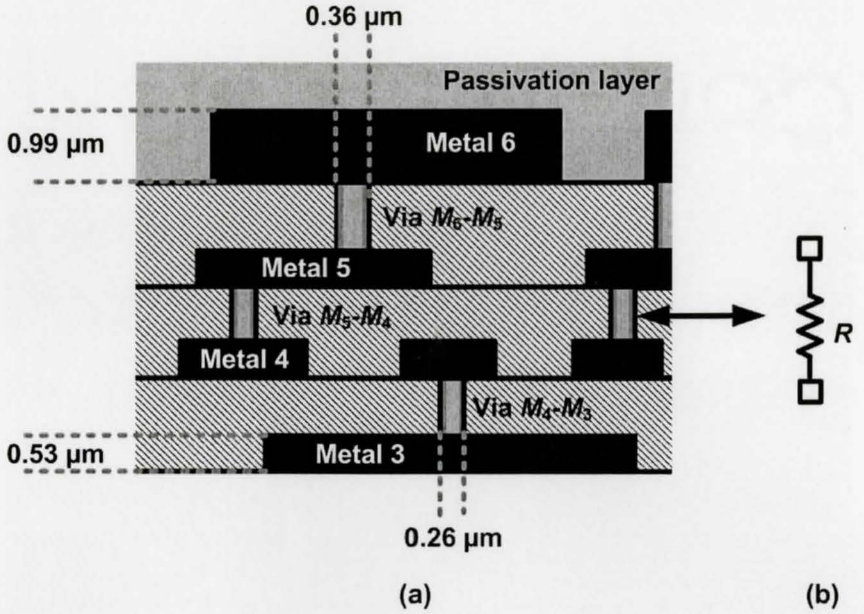

Fig. 4. 2. Vias in the layout of RF ICs: (a) a cross-section showing Metals 3, 4, 5 and 6 connected through vias, and (b) via parasitic resistance.

4.1.3 On-Chip Metal Wires

On-chip metal wires are simply mircostrip transmission lines built over the silicon substrate (Fig. 4.3) that are used to connect the various on-chip active and passive components. At very high frequencies, transmission lines have a distributed behavior and are usually modeled using distributed RLC networks as shown in Fig. 4.4 (a). However, at frequencies below 10 GHz, the frequency dependence of the transmission line model can be neglected [39] and a lumped element model such as a π-, *T*- or *L*-section model can be used. In this work, we used the simplified *L*-section model shown in Fig. 4.4 (b).

The values of L_p, R_p and C_p of the *L*-section model are calculated using one of two ways: (1) by estimating their values using full-wave EM simulations, or (2) by extracting the values of R_p and C_p using post-layout simulations of the interconnection section, and calculating L_p whose value is not provided by post-layout simulations using formulas available in the literature. Using the second approach, L_p is calculated in nanohenries using the following formula [40]

$$L_p = 2l\left\{\ln\left[\frac{2l}{w+t}\right] - 0.50049 + \frac{(w+t)}{3l}\right\}, \tag{4.1}$$

where, *l*, *w* and *t* is the length, width and thickness, respectively, of the metal interconnection in centimeters. The parameter R_p and C_p can also be calculated using the measurement data provided in the technology specification documents [28].

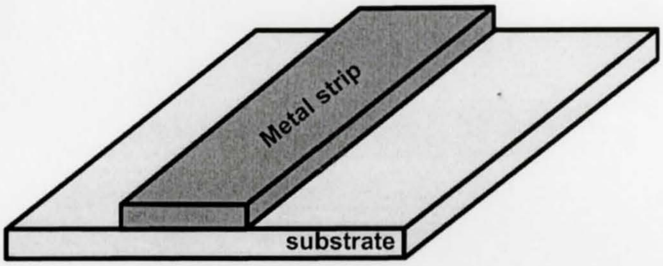

Fig. 4. 3. On-chip metal interconnections.

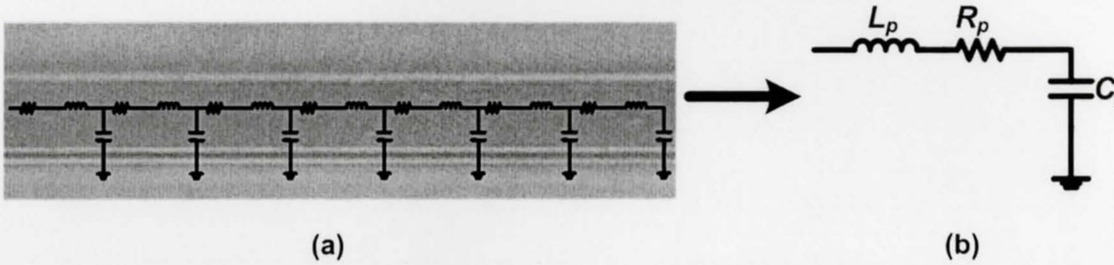

Fig. 4. 4. Modeling of on-chip interconnection wires: (a) distributed transmission line model, and (b) lumped element simplification.

4.2 Proposed Parasitics-Aware Layout Design Approach

The proposed parasitics-aware layout design approach of this work is illustrated in Fig. 4.5 through a flowchart diagram describing the RF circuit design flow. After the schematic-based simulations, the circuit is laid out in the desired technology process. The first step in the layout design stage is to properly design the layout of all passive and active devices for RF operation. The next step is to fit all the passive and active devices in the smallest possible area, which is done while trying to minimize the lengths of the interconnections and ensuring that the inductors are not coupled to each other or to other circuit components. Metal interconnections are then used to connect all the circuit components. Among the previously mentioned parasitics that arise from the circuit layout, the interconnection parasitics have the largest impact on the circuit performance. In the following text, we present a methodology to optimize these interconnections with a brief comparison with the traditional approach.

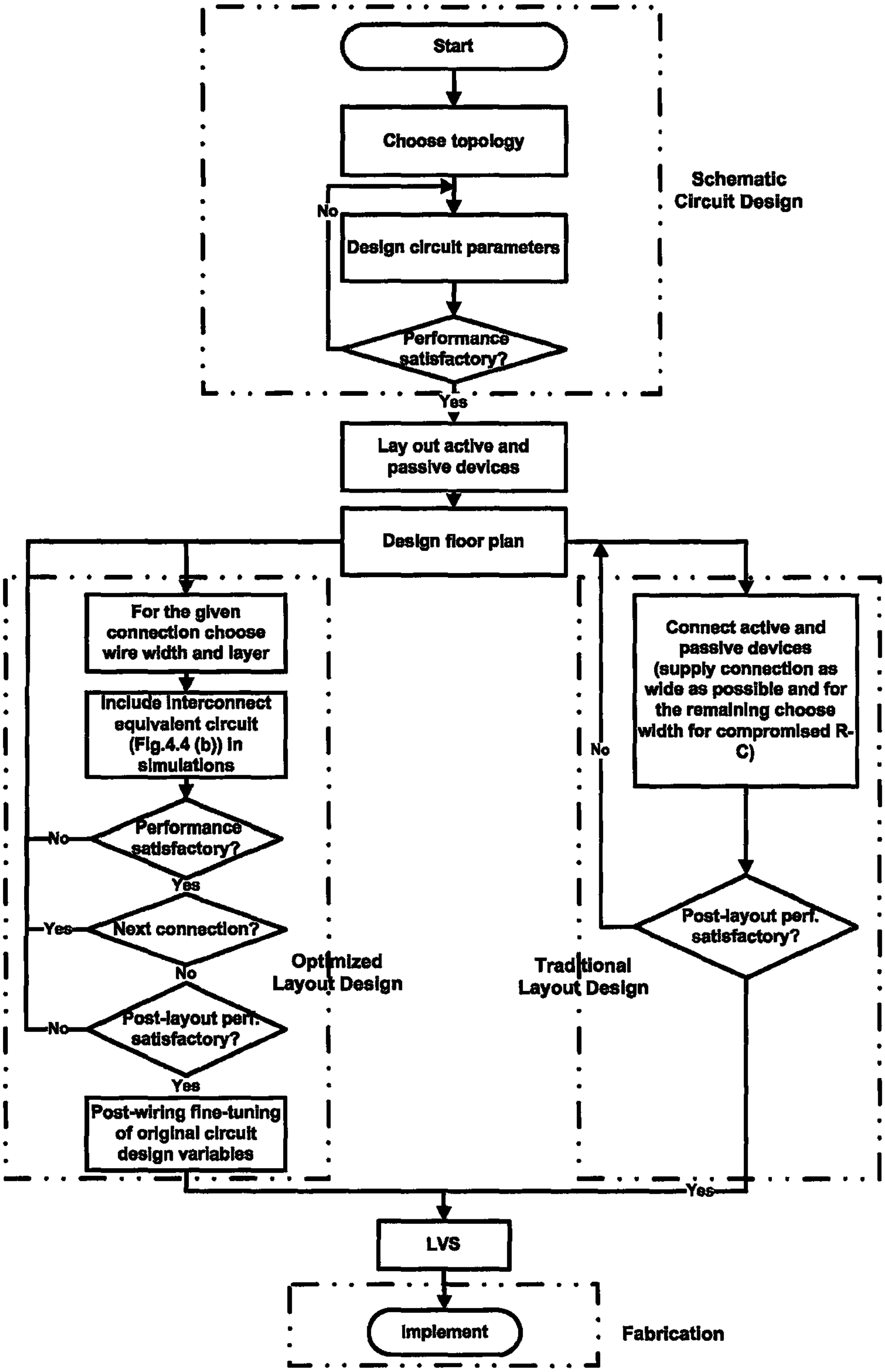

Fig. 4. 5. RF IC design flow comparing the traditional layout design approach with the one implemented in this work [89].

For interconnection wires, there exists a trade-off between the parasitic resistances and capacitances. To minimize the parasitic resistance, the metal wire should be as wide as possible, while for minimum parasitic capacitance, it should be as narrow as possible. The upper metal layer of the technology process features minimum resistive and capacitive effects since it is thicker in most technologies than the other metal layers and is further away from the substrate. It is therefore a common practice to use this upper metal layer for all the interconnections.

Traditionally, circuit designers rely on their experience in designing the metal widths. After connecting the circuit, they perform a post-layout simulation to investigate how the circuit performance is affected. There are many drawbacks of this approach: (1) the post-layout simulations do not account for the inductive effect, which might significantly affect the circuit tuning, especially in narrow band designs. (2) It does not provide insight into the critical nodes of the circuit, to which the circuit performance is most sensitive; and (3) finally, it is based on trial and error and hence, is a time consuming process.

The approach presented in this work, however, is based on modeling the interconnection wires in the simulations and investigating the impact of their parasitics on the circuit's performance. By inserting the simplified lumped element model of the interconnection, shown in Fig. 4.4 (b), into the circuit schematic, it is possible to investigate the sensitivity of the circuit performance to a particular interconnection section and accordingly optimize it by varying the metal width and, if applicable, the number of stacked metal layers. Given the length of the interconnection, the goal of the optimization is to achieve optimum circuit performance, or equivalently, to achieve minimal degradation in the circuit performance that is caused by the parasitics of a particular interconnection wire. There is no rule of thumb for the first guess of the metal width; but it is always useful to start with extremes (minimum and maximum allowable widths) to determine the parasitic effect that is more likely to kill the circuit's performance and thus define the initial guess accordingly. The optimization process then follows a random search for the best metal width, where the parameter range is constrained by the layout design rules. After designing the layout, a final post-wiring fine-tuning step is performed on the design parameters of the various circuit components, such as the sizes of transistors and the number of turns of the inductors. This fine-tuning step is intended to compensate for the degradation in the performance characteristics of the circuit due to the layout parasitics.

4.3 VERIFICATION OF THE USEFULNESS OF THE PROPOSED APPROACH: 5-GHZ LOW-NOISE AMPLIFIER LAYOUT DESIGN

Figure 4.6 shows the circuit schematic of the 5-GHz LNA that was used for verification. It has been realized using the TSMC 0.18 µm CMOS process. It is a simple single-stage topology utilizing the common inductive source degeneration technique (L_s) to provide input matching to 50 Ω. A cascode transistor has been added to isolate the input and the output signals, hence facilitating the design of their matching networks (L_g, C_g and L_o, C_o). The inductor L_i and the capacitor C_i are used to provide the necessary interstage matching between the input transistor and the cascode transistor. Biasing is provided to the gate of M_1 through an on-chip biasing circuit, which is not shown in the figure for simplicity.

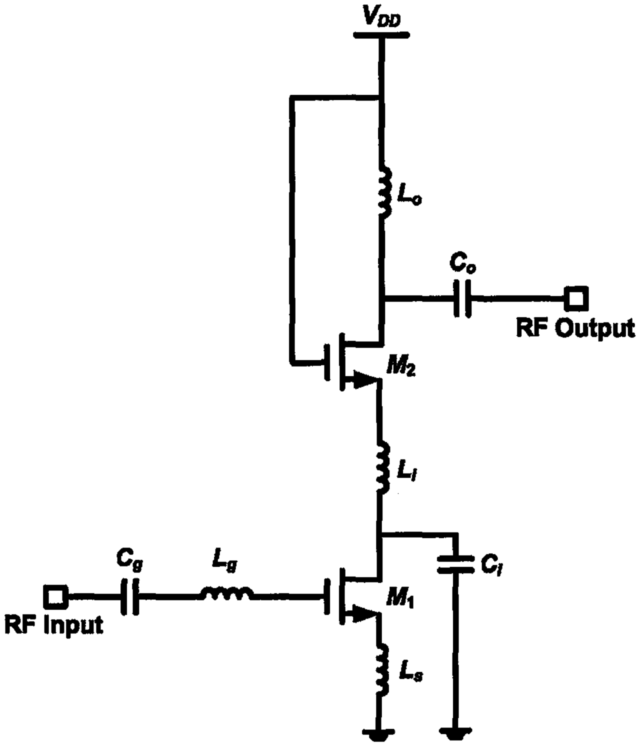

Fig. 4. 6. Circuit schematic of the designed 5-GHz LNA.

The proposed layout design methodology was applied to the layout of the above LNA circuit. The various components have been laid out in an RF compatible manner. Transistors were designed using a multifinger configuration, inductors in form of square spirals and capacitors using the MIM structure. The values of the various parameters of the circuit components are listed in Table 4.2. The layout parasitics have been accounted for in the simulations. Parasitics due to the RF pads, vias and those due to interconnection metals have been modeled in the simulated circuit schematic. Each metal interconnection was designed and optimized individually in the simulations using the model shown in Fig. 4.4 (b). Figure 4.7 shows the LNA circuit schematic including the interconnection metals. The pad capacitances and the via resistances are not shown for simplicity. The top metal layer (Metal 6) was used to construct all interconnections. A chip micrograph of the implemented circuit is shown in Fig. 4.8, which clearly shows the variability in the wire widths resulting from the interconnection design approach discussed above. The total area is about 1000 μm x 960 μm.

Table 4. 2. Components values of the designed 5-GHz LNA.

Component Parameter	**Value**
C_g	35 pF
L_g	3.9 nH
M_1	22 x 2.5 μm x 0.18 μm
L_i	3.9 nH
C_i	30 fF
M_2	70 x 2.5 μm x 0.18μm
C_o	200 fF
L_o	2.3 nH

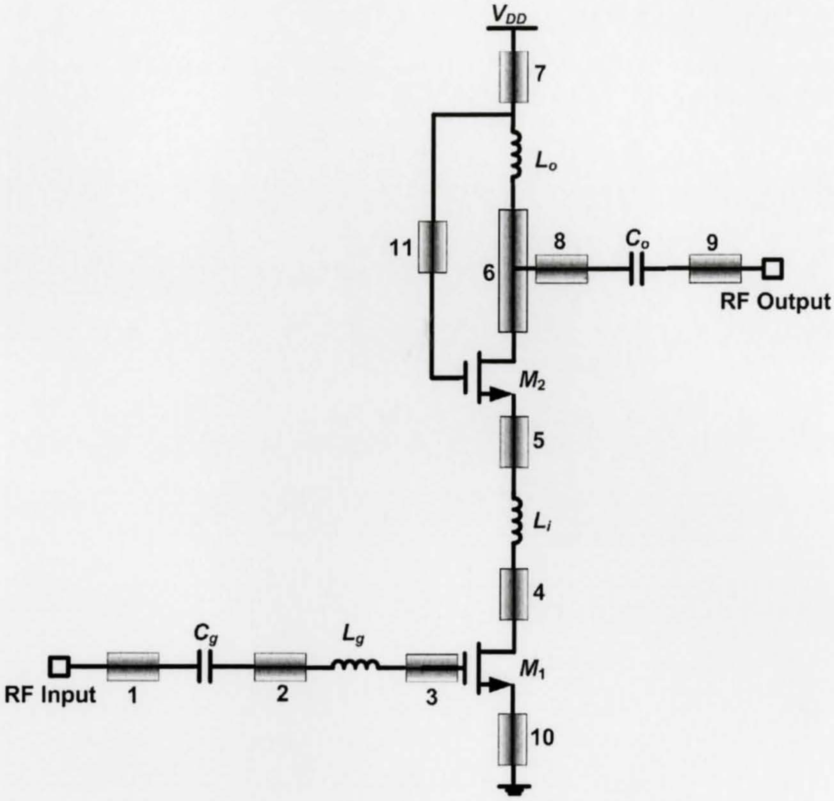

Fig. 4. 7. Circuit schematic of the 5-GHz LNA including the interconnect wires.

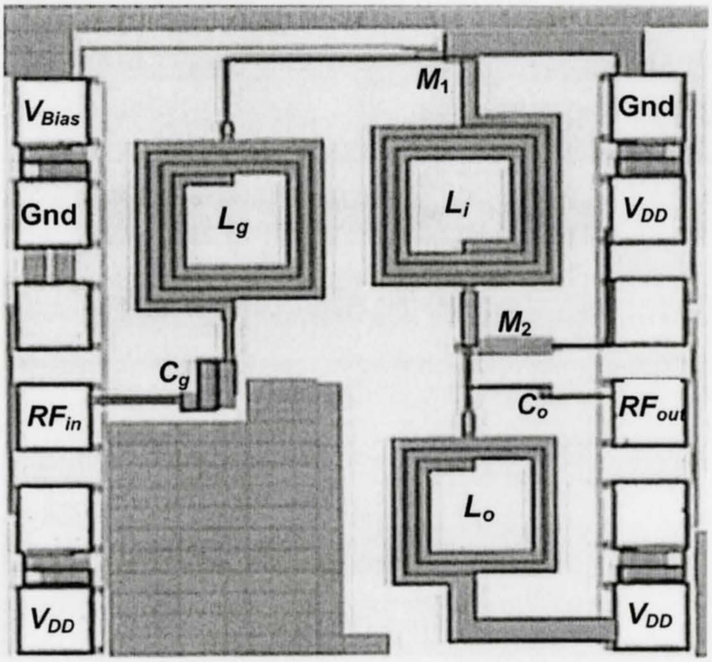

Fig. 4. 8. Chip micrograph of the 5-GHz LNA showing the variability of the interconnection widths.

As shown in Fig. 4.7 and from the chip micrograph, the source degeneration inductor L_s and the interstage matching capacitor C_i have been omitted in the actual layout. For a 22-finger NMOS device with 2.5 μm channel width, biased close to threshold, a source degeneration inductor of 0.2 nH value is needed to realize 50 Ω impedance at the input. This is a very small value for an actual on-chip spiral inductor. The layout parasitics have been utilized instead and we have relied on the parasitic inductances and resistances at the input of M_1 to provide the required matching. Additionally, the capacitor C_i with a value of 30 fF can be realized using a wide metal wire rather than an actual MIM capacitor. As can be seen in the microchip photograph, the interconnection between the source of M_1 and ground (interconnection number 10 in Fig. 4.7), was designed to be long to introduce the needed inductance for source degeneration. The parasitic series resistance of inductor L_g and the parasitic series resistance of the gate of transistor M_1 further contribute to the real part of the input impedance. Connections 4 and 5 were designed to be wide to provide the necessary interstage matching (C_i).

It was observed that the connections at the input, connections 1 and 2, are sensitive to high parasitic resistance. Connections at the gate of M_1 and the output nodes are all sensitive to both resistances and capacitances and were hence optimized to give optimum parasitic effect. The supply and ground connections were found to be extremely sensitive to high parasitic resistance and were hence designed using the widest possible dimension (35 μm). Table 4.3 shows the dimensions of the various interconnections that have resulted from the optimization process described here. The table shows also the calculated parasitic components associated with each metal wire.

On-wafer *S*-parameter measurements were performed using an Agilent-8722ES *S*-parameter network analyzer, an HP-4145B semiconductor parameter analyzer, and a probe station. Figures 4.9 to 4.11 show the measured performance characteristics together with the simulation results of the designed LNA circuit at 1.8 V supply and 1.2 V biasing circuit supply voltages. The performance of the circuit was evaluated in terms of its gain and input and output return losses. As can be seen from the figures, a good match was obtained between measurement and simulation results due to carefully considering the layout effects in the simulations, as described above.

The ideal simulations (simulations with no parasitic components) were not included in the comparison figures, since some circuit components have been removed and the values of some circuit parameters have been fine-tuned to account for the parasitics. However, by comparing the measured gain with the value predicted by the ideal simulations led to the following observation: the measured gain peak experienced a frequency down-shift of 0.2 GHz and a decrease of ~ 4 dB in magnitude. Following the layout approach described above, both effects – magnitude change and frequency shift – were predicted and minimized, and a good match between the measurements and the simulations was finally achieved. The noise figure (*NF*) of the circuit was not considered in the illustration presented here, since the RF transistor models provided by the foundry do not provide accurate modeling of the high frequency noise performance [28]. Any discrepancy between the simulation and the measurement results is expected to be due to this modeling inaccuracy.

Table 4. 3. Interconnection wires dimensions and model parameters.

Interconnection No.	w [μm]	l [μm]	R_p [Ω]	L_p [nH]	C_p [fF]
1	10	120	0.432	0.063	17.6
2	10	70	0.252	0.03	10.3
3	4	400	3.6	0.37	23.5
4	20	80	0.15	0.024	24
5	20	80	0.15	0.024	24
6	6	120	0.72	0.0733	10.6
7	35	270	0.28	0.12	139
8	3	80	0.96	0.05	3.5
9	3	80	0.96	0.05	3.5
10	35	300	0.3	0.122	140
11	4	210	1.9	0.165	12.5

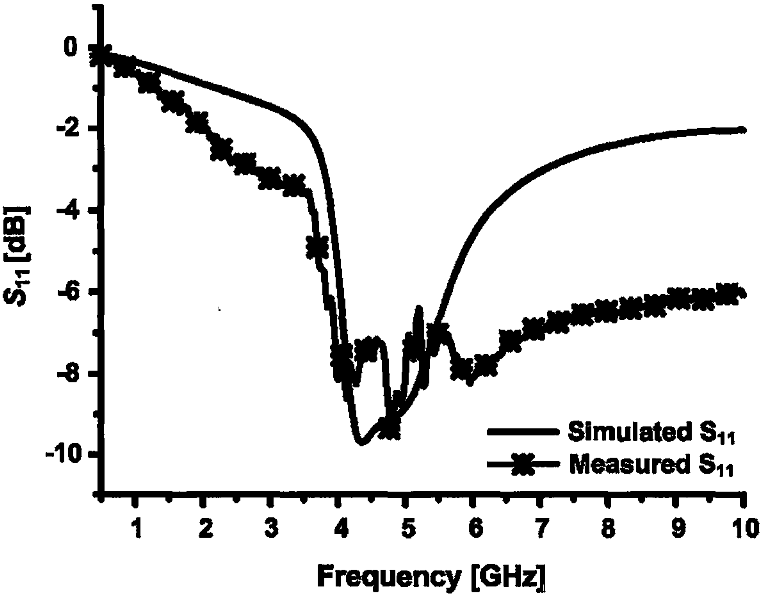

Fig. 4. 9. Comparison between the measured and the simulated input return loss (S_{11}).

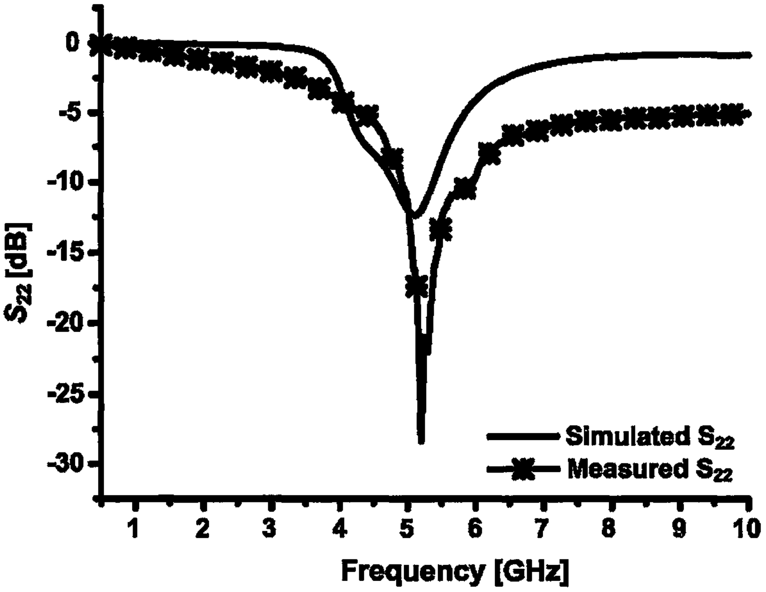

Fig. 4. 10. Comparison between the measured and the simulated output return loss (S_{22}).

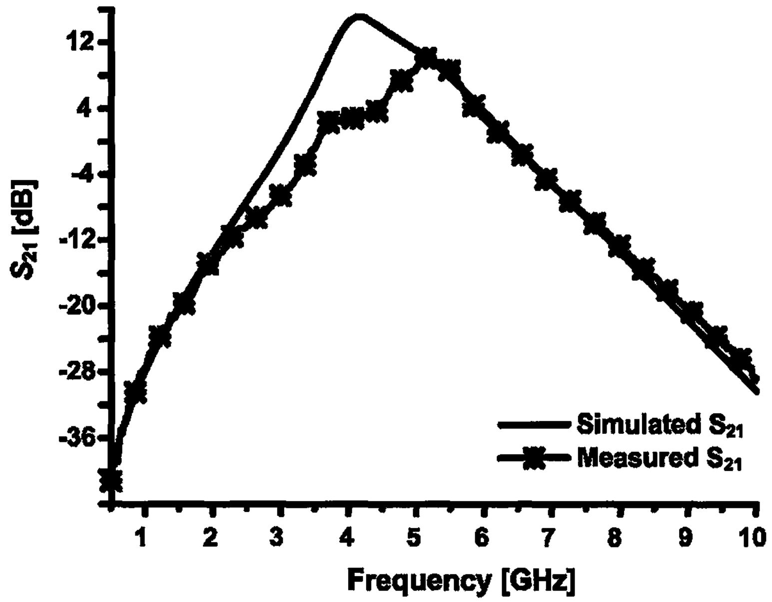

Fig. 4. 11. Comparison between the measured and the simulated gain (S_{21}).

4.4 SUMMARY

Layout parasitics, particularly those due to metal interconnections, can significantly degrade the performance of CMOS RF ICs, especially at gigahertz frequencies. In this chapter, we presented a parasitics-aware methodology for designing the circuit layout that allows for minimizing degradation in circuit performance. The proposed approach was verified using a 5-GHz CMOS LNA circuit, which exhibited good performance characteristics and good agreement between measurement and simulation results. At 5 GHz, a supply voltage of 1.8 V and a gate biasing voltage of 1.2 V, the LNA consumes 3.8 mA from the supply and provides a gain of ~ 10 dB, with its input and output matching to 50 Ω impedances ($S_{11} \leq$ -9 dB and $S_{22} \leq$ -10 dB).

CHAPTER 5

Overview of RF Power Amplifiers

Radio frequency power amplifiers (RF PAs) appear as the last block before the antenna in the transmitter chain of RF transceiver systems (Fig. 2.2). Their main function is to boost the power of the RF signal to the required level in an efficient manner prior to transmission through the antenna. RF PAs are mainly classified based on their operation as current-mode (linear) or switching-mode (nonlinear) topologies. This chapter provides some PA background information. Section 5.1 lists the main metrics that are used to characterize the PA performance and Section 5.2 gives an overview of the different classes of PA operation. The chapter's summary is given in Section 5.3.

5.1 POWER AMPLIFIER PERFORMANCE CHARACTERISTICS

Figure 5.1 shows a block diagram of a PA circuit of any class of operation. The PA delivers an output power $P_{out,rf}$ to the antenna while consuming P_{DC} Watts from the supply with an input drive of $P_{in,rf}$. The following subsections list the most important performance metrics that are used to characterize the performance of RF PAs.

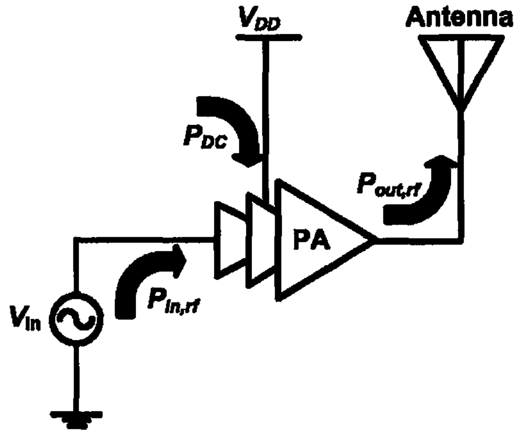

Fig. 5. 1. Block diagram of a PA showing the various power terms.

5.1.1 Output Power

PAs are classified according to the level of output power ($P_{out,rf}$) into low-power or high power amplifiers. The PA circuit is usually designed to deliver a specific amount of output power to the antenna. Assuming a purely resistive output load, the output power is defined as the product of the root mean square (rms) of the output current and the rms of the output voltage and can be expressed by

$$P_{out,rf} = rms(I_o) \times rms(V_o). \tag{5.1}$$

5.1.2 Power Consumption

The PA consumes an amount of DC power (P_{DC}) from the DC supply. P_{DC} is the dynamic power consumption of the amplifier, which is the product of the average current and voltage at the drain and is given by

$$P_{DC} = avg(I_{DD}) \times avg(V_{DD}). \tag{5.2}$$

5.1.3 Power Gain

The gain of the amplifier is defined as the ratio of the RF output power ($P_{out,rf}$) to the RF input power ($P_{in,rf}$)

$$G = \frac{P_{out,rf}}{P_{in,rf}}. \tag{5.3}$$

5.1.4 Drain Efficiency and Power-Added Efficiency (PAE)

The PA performance is typically measured in terms of its efficiency. The efficiency of a PA circuit can be expressed in one of two ways. The first is the drain efficiency η_D, which is defined as the ratio of the RF power delivered to the load $P_{out,rf}$ to the dynamic DC power consumed by the circuit P_{DC}. The second, and the most commonly used term is the power-added-efficiency (PAE). The PAE describes how much power is added to the input power $P_{in,rf}$ using the supply efficiently and taking the gain of the PA into account. The drain efficiency and the PAE are expressed by

$$\eta_D = \frac{P_{out,rf}}{P_{DC}}, \tag{5.4}$$

$$PAE = \frac{P_{out,rf} - P_{in,rf}}{P_{DC}} = \eta_D \left(1 - \frac{1}{G}\right). \tag{5.5}$$

5.1.5 Linearity

Usually, the 1-dB compression, the third-order intercept point (IP_3) and the level of the harmonic signals are used to describe the linearity behavior of nonlinear amplifier circuits. Nonlinearities in amplifiers are caused by the nonlinearities of the active device. It is said that an amplifier is operating at gain compression if the output signal of the amplifier is no longer a linear function of its input. The 1-dB compression point is the level of the input power at which the output power is one dB lower than predicted by the small-signal linear relationship. The third-order intercept point (IP_3) describes the intermodulation distortion, which is caused by the presence of two signals at the input. It takes the form of spurious third-order signals present at the output at ($2f_2$ - f_1) and ($2f_1$ - f_2). Figure 5.2 shows the concept of the 1-dB compression point and the IP_3 on a traditional input-output response of an amplifier circuit. In the case of input signals with varying amplitudes, the PA nonlinearities cause spectral re-growth resulting in signal power loss in the neighboring channels. Thus, another way to measure the amplifier nonlinearity is in terms of the adjacent channel power ratio (ACPR), which is defined as the level of the signal power in the adjacent channel to the signal power in the channel of interest. In the application under consideration, a constant-envelope modulation scheme is suitable, so no neighboring channels exist and the PA has relaxed linearity requirements. The linearity of the PAs presented in this work has been tested in terms of the 1-dB compression point and the level of the harmonic signals.

There exist many techniques for improving the linearity of PAs [41, 42]. However, this is only possible at the expense of increased complexity and hence power consumption. The topic of PA linearization is beyond the scope of this thesis. The feed forward, the feedback and the pre-distortion techniques are used in base-station PAs; and the envelope elimination and restoration (EER), Doherty amplifiers and the linearization using nonlinear components (LINC) are used to enhance the linearity and the efficiency of low-power PAs.

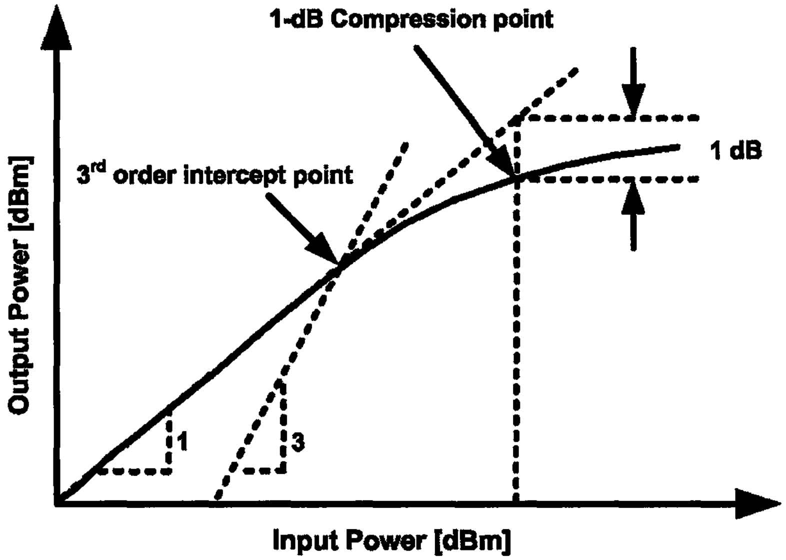

Fig. 5. 2. Input-output response of an amplifier showing the 1-dB compression point and the third-order intercept point.

5.1.6 Figure of Merit (FoM)

A figure of merit (FoM) is usually used to evaluate the performance of RF ICs and to compare various designs. The PAE is the most commonly accepted FoM for the comparison between PAs. However, it does not account for many important metrics that are used to categorize PAs, such as the output power level, the linearity behavior and the frequency of operation. A FoM for comparing performance of PAs has been suggested in the 2003 ITRS [22]. This FoM is given in logarithmic form by

$$FoM_{ITRS} = 10\log\frac{P_{out,rf}}{1mW} + 10\log G + 20\log\frac{f}{1Hz} + 20\log PAE. \tag{5.6}$$

This FoM takes the frequency of operation and the output power level into account, but it does not consider the linearity. Also, it accounts for the output power and the gain twice (as explicit expressions and implicitly in the PAE). In [19], the FoM proposed in the ITRS was modified to eliminate this redundancy and is given as

$$FoM = 10\log\frac{P_{out,rf}}{1mW} + 10\log G + 20\log\frac{f}{1Hz} - 10\log\frac{P_{DC}}{1mW}. \tag{5.7}$$

5.2 Power Amplifier Classes

The PAs appear in many different topologies classified according to the operation mode of the active device into linear-class, also known as current-mode topologies, and nonlinear-class, also known as switching-mode topologies.

5.2.1 Current-Mode PAs

The current-mode A, B, AB or C, also known as linear-class PAs, are presented in this section. In these PAs, the output transistor is operated as a voltage-controlled current source and the output waveform follows the input waveform. All linear classes have the same circuit topology shown in Fig 5.3, which will be explained in greater detail in Chapter 6. The linear classes are distinguished by the fraction of the RF cycle (conduction angle α) for which the output transistor conducts, which depends on the transistor's input bias. In a class A PA, the transistor conducts for the whole RF cycle (α = 360°) and for class B operation, it conducts for half the cycle (α = 180°). For class AB operation, 180° $\leq \alpha \leq$ 360°, and for class C operation, 0° $\leq \alpha \leq$ 180°.

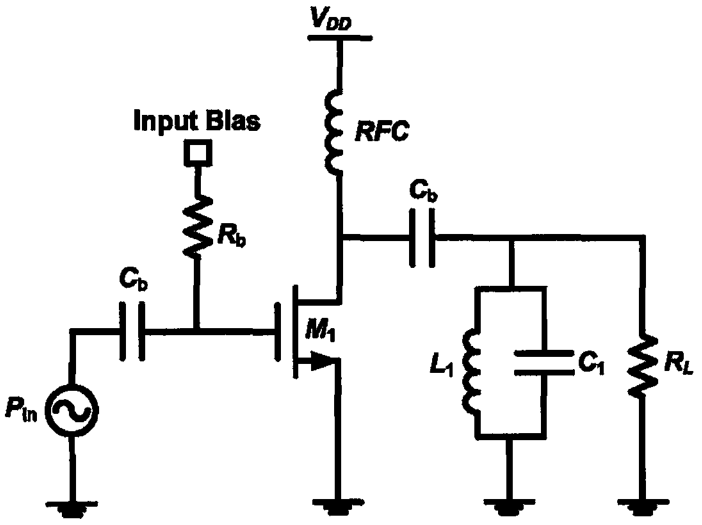

Fig. 5. 3. Circuit schematic of a single-stage linear-class PA.

In the linear-class topologies, assuming a sinusoidal input signal, the drain current will have the waveform of a truncated sine wave shown in Fig 5.4. It can be expressed as [43]

$$i(\theta) = \begin{pmatrix} I_m \cos\theta + I_{dq} & -\alpha/2 \le \theta \le \alpha/2 \\ 0 & \text{elsewhere} \end{pmatrix}. \tag{5.8}$$

Here, I_m is the amplitude of the sine wave and I_{dq} is the DC offset of the wave. I_{dq} is positive for classes A and AB operation, negative for class C and zero for class B operation. Taking the Fourier series of the above periodic waveform, the drain current can be expressed as

$$i(\theta) = i_{dc} + \sum_n i_n \cos n\theta, \tag{5.9}$$

where i_n is the nth component of the drain current given by

$$i_n = \frac{1}{\pi} \int_{-\alpha/2}^{\alpha/2} \frac{I_m}{1-\cos\alpha/2} (\cos\theta - \cos\alpha/2) \cos n\theta d\theta. \tag{5.10}$$

After evaluating the integral, i_n can be expressed by [43]

$$i_n = \frac{I_m}{2\pi}\left(\frac{2}{n+1}\sin(n+1)\alpha/2 + \frac{2}{n-1}\sin(n-1)\alpha/2\right) + \frac{2I_{dq}}{n\pi}\sin\frac{n\alpha}{2}. \tag{5.11}$$

The DC component of the drain current i_{dc} is evaluated from [43]

$$i_{dc} = \frac{2I_m \sin\alpha/2 + \alpha I_{dq}}{2\pi}. \tag{5.12}$$

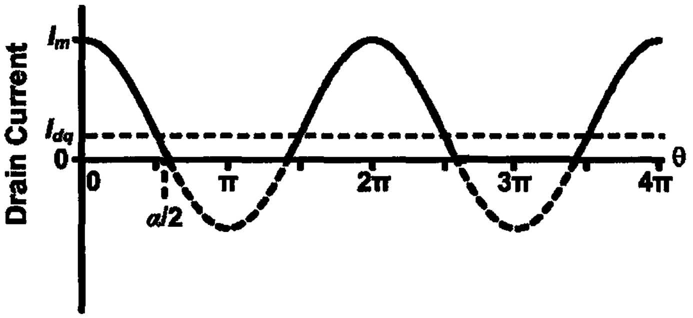

Fig. 5. 4. Sinusoidal drain current in linear-class PAs.

Using a properly designed output filter, all the harmonic components can be filtered to realize the desired sinusoidal output. The drain efficiency and the output power, which are defined in (5.4) and (5.1), respectively, can be now expressed as [43]

$$\eta_D = \left(\frac{V_{DD} - V_k}{V_{DD}}\right) \frac{\alpha - \sin\alpha}{4\left(\sin\alpha/2 - \alpha/2\cos\alpha/2\right)}, \tag{5.13}$$

$$P_{out,rf} = \frac{1}{2} v_o i_1 = \frac{1}{2}\left(V_{DD} - V_k\right)\frac{I_m}{2\pi}\left(\alpha - \sin\alpha\right). \tag{5.14}$$

In the above equations, V_{DD} is the supply voltage and V_k is the transistors drain saturation voltage (knee voltage). Figure 5.5 presents a plot of the efficiency and the output power versus the conduction angle α. Figure 5.6 plots the DC component and first five harmonic signals as a function of the conduction angle α. As is evident in these figures, as the conduction angle decreases (toward class C operation), the DC component becomes smaller and hence the efficiency increases. However, it is also intuitive in these figures that this occurs at the expense of a lower output power and an increased harmonic content of the signal, resulting in a degraded linearity. Hence, in the design of linear-class PAs, there is a direct trade-off between efficiency, output power level and linearity. It should be noted that although class AB PAs have a high third-order harmonic content, they present the best compromise between linearity, efficiency and output power level.

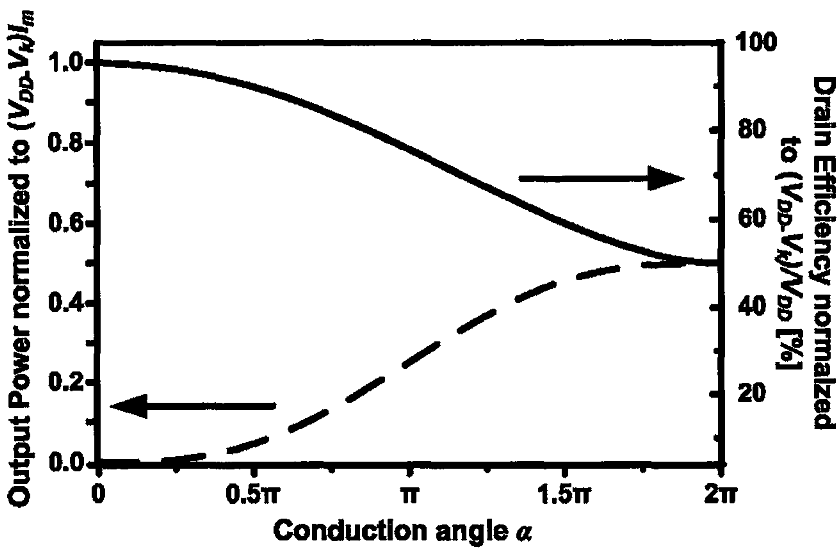

Fig. 5. 5. Efficiency and output power of linear-class PAs vs. the conduction angle α.

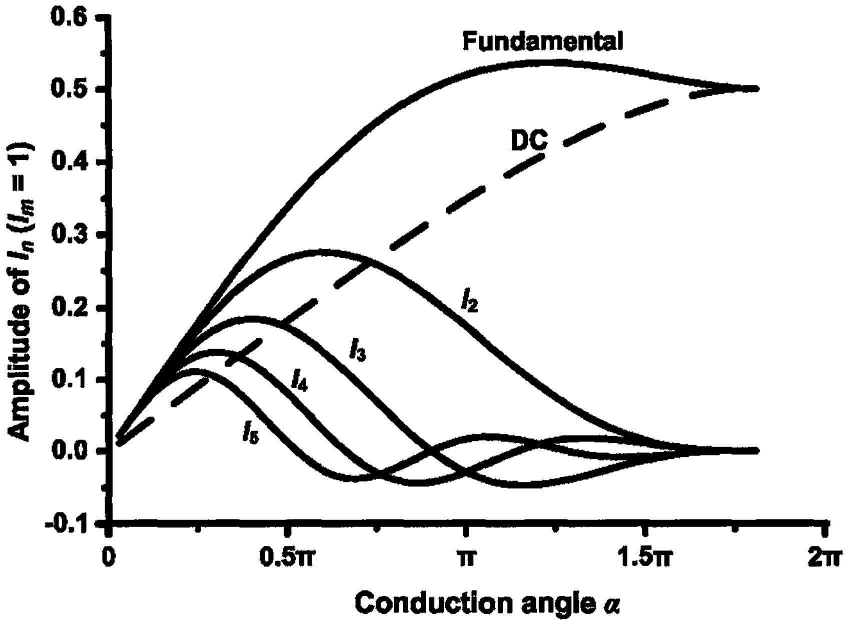

Fig. 5. 6. Level of the DC and the first five harmonic signals of the drain current in linear-class PAs as a function of the conduction angle α.

5.2.2 Switching PAs

In the switching mode PAs, classes D, E and F, the output transistor operates as a switch. As previously mentioned, the power consumption of the PA is the product of the drain voltage and the drain current. Maximizing the efficiency can be achieved by minimizing the time during which the current and the voltage are simultaneously nonzero. This can be done by having a drain voltage with a square waveform (Fig. 5.7). Since in these classes of operation, the active device operates as a switch rather than an amplifier, there is no relationship between the amplitude of the input signal and the output signal; the output signal only follows the input signal in its timing information (phase and frequency). These classes of operation provide higher efficiencies at the expense of linearity. The output waveform is highly distorted, hence filtering is essential to reconstruct a sinusoidal waveform for transmission. Theoretically, efficiencies up to 100% are achievable using this type of amplifiers. The efficiency is mainly affected by the switching time, the on-resistance of the active device and the quality of the passive and active elements used. However, since MOSFETs are not ideal switches, efficiencies less than 100% are to be expected. One final note about switching mode PAs is that they require a large input drive, hence providing a lower gain than the linear-class topologies.

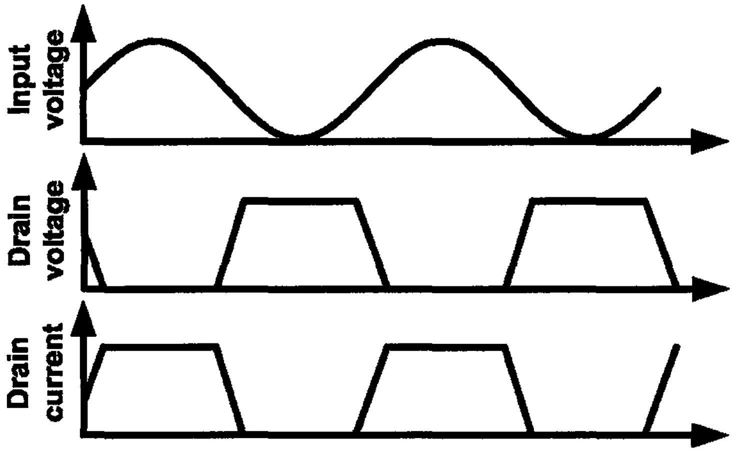

Fig. 5. 7. Drain voltage and drain current waveforms in switching-mode PAs showing that the duration during which both are nonzero is minimum allowing for maximum efficiency.

Figure 5.8 shows the circuit schematic of a typical class D PA. It is simply a CMOS inverter with a digital square wave at the output. Only one device is on at a time with each of them handling either the positive or the negative half cycle. This results in the output node being alternatively pulled down to zero and pulled up to V_{DD} realizing the required square waveform at the output node.

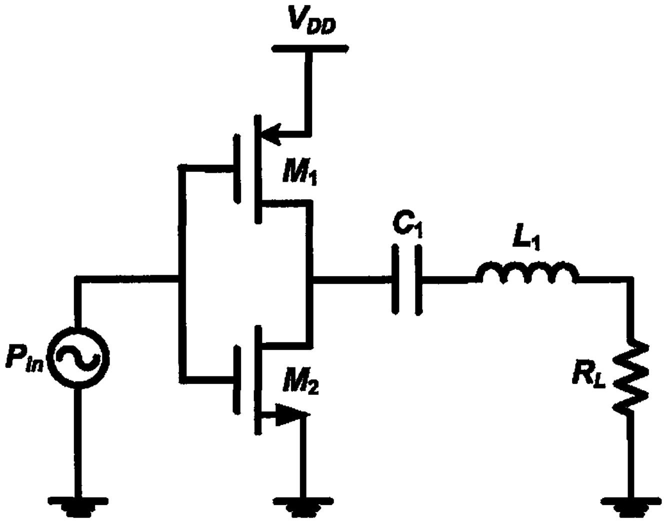

Fig. 5. 8. Circuit schematic of a class D PA (biasing not shown for simplicity).

In class F PAs, the output voltage is shaped into a square wave using harmonic termination tanks. Ideally, this is done using a $\lambda/4$ transmission line at the output. The $\lambda/4$ transmission line appears as a short to all even harmonics and as an open to all odd harmonics, which results in a square wave at the output node. Another alternative to obtain a semi-square waveform is by using second or third harmonic termination tanks, since the harmonic losses are mainly contained in these two harmonics. Figure 5.9 shows the circuit schematics of a class F amplifier with terminating tanks of the second and third harmonic signals.

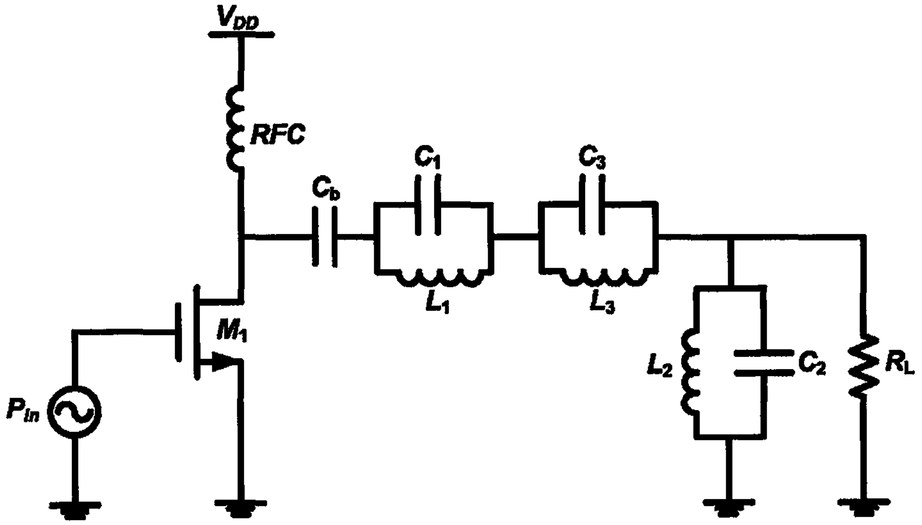

Fig. 5. 9. Circuit schematic of a class F PA (biasing not shown for simplicity).

Figure 5.10 shows a class E PA. The power transistor in this class of operation is ideally driven using a periodic square wave with a 50% duty cycle. During the high state, the transistor is on and current in the RF choke (*RFC*) increases until the input switches to zero. When the transistor turns off, the built-up current charges the parallel capacitor causing the drain voltage to rise. It is a highly tuned circuit where the tuning network at the output is designed to ensure that the capacitor is discharged into the load before the transistor turns on. In a class E PA, the voltage at the output node can reach up to three times the supply, where in linear classes it reaches only two times the supply. This makes Class E PAs more suitable for low voltage operation, especially when a submicron technology is used with a very low breakdown voltage. Readers interested in the detailed operation theory and design of this class of PAs, are referred to [19], where the use of class E PAs is investigated for low-power operation. In [19], another PA operating mode, the mode-locking PAs, is suggested to solve the limitation of the required high input drive in switch mode classes. In these PAs, the amplifier acts as an oscillator with its output frequency locked to the input frequency.

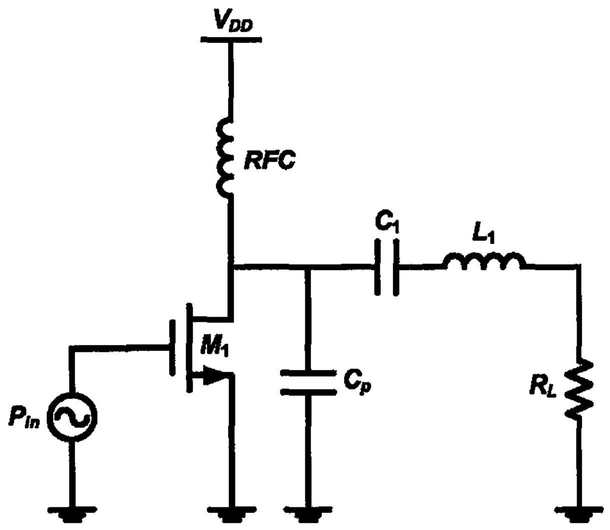

Fig. 5. 10. Circuit schematic of a class E PA (biasing not shown for simplicity).

5.2.3 Comparison of PA Operation Classes

Table 5.1 presents a comparison between the different classes of PA operation. As is shown in the table, class A PAs are the most linear and provide the highest gain, however they only provide up to 50% efficiency. This class of PAs is usually used as driver stages in multi-stage PAs to boost the RF signal prior to transmission. Classes B and AB provide the best compromise between efficiency and linearity. Class C PAs, like the nonlinear-class PAs E, F and D, provide high efficiency at the expense of poor linearity performance.

Table 5. 1. Comparison between the various PA classes of operation.

PA class of operation	Theoretical efficiency	Linearity	Gain
Class A	≤ 50%	Good	High
Class B	78.5%	Moderate	Moderate
Class AB	50% - 78.5%	Moderate	Moderate
Class C	78.5% - 100%	Poor	Low
Class D	100%	Poor	Low
Class E	100%	Poor	Low
Class F	100%	Poor	Low

5.3 SUMMARY

This chapter has presented an overview of the PA basics. The overview covered their performance metrics and their classes of operation, comparing among linear- and nonlinear-class PAs in terms of efficiency and linearity. It was shown that although nonlinear-class PAs exhibit very high efficiencies, they are known to have poor linearity performance with high input drive requirements.

CHAPTER 6

Low-Power CMOS Power Amplifiers: Design and Test

In this chapter, the design, implementation and experimental test of class AB current-mode PAs for low-power biomedical applications are discussed. Three fully integrated PA circuits have been designed, implemented and measured in this work. The three circuits have been realized in a standard mixed-signal CMOS 0.18 μm technology with six aluminum-copper (AlCu) metal layers. The technology is offered by the Taiwan Semiconductor Manufacturing Company (TSMC) provided to us through the Canadian Microelectronics Corporation (CMC). The first two PAs are designed for 2.4-GHz operation. They differ in that the second is realized using the advanced technology option of a thicker top metal layer (Metal 6) of 2 μm thickness rather than the usual 1 μm. The third PA is optimized for 405-MHz operation and is realized using the thicker top metal layer option. The three PAs have class AB topologies and the layouts of the three circuits have been designed using the approach presented in Chapter 4.

Section 6.1 discusses the challenges of low-power PA designs as opposed to high power PA designs. Section 6.2 presents a simple, systematic design procedure for linear-class low-power PAs. Section 6.3 deals with the schematic and layout design of the 2.4-GHz PAs. The measurement results of the two circuits are also presented in this section. Section 6.4 presents the design and test results of the 405-MHz PA. In this section, the 2.4-GHz and the 405-MHz PAs are compared in terms of their suitability for low-power, short-range applications and the feasibility of their realization as fully integrated PAs in CMOS. Section 6.5 presents a comparison of the PA circuits presented in this work to other previously published low-power CMOS PAs. Finally, Section 6.6 gives the chapter's summary.

6.1 LOW-POWER VS. HIGH PAS

RF PAs are classified, next to their class of operation, according to their output power level. PAs with high output power levels (typically 28-32 dBm) are found in cellular and pager applications, while PAs with output power levels in the range of few milliwatts (<10 dBm) are used in short-range devices. Designing PAs to deliver low output power levels comes with challenges that are significantly different from those arising with PA design for high power applications. For the latter case, linearity is usually very important and there exists a linearity-efficiency design trade-off. BiCMOS, SiGe BiCMOS or the III-V technologies are usually preferred for high-power PAs, since devices realized in these technologies are built on top of higher resistivity substrates and the transistors have higher breakdown voltages. Even if high-power PAs are implemented in a standard digital CMOS technology, they usually appear on a separate die to prevent substrate power coupling to the other RF blocks. As discussed in Chapter 3, CMOS, with its low breakdown voltage and lossy passive components, is a suitable candidate for low-power low-frequency RF ICs. Thus, full integration for low-power PAs is achievable. The two main challenges for low-power PA design are: maximizing the power efficiency and minimizing the chip area.

Efficiencies as high as 44% have been reported for fully integrated CMOS PAs with high output power levels (1 to 2 Watts) [44-47]. On the other hand, achieving high efficiency in fully integrated CMOS PAs with low output power levels is a more challenging task. Low-power PAs usually require more bulky passive components leading to increased losses. Efficiencies of only 15% were reported for low-power fully integrated CMOS PAs [49, 54].

6.2 DESIGN PROCEDURE FOR LOW-POWER CMOS CLASS AB PAS

Generally, the function of the PA is to deliver a specific amount of output power to the transmitting antenna efficiently while providing adequate gain to the input signal and maintaining acceptable linearity for the given application. A typical PA consists of a power stage, also known as the output stage, and a number of gain stages, also known as the driver stages. Figure 6.1 shows the block diagram of a two-stage PA. Figure 6.2

shows a flowchart describing a simple procedure for the design of PAs. The design procedure starts with formulating the design goal. Then, some initial design decisions are taken. The actual circuit design starts with the output stage and the output matching network, then the driver stages, the input and the interstage matching networks.

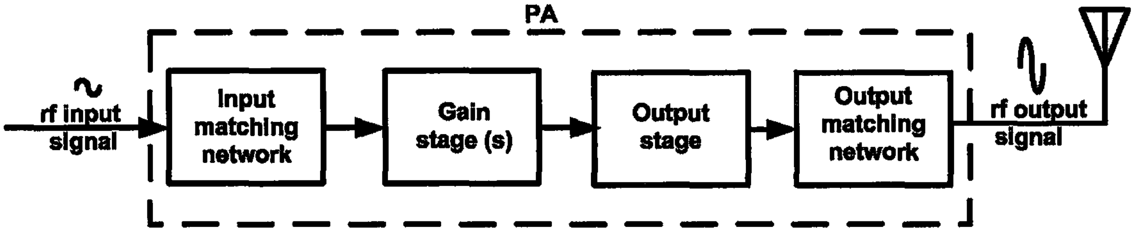

Fig. 6. 1. Block diagram of a two-stage PA.

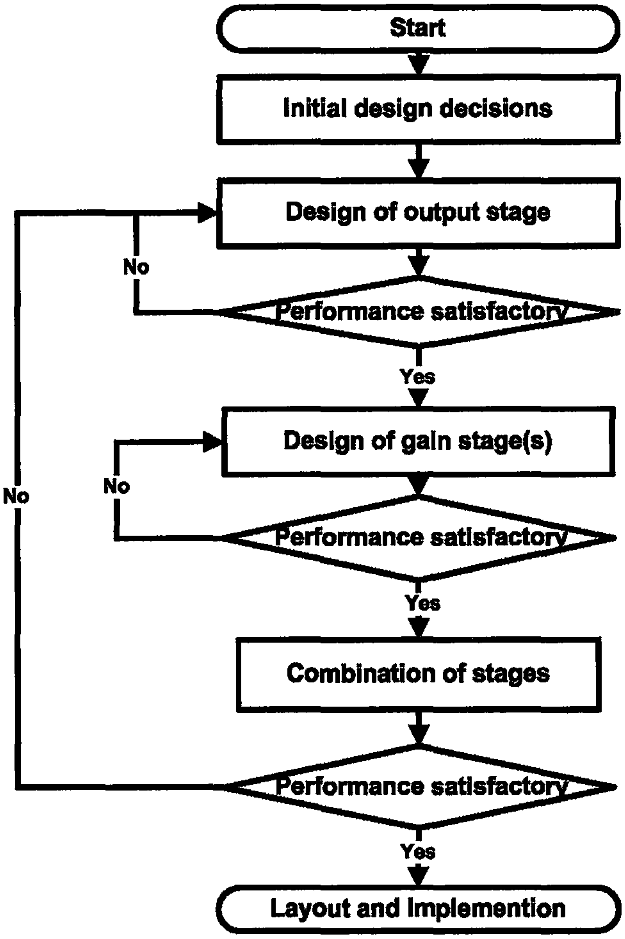

Fig. 6. 2. Flowchart showing the design procedure of low-power PAs.

6.2.1 Design Goal

As for any circuit, the first step in the PA design is formulating a design goal. For low-power, short-range biomedical applications, the design goal can be stated as follows. Over the frequency band of interest, the PA should be:

- highly efficient,
- fully integrated in a standard CMOS technology,
- delivering an output power level in the range of few millwatts,
- matched from its input and output to 50 Ω impedances with all matching networks components on chip,
- providing adequate gain to the input signal,
- operating with a small input drive,
- of small area consumption,
- designed for low voltage operation and
- stable.

In our case, the PA is intended for biomedical applications, where the linearity requirement is relaxed. As discussed in Chapter 2, this is because a simple constant-envelope modulation technique is used. Also, the harmonic content of the output will be greatly suppressed during wave propagation, since the body tissues become very dissipative at high frequencies.

6.2.2 Initial Design Decisions

Before starting the actual circuit design, some initial design decisions have to be made. These involve the following:

- choosing whether to use a single-ended or a differential topology,
- choosing a suitable class of operation (individual stages can be realized in different classes),
- determining the gain and efficiency budgets for the required amount of output power and
- deciding for the number of necessary gain stages for a given gain and efficiency budget.

6.2.3 Design of the Power Stage

The power stage (output stage) has the function of delivering a constant output power to the load at minimum current consumption. Figure 6.3 shows a simplified linear-class output stage. Transistor M_1 is referred to as the power transistor. According to the gate bias voltage of M_1, the PA operates in either class A, B, AB or class C mode. L_o and C_o represent the output matching network and L_1 and C_1 the output filter network. The filter network is used to filter out the higher order harmonics, if high linearity was essential.

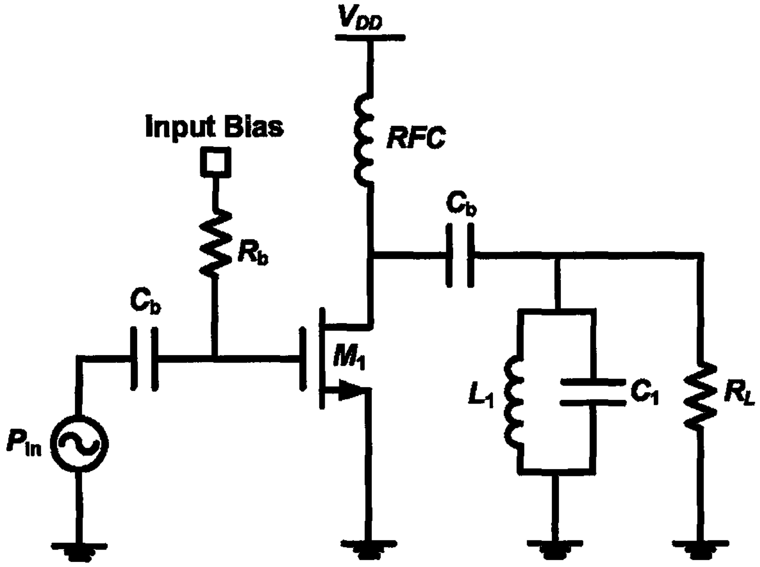

Fig. 6. 3. A linear-class PA output stage.

Given the amount of the required output power to be delivered to the antenna P_{out}, the first step is to estimate the optimum load impedance that is to be seen by the output transistor (R_{OPT}). R_{OPT} is determined from

$$R_{OPT} = \frac{(V_{DD} - V_k)^2}{2 \times P_{out}}. \quad (6.1)$$

Here, V_{DD} is the available supply voltage and V_k is the transistor's knee voltage. For example, for an output power level of 5 mW, R_{OPT} is calculated to be 100 Ω, assuming a supply voltage of 1.5 V and a knee voltage of 0.5 V.

The next step is to design the output matching network, L_o and C_o. The values of these components are chosen as to compromise between realizing the optimum load impedance to be seen by the output transistor, and realizing the required level of output matching to the antenna.

After designing the output matching network, the next step is to design the power transistor M_1. The design involves choosing the proper width and biasing condition of the transistor and choosing the proper input drive level. These are chosen in such a way as to realize the required output power while minimizing the power dissipation in the active device. In this way, the drain efficiency, previously defined in (5.4), can be maximized. For example, targeting 50% efficiency, the dynamic power sets a current limit of 6.67 mA for a 5 mW output power at a 1.5 V supply.

Finally, if an output filter is to be used, it is designed at the frequency of operation. However, filter networks realized on chip, are very lossy and cause the efficiency of the amplifier to degrade significantly. Hence, their use should be avoided if linearity is not crucial for the application.

6.2.4 Design of the Gain Stage(s)

To provide the output stage with the required input drive level, a number of gain stages are used to boost the magnitude of the available RF signal. The design of each driver stage follows that of a simple gain stage with the main aim of achieving the highest gain while minimizing the current consumption. In a linear-class gain stage, the active device is biased either for class A or class AB operation for best gain-efficiency compromise.

Conjugate matching is needed to ensure maximum power transfer. Assuming that a single gain stage is required, only the input needs to be matched to 50 Ω and a passive matching network is required at the input. Matching at the output is not necessary, since the amplifier is going to be connected to the power stage, which has a capacitive input impedance.

6.2.5 Combination of Stages

For best power transfer between the PA stages, the various stages are combined with the proper interstage matching networks. Now, the biasing circuits are designed and the circuit components are fine-tuned for best performance. In the step of combining the various stages, the main goal is achieving the best PAE rather than the best drain efficiency, taking the gain of the PA into account. If the performance is still not satisfactory, the previous steps are repeated until the desired performance is achieved. Finally, the stability performance of the amplifier is checked.

6.3 Power Amplifiers for 2.4-GHz Operation

6.3.1 Schematic Design

Figure 6.4 shows the schematic diagram of the designed 2.4-GHz PA circuit. The PA topology was chosen to be single-ended. Differential amplifiers are advantageous over single-ended amplifiers in their higher gain and better linearity. However, this is achieved at the expense of increased system complexity and hence, increased power consumption. Since the power consumption in this application is of utmost importance, the PA circuits presented here were chosen to have a single-ended topology. In this case a balun is to be used to connect the circuits to the differential loop antenna investigated in this work.

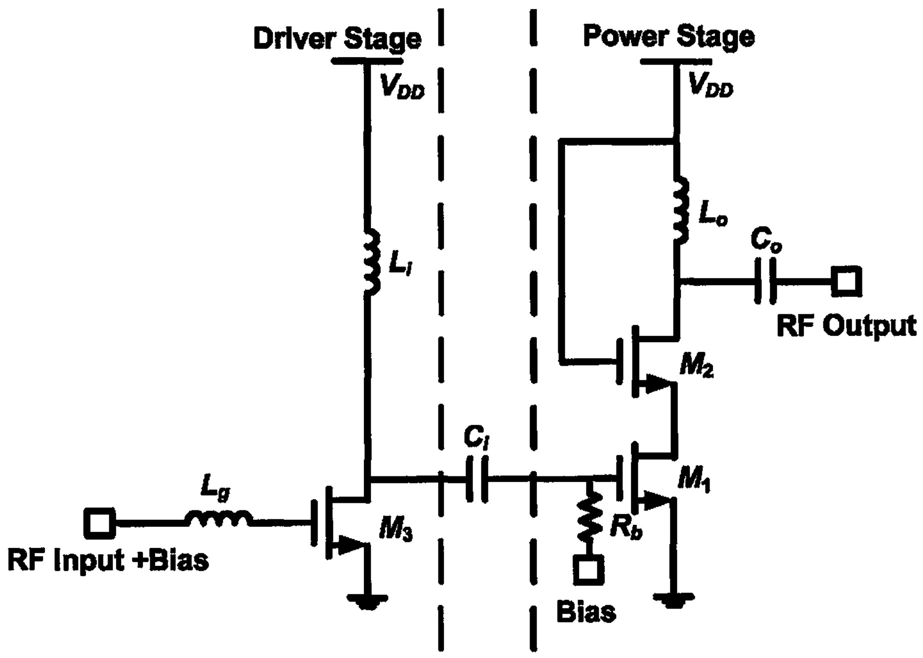

Fig. 6. 4. The complete two-stage 2.4-GHz PA circuit.

Although maintaining a high linearity was not important for the targeted application, a linear topology was chosen rather than a more efficient switching-mode topology, since it requires less input drive, allowing for higher gain at a reduced current consumption.

For the application under consideration, the PA was required to deliver an output power in the range of few dBm. A gain of 15 dB would be sufficient, and is achievable using a single gain stage. Hence, the resulting circuit consists of two stages: the power stage and a gain stage.

The output stage was designed following the design procedure presented in the previous section. An optimum resistance R_{OPT} of 100 Ω is desired at the output. However, to lower this value of R_{OPT}, and hence facilitate the output matching to a 50 Ω impedance, a cascode transistor (M_2) is added to the output stage. This cascode transistor also reduces the Miller's capacitance and thus provides enhanced stability. The components of the output matching network, C_o and L_o, were chosen to provide the required impedance. The sizes of the power transistor and the cascode transistor were chosen for maximum drain efficiency. For minimum power dissipation in the power stage and hence maximum efficiency, the on-interval of the output transistor should be minimized. This is achieved by biasing the transistor below threshold (class C). However, class C power stages require a large input drive and are highly nonlinear. Hence, for best gain-linearity-efficiency compromise, the bias of the output device (M_1) was chosen close to threshold, resulting in class AB operation. Since the linearity in this design is not a concern, a filter at the output was not required.

The driver stage transistor M_3 was also designed to give class AB operation for good gain-efficiency compromise. Impedance transformation at the input was then performed using inductor L_g at the gate of M_3. We relied on the parasitic gate resistance of M_3 and parasitic series resistance of L_g to realize the necessary real part in the input impedance.

The interstage matching network, C_i and L_i, was designed and the two stages were combined. Biasing to the input stage is designed to be supplied through the input port using an external bias-T, while for providing biasing to the second stage, a large on-chip biasing resistor R_b is used. To check for the stability, a pulse was introduced on the supply voltage to excite the circuit with all the frequencies. If the circuit was unstable, oscillations at the frequency the circuit is unstable at will be observed.

The circuit design was done in the Cadence analog design environment. The Cadence Virtuoso schematic editor was used for schematic entry and the simulations were performed using the Cadence SpectreRF simulator. Transient simulations were used and the output power, drain efficiency, PAE and power consumption were all calculated using the formulas given in Chapter 5. All active and passive components were designed to be fully on-chip. RF MOS transistor models, on-chip square spiral inductor models and MIM capacitor models were used in the simulations. The resulting component values are listed in Table 6.1.

Table 6. 1. Component values of the designed 2.4-GHz PAs.

Component Parameter	Value
L_g	12.82 nH
M_3	14 x 2.5 µm x 0.18 µm
L_i	9.1 nH
C_i	2 pF
R_b	30 kΩ
M_1	68 x 2.5 µm x 0.18 µm
M_2	70 x 2.5 µm x 0.18 µm
C_o	850 fF
L_o	6 nH

6.3.2 Layout Design

The circuit layout was designed using the Cadence Virtuoso layout editor. All passive and active components were laid out in a manner suitable for RF operation. Transistors were laid out in multifinger configuration with a fixed finger width of 2.5 µm to minimize the gate resistance. Inductors have been realized as on-chip square spiral inductors using the top metal layer for minimum losses. The RF pads were realized using Metals 5 and 6 only to minimize parasitic capacitances.

The interconnection wires were designed using the approach described in Chapter 4. The optimization's goal was to achieve minimum degradation in the drain efficiency. During the layout design of the thin-Metal-6 PA, the following was observed regarding the sensitivity of the circuit performance to the metal wires. It was found that the supply node of the gain stage is sensitive to high parasitic resistance, whereas the drain of M_3 is very sensitive to high parasitic capacitance. Drops up to 4 % can occur in the drain efficiency, if these critical nodes were not designed properly. The supply and ground connections of the power stage are very sensitive to high parasitic resistance and can lead to drops in efficiency as high as 10 %. As for the connections at the drain of the cascode transistor M_2 and the output node, both are found to be sensitive to capacitive and parasitic effects. For the connection at the drain of M_2, a metal width of 5 μm resulted from the optimization, and the output node was connected to the pad using an optimized 12-μm wide wire. The photograph of the microchip shown in Fig. 6.5 clearly shows the variability in the wire widths, which resulted from the interconnection optimization. The total area consumption is 1200 μm x 1100 μm.

After the design layout, post-layout and layout-versus-schematic simulations were performed to ensure proper interconnection. We did not rely on post-layout simulations, however, in predicting the performance of the circuit after fabrication. The layout design methodology proposed in Chapter 4 was used, which takes all the layout parasitics into account in the circuit simulations.

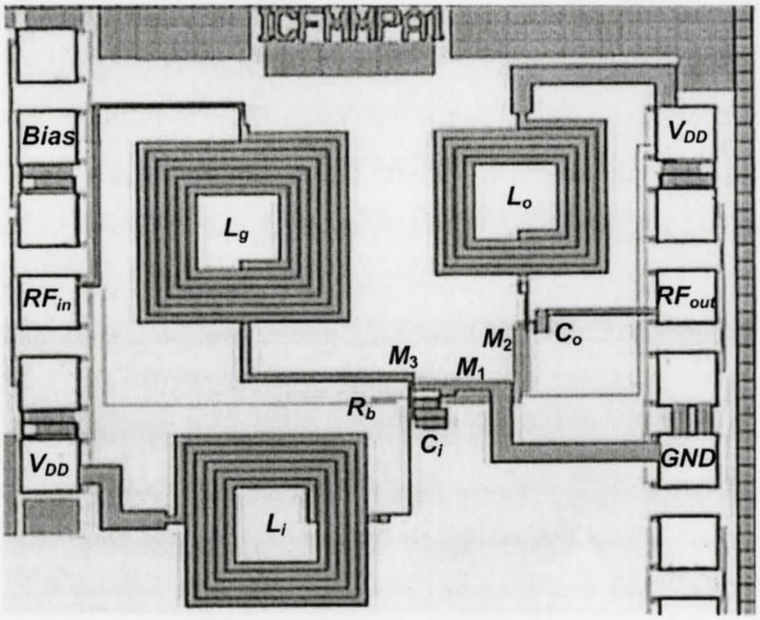

Fig. 6. 5. Chip micrograph of the 2.4-GHz PA circuit.

6.3.3 Measurement Results

The 2.4-GHz PA circuit was fabricated twice. Both prototypes were implemented in the same TSMC 0.18 μm CMOS technology, with the second design different from the first in that it was built using the thicker top metal layer (2 μm) option provided by the foundry. Consequently, the second design suffers from less layout parasitics, and as will be shown later, exhibits a slightly improved performance.

On-wafer measurements were performed on the two chips using a signal generator (Agilent 4422B) to provide the RF input signal, a spectrum analyzer (Agilent E4440A) to measure the RF output power and two on-wafer probe sets. Each probe set consists of 11 tips: 5 DC and 2 ground-signal-ground (GSG) RF probe sets. A semiconductor parameter analyzer (HP-4145B) was used to provide the DC signals to the circuit and to measure its current consumption. Figure 6.6 shows the complete measurements set-up.

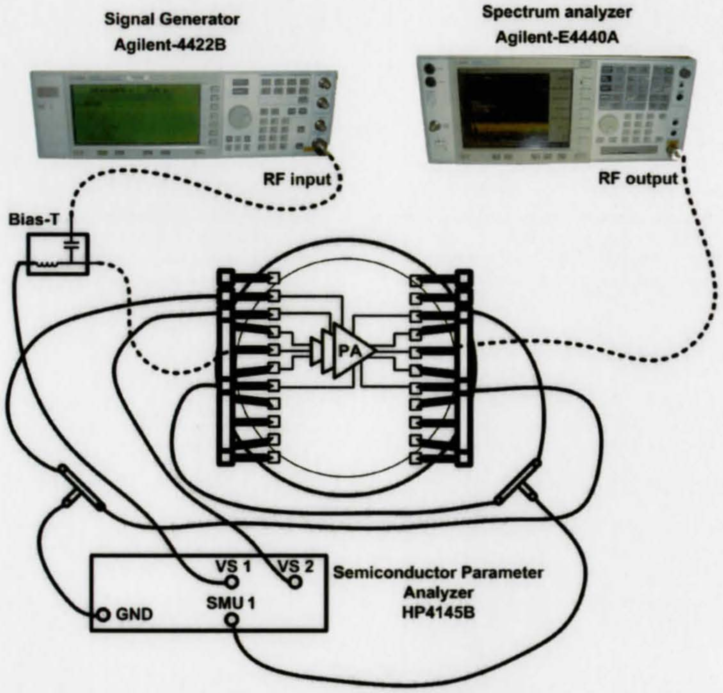

Fig. 6. 6. Experimental set-up used in measuring the 2.4-GHz PA.

Figure 6.7 shows the performance of the PA, which is implemented using the 1-μm top metal layer. The figure shows the measured output power, drain efficiency and

PAE of the PA as a function of the input drive at a supply voltage of 1.4 V. The performance of PAs is usually reported at their gain compression point, where the PAE and output power are maximum. Beyond this point, the PA delivers a constant output power and the gain starts to drop, causing the PAE to decrease. The circuits presented in this work were designed to have low gain compression points for the targeted low-power application, where the signal levels are small. As can be seen from Fig. 6.7, the small-signal gain is about 24 dB. The input power at which compression starts is about -13 dBm. Thus, the previous stage should provide an RF signal of at least -13 dBm. For an input power in the range of -15 to 0 dBm, the PAE is above 25 %. Beyond this value, the circuit enters compression and the PAE starts to drop. At the 1-dB compression point, the PA delivers 6.5 dBm of output power with a PAE of 28% and a current consumption of 11 mA.

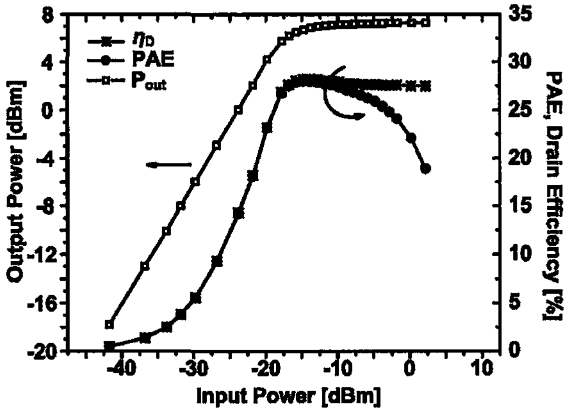

Fig. 6. 7. Measured output power (P_{out}), drain efficiency (η_D) and power-added efficiency (PAE) vs. the input power at 2.45 GHz and 1.4 V supply voltage for the thin-metal design.

Figures 6.8 and 6.9 show a comparison between the ideal simulations (simulations with no parasitics), the more realistic simulations (with all the parasitics included) and the measurements. Figure 6.8 (a) and 6.8 (b) present the output power and drain efficiency, respectively, versus the input power at a supply voltage of 0.8 V. Figure 6.9 presents the frequency response of the circuit at 1.4 V supply and -13 dBm input drive. The figures clearly show that the ideal simulations differ significantly from the actual measurements. Nevertheless, after taking all the significant layout parasitics into account, a good match is obtained between simulations and measurements.

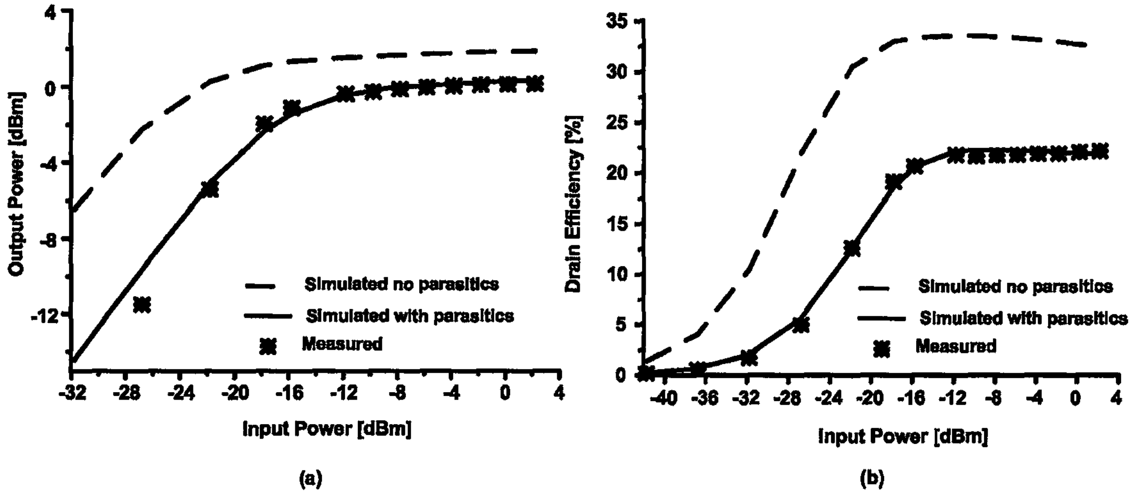

Fig. 6. 8. Comparison between the ideal simulations, simulations with layout parasitics and measurements of (a) the output power and (b) the drain efficiency vs. the input power at 0.8 V supply and 2.45 GHz.

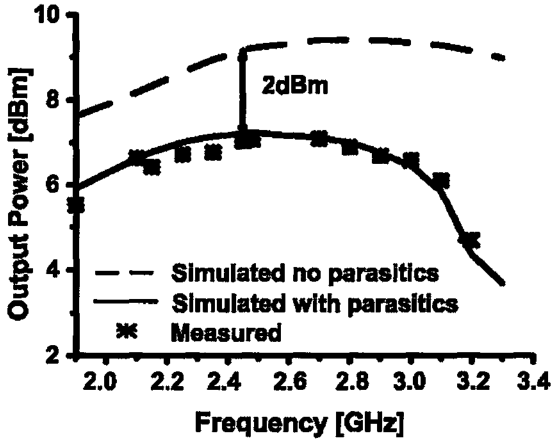

Fig. 6. 9. Comparison between the ideal simulations, simulations with the layout parasitics and measurements of the frequency response of the circuit at a supply of 1.4 V and -13 dBm input power.

Figure 6.10 shows the measured output power and drain efficiency as a function of the supply voltage. The supply voltage was swept from 0.6 V to 1.8 V at an input power of -13 dBm. As can be seen from the figure, the output power and the drain efficiency increase with the increased supply as given by (6.1). The circuit can operate at a supply voltage as low as 0.8 V, delivering 0.6 mW of output power with 16 % drain efficiency.

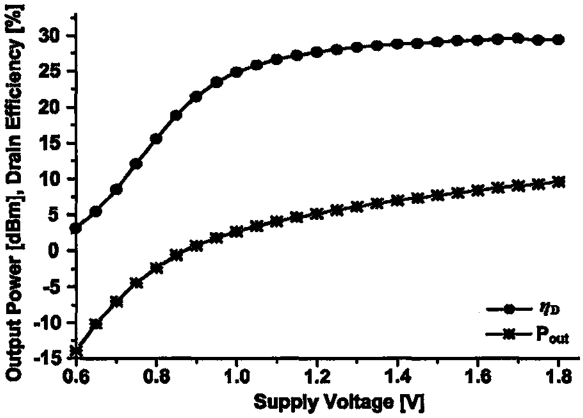

Fig. 6. 10. Measured output power (P_{out}) and drain efficiency (η_D) vs. supply voltage at 2.45 GHz and −13 dBm input power.

Figure 6.11 shows the measured output power (a) and PAE (b) versus the input power for various supply voltages at an input frequency of 2.45 GHz. With the increasing supply voltage, the 1-dB compression point slightly increases, showing a slight improvement in the linearity. Also, the range of input power levels for which the PAE is relatively close to its maximum is increased due to the improvement in the power gain, which is clear from Fig. 6.11 (b).

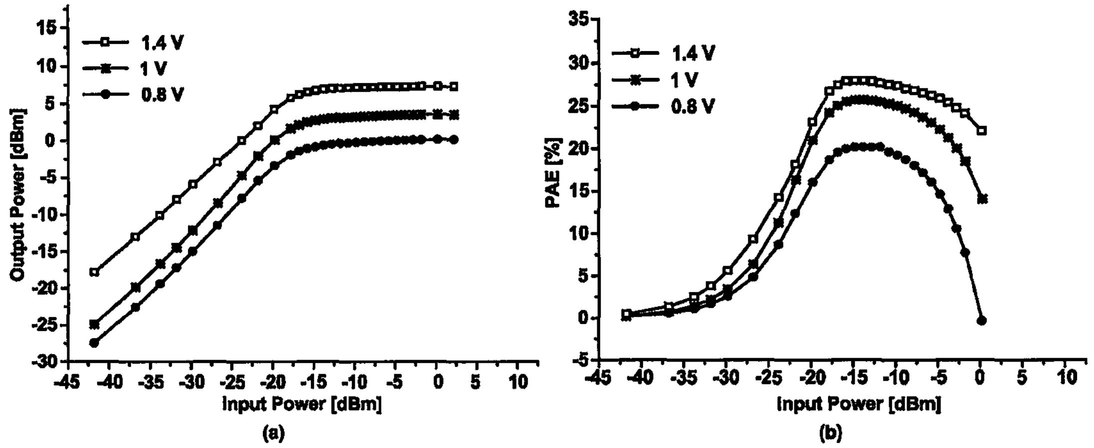

Fig. 6. 11. Measured (a) output power and (b) PAE vs. input power at 2.45 GHz for various supply voltages.

Linearity is evaluated here in terms of the 1-dB compression point and the third to first order harmonic levels. The output spectrum at 1.4 V supply and -13 dBm input drive is shown in Fig. 6.12. The second and third-order harmonic signals are 20 dB and 16 dB below carrier, respectively. As previously mentioned, linearity is not a concern in this design, since a constant-envelope modulation technique is going to be used.

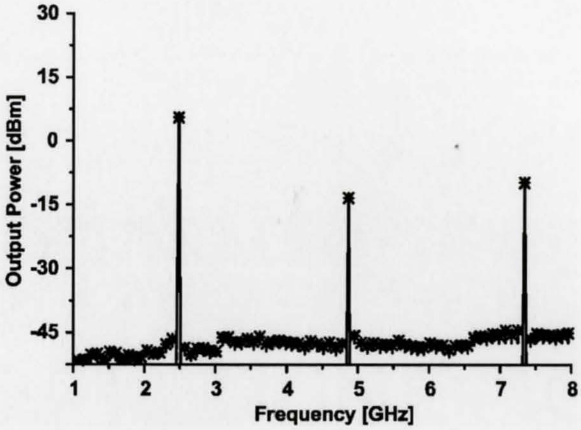

Fig. 6. 12. Frequency spectrum of the PA circuit at 1.4 V voltage supply operation and -13 dBm input drive.

As was discussed in Chapter 3, the use of a thicker top metal layer will allow for higher quality inductors and lower resistive losses of the interconnection wires. This in turn will allow for an improved circuit performance. The same PA circuit presented above was laid out once more using a top metal layer of 2-μm thickness. Figure 6.13 shows a magnified view of the output capacitor in the chip micrograph and the increased thickness of the top metal layer is visible in Fig. 6.13 (b). The measured performance of the circuit is shown in Fig. 6.14. The figure shows that at the 1-dB compression point, the PA delivers 7.2 dBm of output power with a PAE of 30.2 % and a current consumption of 12 mA.

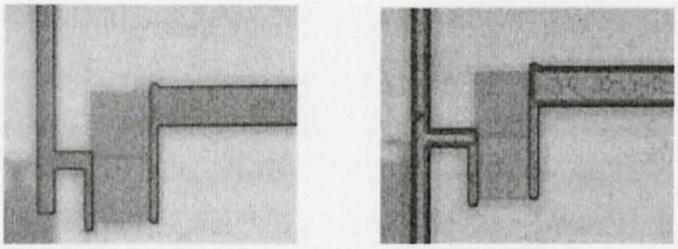

(a) (b)

Fig. 6. 13. Zoomed-in view of the output capacitor showing the top metal layer with: (a) 1-μm thickness and (b) 2-μm thickness.

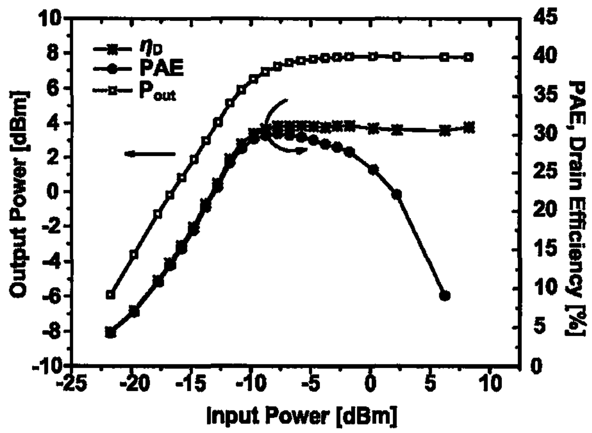

Fig. 6. 14. Measured output power (P_{out}), drain efficiency (η_D) and power-added efficiency (PAE) vs. the input power at 2.45 GHz and 1.4 V supply voltage for the thick top-metal design.

Figures 6.15 to 6.17 show comparisons between the two designs for various performance characteristics of the measured P_{out}, η_D *and* PAE versus P_{in}, respectively. In the thick top-metal design, the input power at which compression starts is about -8 dBm showing an improvement in the amplifier linearity when compared to the thin top-metal design. This is mainly due to the increased DC headroom. The improved linearity in turn results in a reduction in the small-signal gain. When compared to the thin metal design, the thick metal design exhibits a reduced small-signal gain showing a gain of 17 dB. This reduction in the small-signal gain is not significant, since the PA is designed for large signal operation and what is important is the performance beyond compression. As long as the gain at the compression point is well above 10 dB, it is ensured that the PAE will be close to the drain efficiency. The output power is increased by 0.7 dB, corresponding to an increase of 4% in the drain efficiency. As shown in Fig. 6.17, the two circuits operate almost over the same bandwidth. The measured performance of two circuits (thick and thin top-level metal) at their gain compression points is summarized in Table 6.2 at a frequency of operation of 2.45 GHz.

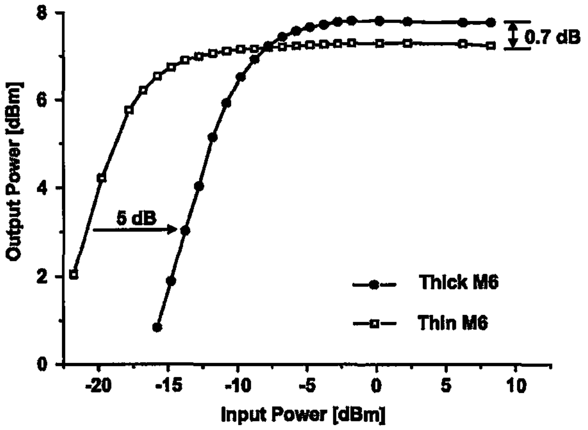

Fig. 6. 15. Comparison between the output powers vs. the input power of the two 2.4-GHz PAs showing the improvements resulting from the increase in the top metal layer thickness.

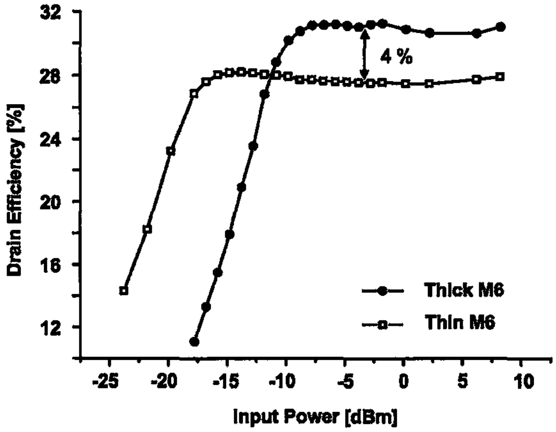

Fig. 6. 16. Comparison between the drain efficiencies vs. the input power of the two 2.4-GHz PAs showing the improvement resulting from the increase in the top metal layer thickness.

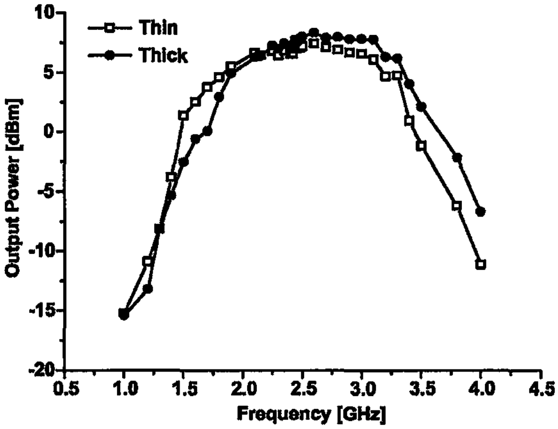

Fig. 6. 17. Comparison between the output powers vs. the input frequency of the two 2.4-GHz PAs.

Table 6. 2. Summary of the measured performances of the 2.4-GHz prototype circuits showing the improvements resulting from the increase in the top metal layer thickness.

	Thin M6	Thick M6
Supply voltage [V]	1.4	1.4
Output power [dBm]	6.5	7.2
Current consumption [mA]	11	12
Gain compression point (CP)	-13	-8
S_{11} [dB]	-9	-7
S_{22} [dB]	-12	-16
PAE @ CP [%]	28	32
Small-signal gain [dB]	24	17

6.4 Power Amplifier for 405-MHz Operation

It is known that RF circuits of improved performance and lower power consumption are more easily achievable at low frequencies than at higher frequencies [50]. However, inductors used in low frequency designs are very bulky. When these are realized in CMOS, they perform very poorly due to the increased coupling to the substrate. To realize a PA circuit for low-frequency operation and with reasonable area consumption, we decided to sacrifice the gain and use a single-stage PA. Reducing the gain was possible for this application, since the required output power level is relatively low. The circuit schematic of the single-stage 405-MHz PA is shown in Fig. 6.18.

The circuit design followed the output stage design procedure described in Section 6.2. To maximize the gain from a single stage, no cascode transistor was used. Biasing is supplied to the circuit through the input port using an external bias-T. Again, class AB operation was chosen for best gain-efficiency compromise and the Cadence RF design package was also used. The component values resulting from the simulations are listed in Table 6.3.

At such a low frequency, the layout parasitics become less prominent. Nevertheless, the layout was designed using the approach described in Chapter 4. Transistors were designed with multifinger gates, inductors were realized using the top metal layer in square spiral form, capacitors as MIM capacitors and RF pads were constructed using the top two metal layers. The layout was realized using the thick top-metal layer option provided by the foundry. The chip micrograph is shown in Fig. 6.19. The layout was designed for differential measurements. But, since we wanted to evaluate the circuit performance without including the losses in the balun, only one side of the layout was measured. The total die area of the single ended PA is 700 μm x 1600 μm.

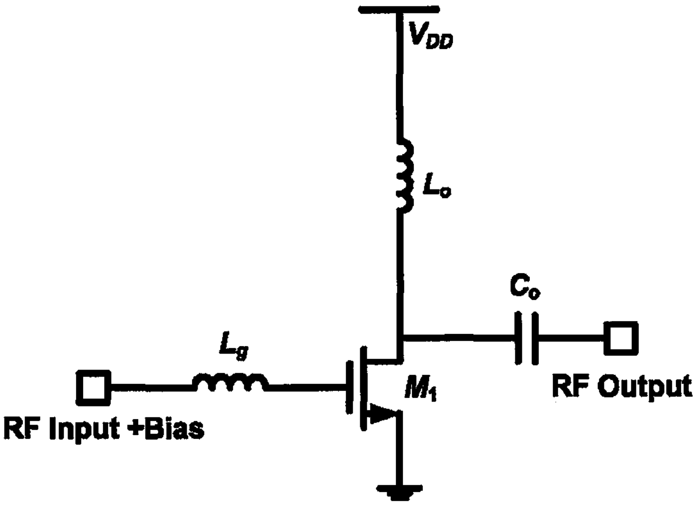

Fig. 6. 18. The single-stage 405-MHz PA circuit.

Table 6. 3 Component values of the designed 405-MHz PA.

Component Parameter	Value
L_g	2.4 nH
M_1	100 x 2.5 μm x 0.18μm
C_o	6 pF
L_o	24.6 nH

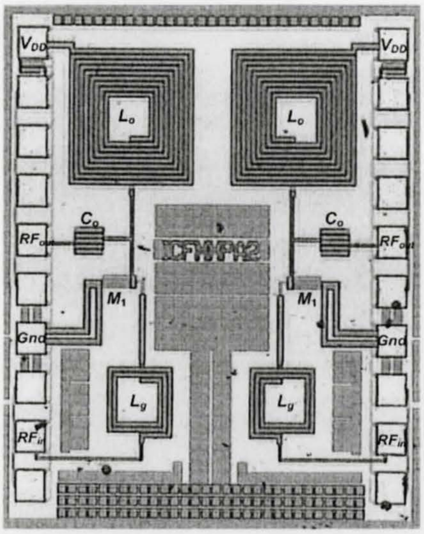

Fig. 6. 19. Chip micrograph of the 405-MHz PA circuit.

6.4.1 Measurement Results

Figure 6.20 shows the experimental set-up used in the 405-MHz measurements and Fig. 6.21 shows the output power, drain efficiency and PAE of the circuit as a function of the input power at 1.4 V supply voltage and 405-MHz input frequency. The circuit is capable of delivering up to 8 dBm of output power with a drain efficiency of 40%. The PAE, however, is only 32.6%, which is mainly due to the reduced gain of the circuit, since only a single stage was used.

Figures 6.22 to 6.24 compare the two PA circuits operating at 2.4 GHz and 405 MHz implemented using the thick top-metal layer. The 405-MHz design exhibits an increase in the 1-dB gain compression point, hence improved linearity. This is mainly due to two reasons; the first is that the gain itself in the 405-MHz design is lower and second is that the 2.4-GHz design uses a cascode topology, which reduces the DC headroom causing a reduction in the linearity. The 405-MHz design also shows significantly higher drain efficiency, since (1) power is only consumed in a single stage, (2) the losses are reduced at lower frequencies, and (3) no cascode transistor was used. However, the increase in the PAE is not as high, since the circuit has a much lower gain performance. During the measurements, it was noted that the 405-MHz design is not band-limited and operates at frequencies up to 4 GHz, showing a bandwidth much higher than the 2.4-GHz circuit. This is mainly because the inductors used in this design were very large with very low quality factors. Table 6.4 compares the performance of two circuits at 1.4 V supply voltage and at their input gain compression point. As shown in the table, the 405-MHz design occupies a larger area than the higher frequency design, since larger inductors are needed.

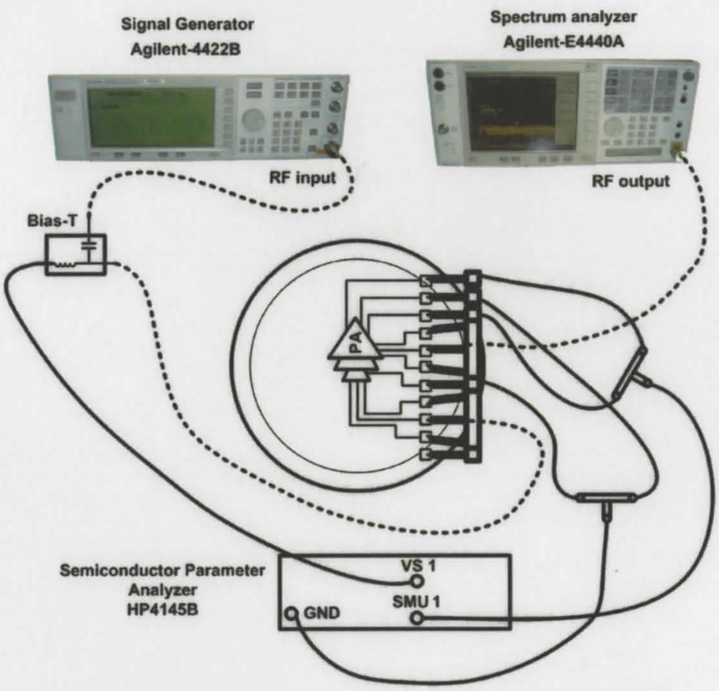

Fig. 6. 20. Experimental set-up used in measuring the 405-MHz PA.

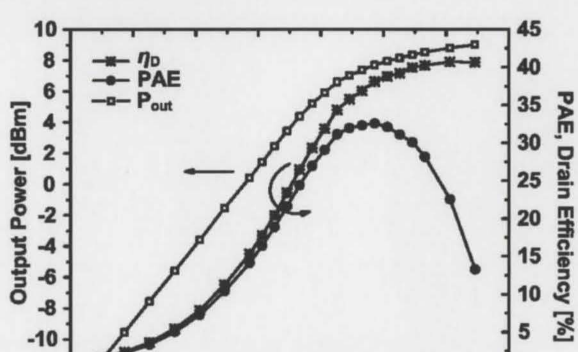

Fig. 6. 21. Measured output power (P_{out}), drain efficiency (η_D) and power-added efficiency (PAE) vs. the input power at 405 MHz and 1.4 V supply voltage.

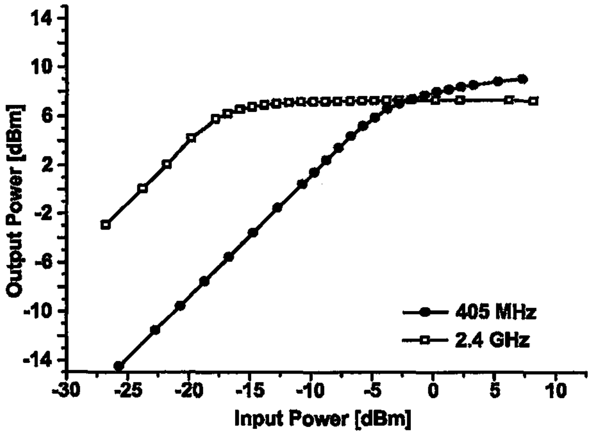

Fig. 6. 22. Comparison between the output powers vs. the input power of the 2.4-GHz and the 405-MHz PAs.

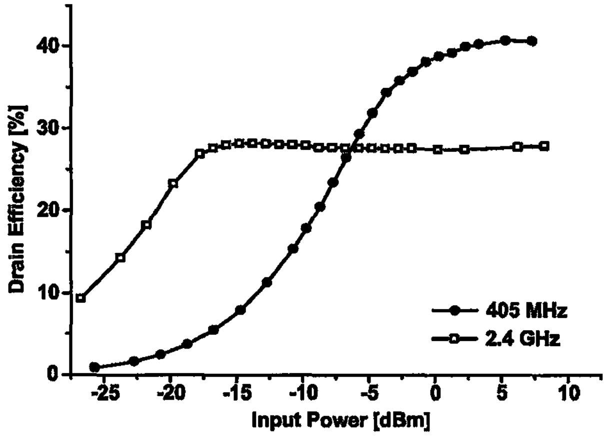

Fig. 6. 23. Comparison between the drain efficiencies vs. the input power of the 2.4-GHz and the 405-MHz PAs.

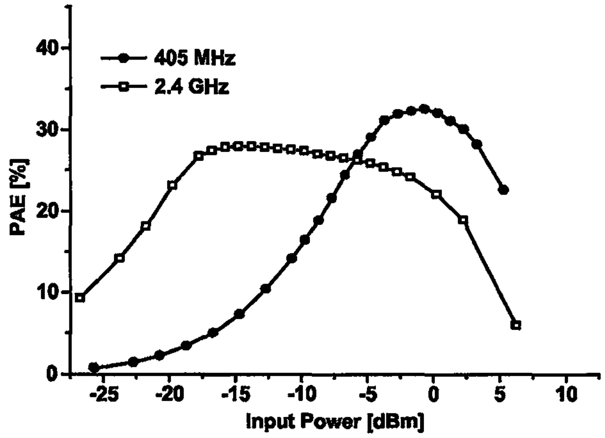

Fig. 6. 24. Comparison between the PAEs vs. the input power of the 2.4-GHz and the 405-MHz PAs.

Table 6. 4 Comparison between performance characteristics of the 2.4-GHz and the 405-MHz PAs.

	2.4-GHz PA	405-MHz PA
Area [mm^2]	1.2 x 1.1	0.7 x 1.6
Number of stages	2	1
Maximum output power [dBm]	7.2	8
Current consumption [mA]	12	11
Small-signal gain [dB]	17	11.2
1-dB CP [dBm]	-8	-1
Maximum PAE [%]	30.2	32.6
Maximum drain efficiency [%]	32	40.7

6.5 Comparison to Previously Published PAs

Table 6.5 compares the performance of the PA circuits presented in this work to other published low-power, linear-class CMOS PAs. As can be seen from the comparison, the performance of the circuits presented in this work, although fully on-chip, is superior to other designs using off-chip components. The FoM previously expressed in equation (5.7) is included in the comparison. It is worth mentioning that this FoM does not take the level of integration into account. Conversely, it is a strong function of the frequency of operation; hence the 405 MHz design shows a lower FoM than the remaining circuits.

6.6 Summary

In this chapter, we have presented the circuit, layout design and measured performance of the three designed linear-class PA circuits, which are intended for low-power biomedical applications. The first two are designed for 2.4-GHz operation, while the third is optimized for the operation in the MICS frequency band (403-405 MHz). The three circuits are fully integrated with all passive components in CMOS to fulfill the area requirements of the application. The layouts of the three circuits were designed using the approach described in Chapter 4. Designing the layout of the PA circuit using this parasitics-aware approach resulted in high-performance CMOS PAs with measured performance characteristics in good agreement with simulated results. Therefore, through this work, it has been shown that linear-class PAs, when carefully designed, are well-suited for low-power, short-range biomedical applications.

Table 6. 5 Performance comparisons between low-power linear-class PAs.

	Tech. [μm]	V_{DD} [V]	Freq. [GHz]	P_{out} [dBm]	PAE [%]	FoM [dB]	Integration
S.-J. Yoo [51]	0.5	3	0.433	13	29	184	Off-chip components
T. Melly et. al [52]	0.5	1.2	0.433	4	15	n. a.	Off-chip components
K. Yamamoto [53]	0.18	1.8	2.4	9	16	199	Off-chip components
Y. H. Chee et. al [48]	0.13	1.2	1.92	4	26	187	Off-chip components
A. Zolfaghari et. al [49]	0.25	2.5	2.4	0	13.3	n. a.	Fully on-chip
P. B. Khannur [54]	0.18	1.8	2.45	3.5	14	192	Fully on-chip
This work thin 2.4-GHz design	0.18	1.4	2.45	6.5	28	202	Fully on-chip
This work thick 2.4-GHz design	0.18	1.4	2.45	7.2	30.2	197	Fully on-chip
This work 405-MHz design	0.18	1.4	0.405	8	32.6	178	Fully on-chip

CHAPTER 7

In-Body Radiation

EM fields are known to interact with the human body, resulting in various hazardous biological effects. These biological effects vary with frequency. Figure 7.1 shows the hazardous biological effects of EM radiation at various frequencies [55]. As indicated in the figure, the thermal effect is the main biohazardous effect in the RF range (300 MHz – 3 GHz). There, the EM power is absorbed by the exposed biological tissues whose temperature increases as a result.

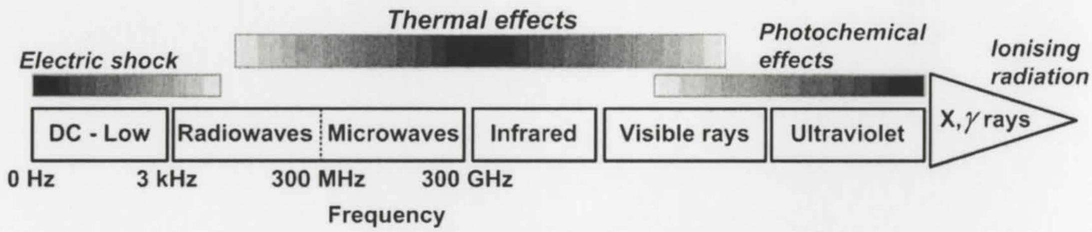

Fig. 7. 1. Various biohazardous effects of EM fields as a function of frequency [55].

To protect people from the thermal damage of their tissues due to excessive RF field exposure, special committees and organizations have been formed with the goal to develop strict safety standards, which regulate the amount of EM fields that a human being can be exposed to. The specific absorption rate (SAR) is the most popular quantity used to assess body exposure to RF fields. In designing wireless devices for the various types of applications, compliance with SAR limits must be verified either numerically, experimentally, or both. Modeling of the human body is an essential step in developing the compliance requirements. Realistic numerical and experimental models (phantoms) of the human body have been developed for the purposes of human exposure assessment.

To be able to design and characterize antennas for implanted transceiver systems, a thorough understanding of the nature of the complex human body as a radiation environment is essential. Besides, one must be familiar with the regulations and standards on the body exposure to RF fields. The aim of this chapter is to discuss various aspects of the radiation from implanted sources. The chapter is organized as follows. Section 7.1 presents the frequency-dependent electrical constitutive parameters of the body tissues. Section 7.2 introduces the SAR as the main quantity used to describe the absorbed power in biological tissues at RF. Section 7.3 introduces the safety standards, highlighting the important limits that should be followed in our case. Section 7.4 describes the existing procedures and regulations for evaluating numerical and experimental dosimetry. Section 7.5 presents the concept of modeling the human body, highlighting both numerical and experimental phantoms. Finally, in Section 7.6, a summary of the chapter is given.

7.1 Electrical Properties of Biological Tissues

The body constitutes a strongly dissipative, heterogeneous, dielectric medium characterized by the relative permittivity ε_r and specific conductivity σ of its tissues. Medical imaging data and experimental investigations show that more than 30 types of biological tissues can be identified in the human body [56]. The structure and the number of the involved biological tissues depend on the anatomy of the exposed part of the body. To be able to analyze the interaction between the EM waves and the human body, the electric properties of the body tissues must be studied. Subsection 7.1.1 lists the EM constitutive parameters and the equations needed to describe the field behavior in a lossy material. Subsection 7.1.2 discusses the electrical behavior of the biological tissues based on data collected from the literature.

7.1.1 Overview of EM Constitutive Parameters and Equations

The dielectric properties of a material determine its response to the EM fields. These are mainly represented by the complex permittivity $\hat{\varepsilon}$ and the specific conductivity σ (S/m) of the medium, where $\hat{\varepsilon}$ is given by

$$\hat{\varepsilon} = \varepsilon' - j\varepsilon'', \tag{7.1}$$

$$\varepsilon' = \varepsilon_0 \varepsilon_r, \tag{7.2}$$

where ε' is the permittivity of the material, ε'' is its dielectric loss factor and ε_0 is the permittivity of free space (8.85×10^{-12} F/m). The ratio $\varepsilon''/\varepsilon'$ is known as the dielectric loss tangent. Assuming a time-harmonic field, the propagation constant k in a lossy medium is given by

$$k = j\omega\sqrt{\mu_0\varepsilon'\left(1-j\left(\frac{\varepsilon''}{\varepsilon'}\right)-j\frac{\sigma}{\omega\varepsilon'}\right)} = \alpha + j\beta, \tag{7.3}$$

where ω is the angular frequency of the incident wave in rad/s and μ_0 is the permeability of free space ($4\pi\times10^{-7}$ H/m). Also, α is the attenuation factor and β is the phase constant; and are expressed as

$$\alpha = \omega\sqrt{\frac{\mu_0\varepsilon'}{2}}\left(\sqrt{1+\left(\frac{\varepsilon''}{\varepsilon'}\right)+\left(\frac{\sigma}{\omega\varepsilon'}\right)^2}-1\right)^{1/2}, \tag{7.4}$$

$$\beta = \omega\sqrt{\frac{\mu_0\varepsilon'}{2}}\left(\sqrt{1+\left(\frac{\varepsilon''}{\varepsilon'}\right)+\left(\frac{\sigma}{\omega\varepsilon'}\right)^2}+1\right)^{1/2}. \tag{7.5}$$

The distance at which the wave intensity falls to $1/e$ of its incident value, is known as the penetration depth δ and is given by

$$\delta = \frac{1}{\alpha} = \frac{1}{\omega}\left[\left(\frac{\mu_0\varepsilon_r\varepsilon_0}{2}\right)\left(\sqrt{1+\left(\frac{\sigma}{\omega\varepsilon_r\varepsilon_0}\right)^2}-1\right)\right]^{-1/2}. \tag{7.6}$$

7.1.2 Review of the Dielectric Behavior of Biological Tissues

The various tissues in the human body differ in their chemical and biological structures, which results in their distinct dielectric properties. The body tissues have practically no magnetic properties.

The electrical properties of biological tissues have been investigated using various laboratory measurements and results are available in the literature for most body tissues [57-59]. In [57], a collection of previous experimental results from the literature is given.

In [58], the same group used three different experimental techniques that cover overlapping frequency ranges to measure the electrical properties of 30 biological tissues. In the third and the last phase of their project [59], they developed a parametric model of the frequency dependence of the electric properties of 17 types of body tissues. Using these results, they provided an on-line applet [56] that generates the dielectric properties of most of the body tissues in the frequency range of 10 Hz to 20 GHz. Using this applet, curves of the relative permittivity ε_r, conductivity σ and the penetration depth δ of different tissue types (muscle, fat, and small intestine) were generated over the 300 MHz - 3 GHz frequency range (Fig 7.2 to 7.4). As can be seen from the three figures, the electrical properties of the various tissue types are frequency dependent and dissipative at RF. Table 7.1 lists the electrical parameters and the mass density of almost all tissue types at 2.4 GHz and 405 MHz, which are the two frequencies of interest in this work.

In summary, the problem of RF wave propagation inside the human body is a complex radiation problem. The radiated EM waves interact with the cells and the molecules that the biological tissues are composed of, and are reflected and scattered at boundaries between the different types of tissues. The resulting field distribution is very complex and depends on the frequency of the incident wave and on the anatomy of the body (types of tissues in the path of the wave and the tissue structure of the exposed body part). In the particular case of internal RF radiation from biomedical implants, the tissues are in the near field zone of the radiating source. Knowing that the wave penetration depth in the body tissues is very small, one can expect that any radiated signal will be greatly attenuated and the human body will perform badly as a communication medium due to very high losses.

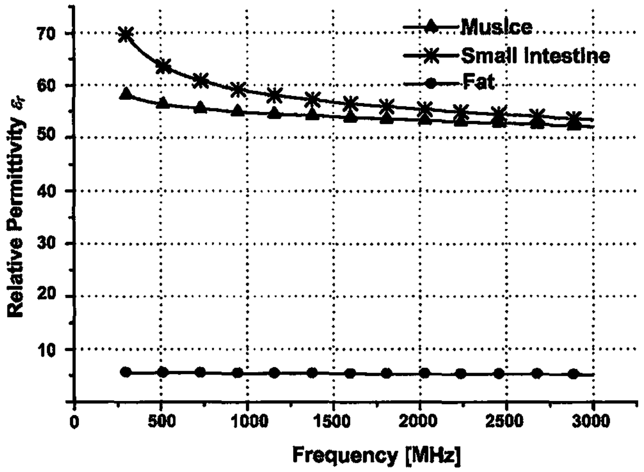

Fig. 7. 2. Relative permittivity of muscle, fat and small intestine tissues vs. frequency [56].

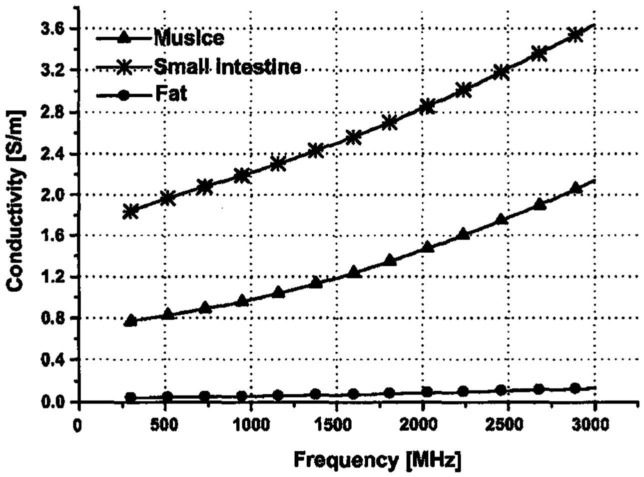

Fig. 7. 3. Conductivity of muscle, fat and small intestine tissues vs. frequency [56].

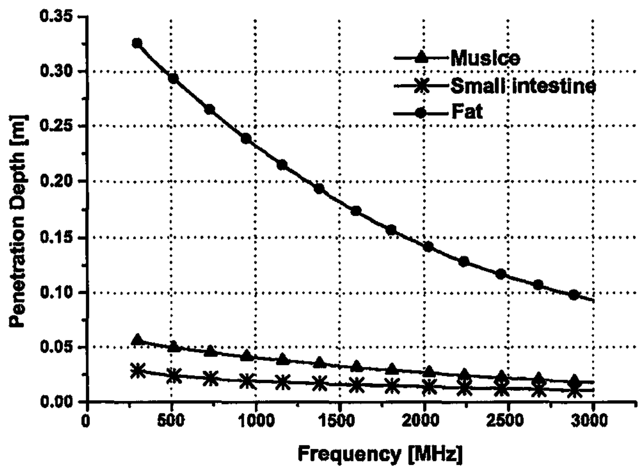

Fig. 7. 4. Wave penetration depth in muscle, fat and small intestine tissues vs. frequency [56].

Table 7. 1. The mass density [60] and the electrical parameters [56] of almost all body tissues at 2.4 GHz and 405 MHz.

		2.4 GHz		405 MHz	
Body Tissue	**Mass Density ρ [10^3 kg/m^3]**	ε_r	σ[S/m]	ε_r	σ[S/m]
Brain	1.04	42.6	1.48	49.6725	0.59287
Bone	1.96	15.008	0.5861	17.775	0.163665
Bone Marrow	1.04	5.3024	0.092834	5.6696	0.029365
Bladder	1.03	18.026	0.67265	19.7	0.32713
Blood	1.06	58.347	2.5024	64.127	1.3513
Body Fluid	1.01	68.24	2.4392	69	1.53
Cartilage	1.1	38.878	1.7172	45.417	0.58813
Cerebro Spinal	1.01	66.319	3.4122	70.939	2.2525
Colon	1.04	53.969	1.9997	62.501	0.86009
Eye Sclera	1.03	52.698	1.9967	57.627	1.0058
Fat	0.92	5.2853	0.10235	5.5777	0.041199
Gall Bladder	1.03	57.68	2.023	61.176	1.1393
Gland	1.05	57.272	1.9283	61.514	0.87851
Heart	1.03	54.918	2.2159	65.975	0.96749
Kidney	1.05	52.856	2.3901	66.268	1.0978
Liver	1.03	43.118	1.6534	51.147	0.65595
Lung	1.05	34.482	1.21941	39.1495	0.530165
Lymph	1.04	57.272	1.9283	61.514	0.87851
Mucous	1.04	42.923	1.5618	49.819	0.67076
Muscle	1.05	52.791	1.705	57.088	0.79759
Nail	1.03	11.41	0.38459	13.136	0.09178
Nerve	1.04	30.196	1.0681	35.351	0.44803
Pancreas	1.04	57.272	1.9283	61.514	0.87851
Skin	1.13	40.493	1.50125	48.4325	0.66327
Small Intestine	1.04	54.527	3.1335	66.004	1.9053
Spleen	1.05	52.546	2.2	63.1	1.0286
Stomach	1.05	62.239	2.1671	67.44	1.0046
Testis	1.04	57.629	2.1273	63.322	1.0285
Tooth	2.16	11.41	0.38459	13.136	0.09178

7.2 SPECIFIC ABSORPTION RATE (SAR)

The specific absorption rate (SAR) is the most common metric used to describe the energy absorption of EM waves by biological objects at RF. SAR is the rate of absorbed energy (power) in a unit body mass. It is defined in [61] as: "the time derivative of the incremental energy dW absorbed by an incremental mass dm contained in a volume element dV of a given density ρ" and is expressed in units of [W/kg] by

$$SAR = \frac{d}{dt}\left(\frac{dW}{dm}\right) = \frac{d}{dt}\left(\frac{dW}{\rho dV}\right). \qquad (7.7)$$

The SAR is related to the internal electric field E by

$$SAR = \frac{\sigma|E|^2}{\rho}, \qquad (7.8)$$

where E is the root mean square (rms) electric field strength in [V/m].

The SAR can also be used as a measure of the local heating rate [°C/s] which is given by

$$\frac{dT}{dt} = \frac{SAR}{c}, \qquad (7.9)$$

where c is the specific heat capacity of the tissue in [J/kg°C].

To protect the human body from the thermal damage of its biological tissues, international human safety committees and organizations have specified peak SAR values that should not be exceeded in any radiation application. The SAR is relevant in the frequency range of 100 kHz to 6 GHz [61]. Otherwise, limitations are set on the power density. In the following section, the most popular safety committees will be presented, followed by the safety criteria as given in the IEEE C95.1 standard [61], which is the most widely used standard.

7.3 SAFETY STANDARDS

Safety standards are regulations, recommendations and guidelines that are developed by specialized committees for the purpose of protecting human health from the adverse effects of EM radiation.

7.3.1 International Committees for Developing Safety Standards

Examples of international committees in charge of developing such standards are the Institute of Electrical and Electronics Engineers (IEEE) International Committee on Electromagnetic Safety (ICES), the National Council on Radiation Protection and Measurements (NCRP) in the United States and the International Radiation Protection Association International Commission on Non-Ionizing Radiation Protection (IRPA ICNIRP) [62].

These committees rely on the data collected from the literature that describes the interaction of RF radiation with the biological systems. Members of these committees evaluate the relevant published results on a continuous basis and develop the safety limits for the human exposure to RF fields. After approval, these limits are standardized in the form of international regulations and guidelines that are enforced in industry. The latest relevant IEEE standard is the IEEE C95.1 std., 1999 Edition [61], which has been approved by the American National Standards Institute (ANSI) for use as the American safety standard [62]. The IEEE/ANSI standard is used by many countries in developing their safety codes. Code 6, developed by Health Canada, is the Canadian safety standard [Safety Code 6, 1999]; and it adopts the IEEE C95.1 std. as the basis for its safety criteria.

Although the standards developed by all the different committees are based on the same biological background, still there are some slight differences between the exposure limits. This is attributed to differences in the arbitrarily chosen safety factors and is not based on biological conflicts. Safety factors are used mainly to compensate for any uncertainties in the data and to ensure that the limits are well below the danger thresholds.

7.3.2 Limits for Body Exposure to Radiation from Medical Implants: IEEE C95.1 std. ('99)

In the IEEE standard, exposure limits are developed for exposures in both controlled (workers) and uncontrolled (general public) environments. Radiation limits in controlled environments are higher than those in uncontrolled environments, since the general population is usually unaware of their exposure. According to the definitions given in the IEEE C95.1 std., body exposure to radiation from medical implanted devices is considered as a "partial-body"[3] exposure in an "uncontrolled environment"[4] [61].

Since the body tissues behave differently at different frequencies, the exposure limits are frequency-dependent. Figure 7.5 shows the limits versus frequency, in terms of the plane-wave free-space equivalent power density S [mW/cm^2], for the case of an uncontrolled environment [61, 63]. Power density S must be less than $f/1500$ in the frequency range of interest (300 MHz to 3 GHz).

At frequencies between 100 kHz and 6 GHz, exceeding the exposure limits is permitted under the condition that the SAR limits are not exceeded [61]. SAR limits are given in two forms. The first form is the whole-body average SAR, which is mainly used in the case when the exposed body is in the far zone of the radiating source. And the second form, which is used in the partial-body near-field exposure cases, is the local peak spatial SAR averaged over a given mass of tissue. In the IEEE C95.1 std., the spatial SAR is evaluated over 1 gram of tissue, where 1 gram of tissue is defined as a cubic centimeter volume of contiguous tissue [61]. Limits on SAR averaged over 1 gram of tissue are 20-25 times higher than the whole-body average SAR [64]. In the case of partial-body exposure in an uncontrolled environment, whole-body average SAR must be below 0.08 W/kg and the peak spatial average SAR must be less than 1.6 W/kg [61].

[3] *"Partial-body exposure: Exposure that results when RF fields are substantially nonuniform over the body. Fields that are nonuniform over volumes comparable to the human body may occur due to highly directional sources, standing-waves, re-radiating sources, or in the near field region of a radiating structure."*

[4] *"Uncontrolled environment: Locations where there is the exposure of individuals who have no knowledge or control of their exposure."*

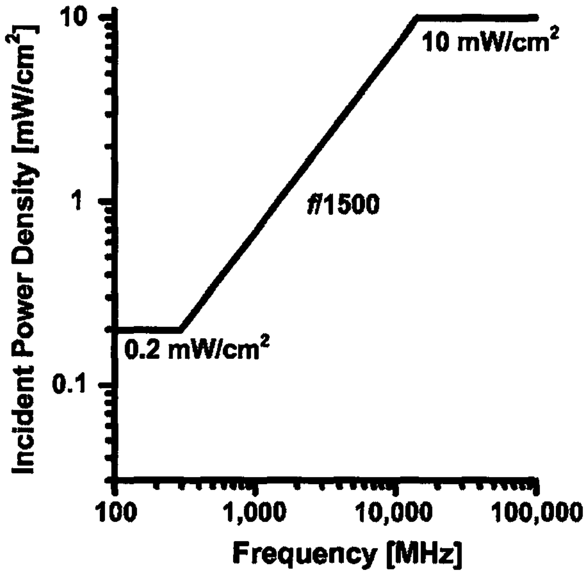

Fig. 7. 5. Maximum permissible exposure expressed in terms of the power density in an uncontrolled environment [61].

7.4 EM DOSIMETRY

EM dosimetry techniques are used to evaluate the conformity of the radiation doses of wireless devices with the safety limits. In EM dosimetry, the human exposure to RF fields is quantified by determining the SAR distribution in the body tissues. The assessment of the human exposure can be evaluated experimentally, numerically or preferably both. Dosimetric near field measurement equipments and computational tools are widely available to assess the SAR distributions in the vicinity of wireless devices [65]. These techniques are also applicable to the exposure assessment of in-body radiation.

Figure 7.6 and 7.7 show experimental set-ups that can be used for SAR measurements [66, 67]. These are very complicated and bulky, making SAR measurements very expensive and not always possible. In these measurements, the electric field distribution in the liquid that mimics the human body (phantom) is measured using E-field probes that are controlled and positioned using a robotic arm. Knowing the field distribution in the exposed body tissues, the SAR can be calculated and compliance with the safety standards ensured. Techniques for modeling the human body for experimental purposes are presented in Subsection 7.5.1.

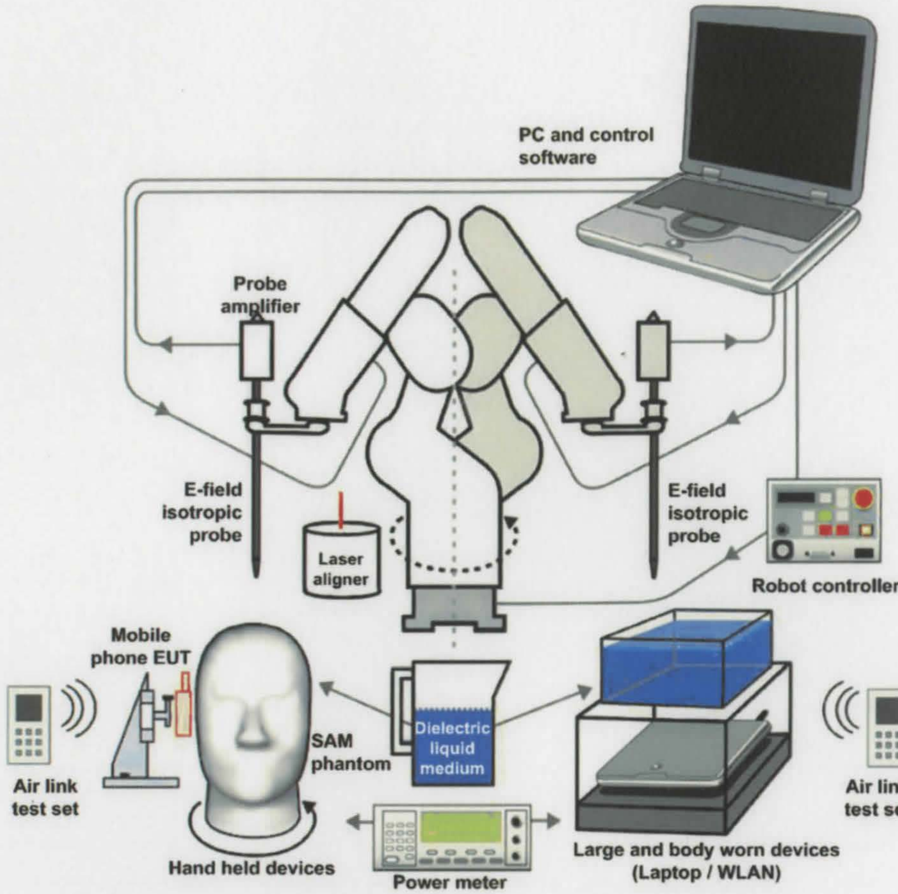

Fig. 7. 6. Experimental set-up for SAR measurements [66].

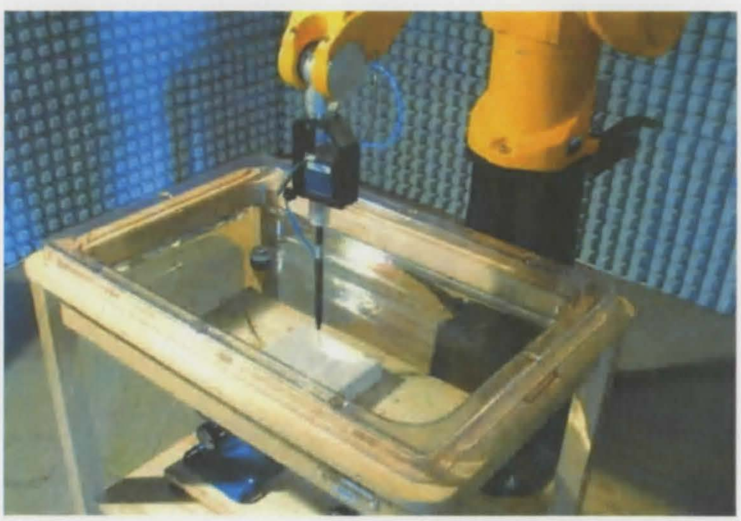

Fig. 7. 7. SAR measurement equipment used at Ericsson [67].

The other way to assess the in-body radiation is using numerical simulations. Many numerical techniques can be used in solving the in-body radiation problem. In this thesis, we have used a method of moments (MoM) antenna solver to develop the SAR distribution. Another technique is the FDTD (Finite Difference Time Domain) method. To be able to assess the SAR distribution numerically, the problem space (human body) has to be numerically modeled. Once a whole-body model is available, it can be included in the numerical simulator to solve the interaction problem. Issues related to developing numerical body models (numerical phantoms) are presented in Subsection 7.5.2.

7.5 Modeling of the Human Body for EM Dosimetry

Phantoms are defined as "models that mimic the response of a subject to an external agent under investigation" [68]. In the case of EM dosimetry, a phantom is a model (experimental or numerical) that mimics the response of the human body to RF radiation. To be able to develop these phantoms, the exposed body tissues should be identified and their electrical properties should be characterized at the frequency range of interest. The phantom complexity determines the accuracy of the assessment. Depending on the exposed body part, whole body or partial body models are used. Phantoms are 3-dimensional and their shapes can be spherical, cylindrical or anatomically realistic showing the details. The phantom can be homogeneous, layered or heterogeneous. A homogeneous phantom is a coarse representation of the real human body, while a heterogeneous phantom simulates the human body in greater anatomical detail, which allows for a more realistic assessment of SAR, providing a more conservative estimate.

7.5.1 Experimental Phantoms

Experimental phantoms are spherical, cylindrical or detailed shell containers with a body simulating liquid. Liquids are preferred in this case to allow for the movement of the E-field measuring probes. The dimensions of these containers and the recipes for mixing body simulating liquids are given in international standards [69, 72]. For frequencies below 1 GHz, the tissue simulating liquid is prepared from nontoxic substances – sucrose (sugar), deionized water, salt (NaCl) and cellulose, while at higher frequencies; the recipe involves polyhydric alcohol plus the deionized water [55]. For verification, electric properties of the body simulating liquid can be measured after preparation using a technique called the coaxial probe method [70, 71]. Figure 7.8 shows the specific container dimensions as given in the European standard for SAR assessment of ultra low-power active medical implants [72].

To obtain the radiation characteristics of the loop antennas investigated in this work, two solutions were prepared to model the human body at 405 MHz and at 2.4 GHz, respectively. The recipes are given in Appendix A [69]. Expiration of these liquids is mainly caused by water evaporation [55] and if the container is tightly closed, the electrical properties of the solution will not change with time and the liquids will be valid for a longer time. A container similar to the one prescribed in [72] (see also Fig. 7.8) has been used during the measurements.

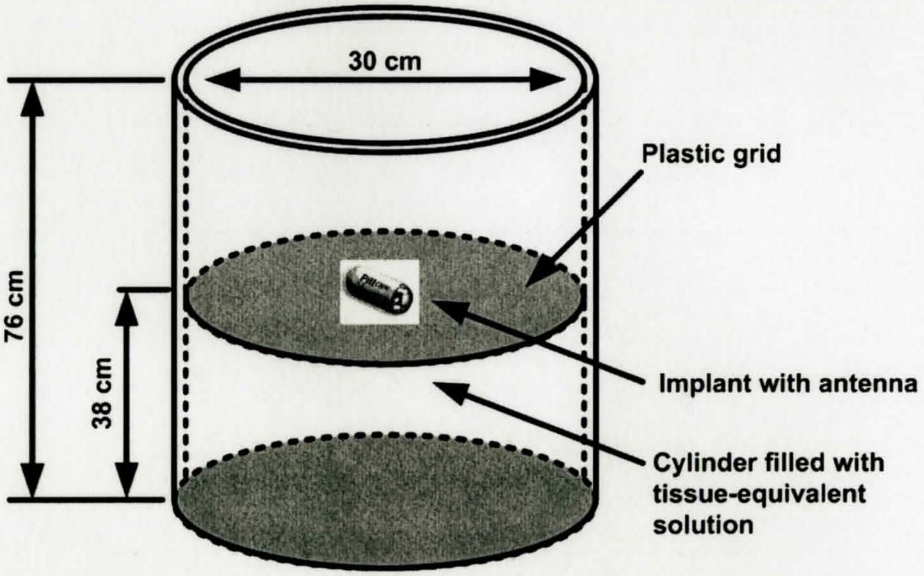

Fig. 7. 8. Simulated human body for experimental in-body exposure assessment [72].

7.5.2 Numerical Phantoms

Numerical phantoms are classified according to their geometrical. In [73], it was concluded that great geometrical detail is not necessary and simplified geometries can be used to model the shape of the human body. Numerical phantoms are also classified according to their anatomical details. A phantom can be homogeneous, tissue-layered or detailed tissue-segmented. Figure 7.9 shows a four-layer spherical model of the human head containing the most important tissue types.

The tissue-segmented model is the most accurate. Tissue-segmented phantoms are constructed using medical imaging data and the electrical data of the various body tissues. A number of transverse magnetic resonance imaging (MRI) slices of the body of a male, female or a child are needed. These can be derived from the Visible Male (VM) and Visible Female (VF) data available from the U.S. National Library of Medicine under the Visual Human Project (VHP) [74]. Each of these medical images is segmented into the various biological tissues that the body part is constructed of (Fig. 7.10). These reconstructed slices are then used to generate a three-dimensional numerical phantom that contains a number of voxels (volume pixels). Figure 7.11 shows a cross-section of a tissue-segmented numerical phantom [75]. Each voxel is assigned a tag that identifies its tissue type. This model is then linked to a database of the frequency-dependent electrical properties of the various body tissues.

The phantom accuracy depends strongly on the voxel size. This in turn depends on the number of transverse MRI slices used, the image resolution and the tissue segmentation level. The smaller the voxel size, the more accurate the model and the more anatomical details it mimics. On the other hand, accurate phantoms require huge computational resources and long simulation times. Since the EM wave is mainly absorbed by the tissues in the close vicinity of the radiating source, these tissues are more important and it is reasonable, therefore, to use a model that is semi-segmented, where the body part closest to the radiating source is modeled in greater detail and further parts are tissue-layered. In [13], it was proven that too much detail is not necessary and that the human exposure can be accurately evaluated using semi-segmented phantoms.

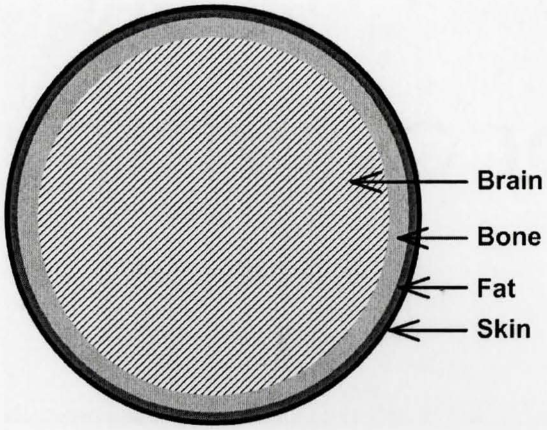

Fig. 7. 9. Four-layer spherical model of the human head.

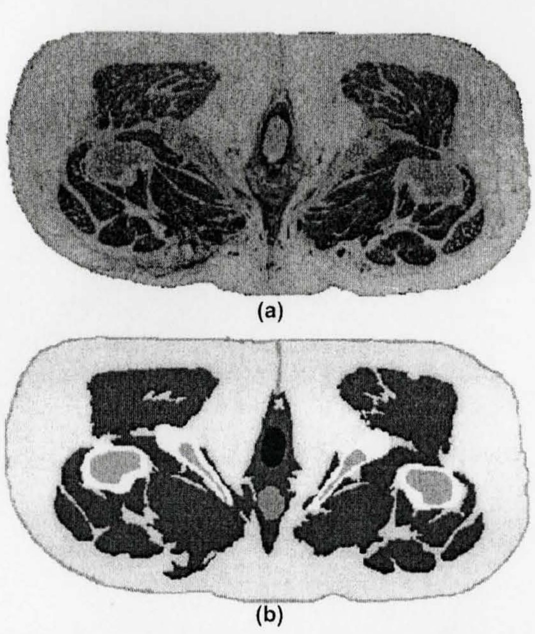

Fig. 7. 10. Tissue-segmentation of a transverse MRI scan of a female body: (a) MRI image and (b) tissue-segmented digital image [13].

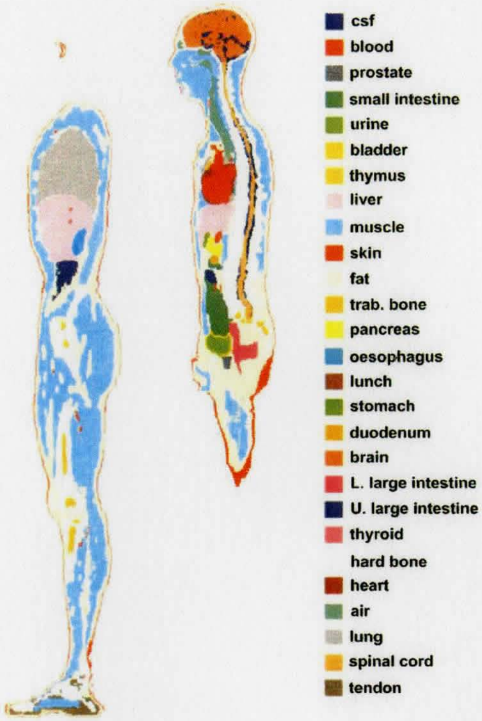

Fig. 7. 11. Tissue-segmented detailed numerical phantom [75].

7.6 SUMMARY

In this chapter, we have presented the various aspects of the in-body radiation problem. First, the human body was characterized as a radiation environment in terms of its electrical behavior. Then, the concept of SAR for RF exposure assessment was introduced. Afterwards, the experimental and numerical dosimetric techniques were discussed in detail. Finally, the chapter was concluded by a discussion on experimental and numerical phantoms used in EM dosimetry.

CHAPTER 8

Radiation Characteristics of In-Body Loop Antennas

Antennas are used in RF transceivers to transform the RF signal into a radiated wave and vice versa. The electrical size of the antenna is a major parameter that determines its radiation efficiency. For efficient radiation, the antenna size should be at least one half of the wavelength in the medium where the antenna operates. Small antennas in free space are consequently inefficient. However, when immersed in a dissipative medium such as the human body, the physically small antenna becomes an efficient radiator. In this dissipative medium, the wavelength decreases ($\lambda = c/(\sqrt{\varepsilon_r} f)$) and the antenna size becomes comparable to it. At 405 MHz, the wavelength in free space is about 74 cm, while in the human body it is only 9.8 cm (assuming a relative permittivity of 58).

As part of this research, we have performed an investigation on the suitability of loop antennas for in-body operation. Radiation characteristics of implanted loop antennas were evaluated in terms of their radiation resistance, radiation efficiency and frequency bandwidth of their impedance. Also, the SAR distribution was studied using numerical EM simulations to ensure compliance with the safety standards. To experimentally confirm the suitability of loop antennas for biomedical implants, a prototype wire loop antenna was fabricated and its return loss was measured. The measurement data was then used to estimate its impedance.

Details of the radiation characteristics of in-body loop antennas are presented in this chapter. Section 8.1 briefly highlights the performance specifications of antennas for implanted transceivers. Section 8.2 presents the analytical evaluation of the performance of the implanted loop. Section 8.3 presents the numerical results of the SAR distribution in the body tissues surrounding the loop, and Section 8.4 presents the experimental results. Finally, the summary of the chapter is given in Section 8.5.

8.1 Antennas for Implanted Transceivers

As discussed in Chapter 7, human tissues are very dissipative at RF. Given the limited supply power of implanted wireless systems and to compensate for the losses occurring in human tissues, a highly efficient antenna is needed. Antennas for implanted biomedical transceivers should in addition have the following specifications: (1) radiation levels complying with the safety standards, (2) small physical size (~ 28 mm x 10 mm in our case), and (3) reasonable bandwidth for reliable transmission.

For implanted antennas, especially those radiating deep from the inside of the human body, the radiation pattern and far field are insignificant, since the wave will be absorbed by the body tissues in the near zone of the antenna ($kr \ll 1$, where r is the distance from the source and k is the complex propagation constant given in (7.3)). In the design of these antennas, the near field and SAR evaluations are of utmost importance.

Several types of antennas are used in biomedical implants. For applications where the implant is placed close to the surface of the human body such as in pacemakers, dipoles [77] and planar antennas are used [71, 73, 78, 79]. Printed and wire loop antennas have also been effectively used in biotelemetry implants [13, 80, 81].

In this thesis, we present an investigation of the suitability of wire loop antennas for the use in the implanted imaging pill. Analytical formulas, numerical simulations and an experimental set-up were used to develop the radiation characteristics of the implanted loop antennas. The models used for the human body are simple, homogeneous models with electrical properties averaged over a number of biological tissues. The model used in the analytical evaluation assumes an infinite medium, while the ones used in the numerical and experimental assessments are finite cylindrical models. Although homogeneous models are coarse representations of the human body, they are good enough for the early investigations of the radiation characteristics of a candidate antenna.

8.2 Analytical Evaluation of the Radiation Characteristics of In-Body Loop Antenna

The radiation performance of a loop antenna is a function of a number of parameters – the frequency of operation, the number of turns, the antenna dimensions, the wire conductivity, the electrical properties of the medium and the amount of feed power.

Figure 8.1 shows a multiturn loop antenna showing its dimensions. In this figure, a is the wire radius, b the loop radius and c is half the spacing between the turns. The total length of the loop is given by $N(2\pi b)$ for an N-turn loop.

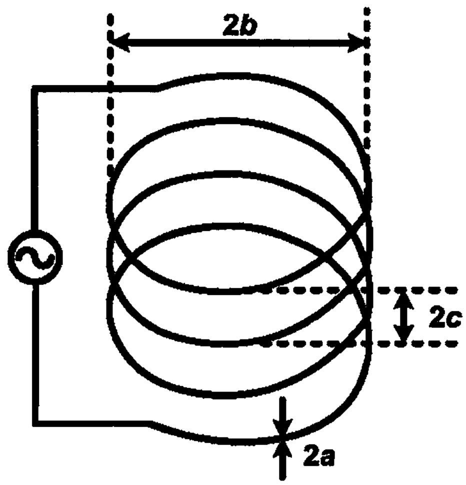

Fig. 8. 1. Multiturn loop antenna.

The loop performance is estimated in this section using analytical formulas from the literature, which were implemented in a MATLAB code. The characteristics of the loop antennas were evaluated for a single-turn loop with a radius of 3.5 mm, a wire radius of 0.2 mm and a turn spacing of 4 mm. The analytical formulas used here were originally developed for loop antennas of small to moderate electrical sizes [76]. An antenna is considered to be of small size in the medium if $\beta b \leq 0.2$ [76], where β is the phase constant in the medium given by equation (7.5). At 405 MHz, a loop with the dimensions mentioned above is of moderate size (βb equals 0.25), and hence, these formulas are still applicable. However, at 2.4 GHz, the loop antenna becomes electrically large (βb equals 1.25) and these formulas can be no longer used. Table 8.1 gives the geometrical parameters and the conductivity of the loop wire used in the antenna analysis.

Table 8. 1. Antenna parameters used in the evaluation of the in-body loop radiation performance.

Parameter	Value
a	0.2 mm
b	3.5 mm
c	2 mm
σ_c	5.88 x 10^7 S/m (Copper)

8.2.1 Radiation Impedance

To estimate the radiation impedance of the loop antenna, we used the analytical formulation of the input admittance Y given in [76][5].

$$Y = \frac{\beta^2 b}{\omega\mu_0}\left\{(\pi\beta b + 8\alpha/\beta)/6\left[A_1(b/a)\right]^2 + 4(\alpha/\beta)S(b/a)\right\}$$
$$-\frac{j}{\omega\mu_0 b}\left(\begin{array}{l}\left\{1-\frac{2}{3}(\beta b)^2\left[1-(\alpha/\beta)^2\right]/A_1(b/a)\right\}/A_1(b/a)\\ -2(\beta b)^2\left[1-(\alpha/\beta)^2\right]S(b/a)\end{array}\right), \tag{8.1}$$

where $\mu_0 = 4\pi 10^{-7}$ H/m is the permeability of free space and α and β are the attenuation constant and the phase constant, respectively. They are calculated using (7.4) and (7.5) using the electrical data of the medium. Table 8.2 gives the electrical data used in modeling the human body [56]. The parameters $S(b/a)$ and $A_n(b/a)$ are calculated as follows

$$S(b/a) = \sum_{n=1}^{20} 1/\left[n^2 A_n(b/a)\right], \tag{8.2}$$

$$A_n(b/a) = \ln\left(\frac{8b}{a}\right) - 2\sum_{m=0}^{n-1}\frac{1}{2m+1} + \frac{1}{2}\left(\frac{na}{b}\right)^2\left[\ln\left(\frac{2b}{na}\right) + \frac{1}{2} - \gamma\right], \tag{8.3}$$

where γ is the Euler's constant and is equal to 0.5772.

---

[5] *To be able to reproduce the curves of the input admittance Y shown in [1], an adjustment factor of 0.5 was added to the equations in the implemented MATLAB code.*

Table 8. 2. Medium parameters at 405 MHz used in the analytical and SAR evaluation of the loop (average of the parameters of several body tissues [56]).

Parameter	Value
σ	0.944 S/m
ε_r	54
$\tan\delta$	0.722

This formulation of the loop input admittance was developed in [76] based on some assumptions. First, it was developed for a single-turn loop antenna with small electrical dimensions ($\beta b \leq 0.2$). Second, the first 20 terms of the Fourier series expansion of the current in the loop were accounted for in the derivation [76]. And finally, the formulation assumes the antenna to be radiating in a lossy medium of infinite dimensions. This latter assumption is valid for a loop antenna radiating deep from within the human body, as in the case of the WCE pill, where the radiation will be mostly absorbed within the biological tissues.

The radiation resistance and susceptance of the single-turn loop defined in Table 8.1 are shown in Fig. 8.2. The loop is expected to have a radiation resistance of about 30 Ω and an inductive susceptance of about 73 Ω. With this radiation resistance, the loop antenna immersed in the human body is shown to be a good radiating source. For a multiturn loop antenna, the radiation impedance will increase even further, approximately in proportion to N^2. As is the case for electrically small loop antennas, the antenna has an inductive reactance. However, as will be seen later in this chapter, larger loops can become capacitive. The reactive part of the input impedance can be canceled using a passive network with tuning elements.

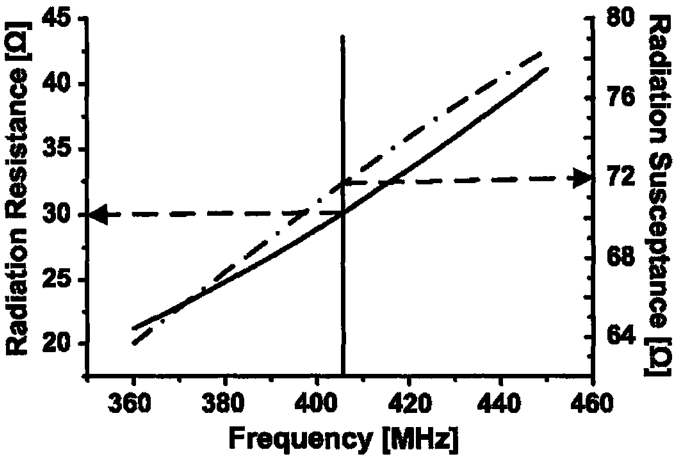

Fig. 8. 2. Radiation impedance of the antenna described in Table 8.1.

8.2.2 Radiation Efficiency

To be able to calculate the radiation efficiency, the losses in the loop antenna have to be determined. Ohmic losses in a multiturn loop antenna with closely spaced turns are due to the skin effect and the proximity effect. The skin effect is a high-frequency phenomenon that occurs due to the finite conductivity of the loop wire resulting in a current that is confined to a small layer at the surface. The proximity effect is due to the proximity of two or more conductors that are carrying current. This effect further reduces the area of current flow in the conductors, contributing to the ohmic losses. Assuming an antenna with a radiation impedance Z_{rad}, then its radiation efficiency is given by

$$\eta_{\mathrm{rad}} = \frac{\operatorname{Re} Z_{rad}}{\operatorname{Re} Z_{rad} + R_{ohmic}}. \tag{8.4}$$

In our case, Z_{rad} is the radiation impedance of the loop antenna calculated using the expressions in Section 8.2.1. In (8.4), R_{ohmic} is the resistive loss in the loop due to the proximity and the skin effects. For a N-turn loop antenna, R_{ohmic} is given by [82]

$$R_{ohmic} = N\frac{b}{a}R_s\left(\frac{R_p}{R_o}+1\right). \tag{8.5}$$

Here, R_s is the surface resistance of the conductor, and R_o is the ohmic skin effect resistance of the conductor per unit length, which are given by [82]

$$R_s = \sqrt{\frac{\omega\mu_0}{2\sigma_c}}, \tag{8.6}$$

$$R_o = \frac{NR_s}{2\pi a} \; [\Omega/\mathrm{m}]. \tag{8.7}$$

σ_c is the conductivity of the metal wire used to build the loop and R_p is the ohmic resistance per unit length due to the proximity effect. The normalized proximity effect ohmic loss resistance per unit length, R_p/R_o, can be interpolated for an antenna with up to 8 turns and with a c/a ratio of up to 4 using Table 8.3 [83].

Table 8. 3. Normalized ohmic resistance per unit length due to the proximity effect [83].

c/a	2 turns	3 turns	4 turns	5 turns	6 turns	7 turns	8 turns
1	0.333	0	0	0	0	0	0
1.05	0.316	0.743	1.231	0	0	0	0
1.10	0.299	0.643	0.996	1.347	1.689	2.02	2.34
1.15	0.284	0.58	0.868	1.142	1.4	1.643	1.872
1.20	0.268	0.531	0.777	1.002	1.21	1.401	1.577
1.25	0.254	0.491	0.704	0.896	1.068	1.224	1.365
1.30	0.24	0.455	0.644	0.809	0.956	1.086	1.203
1.40	0.214	0.395	0.546	0.674	0.784	0.88	0.965
1.50	0.191	0.346	0.47	0.572	0.658	0.732	0.796
1.60	0.173	0.305	0.408	0.492	0.561	0.62	0.67
1.70	0.155	0.27	0.358	0.428	0.485	0.532	0.573
1.80	0.141	0.241	0.316	0.375	0.423	0.462	0.495
1.90	0.128	0.216	0.281	0.332	0.372	0.405	0.433
2.00	0.116	0.195	0.252	0.295	0.33	0.358	0.382
2.20	0.098	0.161	0.205	0.239	0.265	0.286	0.304
2.40	0.082	0.135	0.17	0.197	0.217	0.234	0.247
2.50	0.077	0.124	0.156	0.18	0.198	0.213	0.225
2.60	0.071	0.114	0.144	0.165	0.182	0.195	0.206
2.80	0.061	0.098	0.123	0.141	0.154	0.165	0.174
3.00	0.054	0.085	0.106	0.121	0.133	0.142	0.15
3.50	0.04	0.062	0.077	0.087	0.095	0.101	0.106
4.00	0.031	0.048	0.058	0.066	0.072	0.076	0.08

For the loop described in Table 8.1, losses are only due to the skin effect (R_o equals 4.15 Ω), resulting in a radiation efficiency of 87.84%. This implies that loop antennas show high radiation efficiencies when operating in a body-like environment.

8.2.3 Transmission Bandwidth

As can be seen from Fig. 8.2, the electrically small loop analyzed here is inductive. To tune out the reactive part of the loop input impedance, a series tuning capacitor is needed. The value of this capacitor can be calculated from

$$C_{tun} = \frac{1}{\omega_0^2 L}, \tag{8.8}$$

where L is calculated from the reactive part of the input impedance as

$$L = X/\omega_0. \tag{8.9}$$

The loop can be represented by the equivalent circuit shown in Fig. 8.3. The figure shows the antenna – modeled by the radiation impedance ($Z_{rad} = R_{rad} + jX$), the loss resistance R_{ohmic} and a lumped tuning capacitor C_{tun}. Thus, for the tuned antenna, the total input impedance Z_{in} can be written as

$$Z_{in}(\omega) = R_{rad} + j\omega L + R_{ohmic} + \frac{1}{j\omega C_{tun}}. \tag{8.10}$$

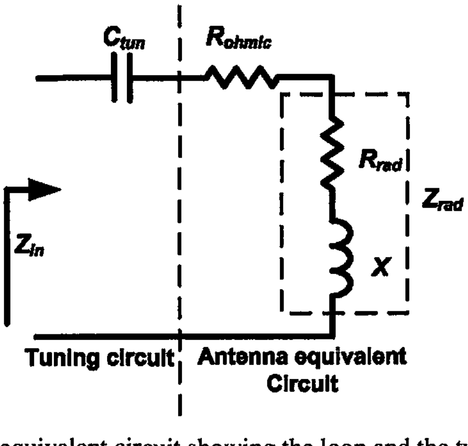

Fig. 8. 3. Loop equivalent circuit showing the loop and the tuning capacitor.

Assuming a feeding source with input impedance Z_0, the reflection coefficient Γ is given by

$$\Gamma(\omega) = \frac{Z_{in}(\omega) - Z_0}{Z_{in}(\omega) + Z_0}. \tag{8.11}$$

The voltage standing wave ratio (VSWR) can then be expressed by

$$\mathrm{VSWR}(\omega)=\frac{1+|\Gamma(\omega)|}{1-|\Gamma(\omega)|}. \tag{8.12}$$

For a tuned loop, the VSWR equals one at the operating frequency ω_0. Now, the matched VSWR bandwidth is defined as the band of frequencies around ω_0, for which the VSWR is equal to or less than a given desired value R. An expression for the VSWR bandwidth of a tuned antenna as a function of its input impedance is given in [84]. For a maximum allowable VSWR R, the VSWR bandwidth in hertz can be estimated from

$$BW=\frac{1}{2\pi}\cdot\frac{2(R-1)\cdot\mathrm{Re}\,Z_{in}(\omega_0)}{\sqrt{R}\cdot|Z'_{in}(\omega_0)|}. \tag{8.13}$$

In this equation, Z_{in}' is the derivative of the input impedance of the tuned antenna with respect to the angular frequency ω.

Next, we are going to determine the angular frequency dependence of the input impedance of the loop to calculate the VSWR bandwidth. The total input impedance including the loss resistance and the tuning capacitor can be written as

$$Z_{in}=Z_{rad}+R_{ohmic}+\frac{1}{j\omega C_{tun}}. \tag{8.14}$$

Now, taking the derivative of (8.14) with respect to ω, we get

$$\frac{\partial Z_{in}}{\partial\omega}=\frac{\partial Z_{rad}}{\partial\omega}+\frac{\partial R_{ohmic}}{\partial\omega}+\frac{j}{\omega^2 C_{tun}}. \tag{8.15}$$

The derivative of Z_{rad} is given by

$$\frac{\partial Z_{rad}}{\partial\omega}=\frac{\partial}{\partial\omega}\left(N^2 Z\right)=\frac{\partial}{\partial\omega}\left(\frac{N^2}{Y}\right)=-\frac{N^2}{Y^2}\frac{\partial Y}{\partial\omega}. \tag{8.16}$$

So, (8.15) becomes

$$\frac{\partial Z_{in}}{\partial\omega}=-\frac{N^2}{Y^2}\frac{\partial Y}{\partial\omega}+\frac{\partial R_{ohmic}}{\partial\omega}+\frac{j}{\omega^2 C_{tun}}. \tag{8.17}$$

Now, the derivative of the input admittance Y can be written as

$$\frac{\partial Y}{\partial \omega} = -\frac{1}{\omega^2 \mu_0}\left\{\beta^2 b\left[\frac{\pi b + 8\alpha/\beta}{6\left[\ln(8b/a)-2\right]} + 4\left(\frac{\alpha}{\beta}\right)S(b/a)\right] - \frac{j}{b\left[\ln(8b/a)-2\right]}\right\}$$
$$+\frac{1}{\omega\mu_0}\left\{\begin{array}{l} 2\beta b\dfrac{\partial\beta}{\partial\omega}\left[\dfrac{\pi b + 8\alpha/\beta}{6\left[\ln(8b/a)-2\right]} + 4\left(\dfrac{\alpha}{\beta}\right)S(b/a)\right] \\ +\beta^2 b\left[\begin{array}{l}\dfrac{8\left[(-\alpha/\beta^2)\partial\beta/\partial\omega + (1/\beta)\partial\alpha/\partial\omega\right]}{6\left[\ln(8b/a)-2\right]^2} \\ +4S(b/a)\left[(-\alpha/\beta^2)\partial\beta/\partial\omega + (1/\beta)\partial\alpha/\partial\omega\right]\end{array}\right]\end{array}\right\}. \tag{8.18}$$

To evaluate $Y'(\omega)$, derivatives of the phase constant β, the attenuation constant α and the ohmic loss resistance R_{ohmic} need to be evaluated. Simply, $\partial\alpha/\partial\omega$ and $\partial\beta/\partial\omega$ are the real and the imaginary parts of the derivative of the complex propagation constant in (7.3)

$$\frac{\partial k}{\partial \omega} = j\sqrt{\mu_0\varepsilon'\left(1 - j\tan\delta - j\frac{\sigma}{\omega\varepsilon'}\right)} - \frac{\mu_0\sigma}{2\omega}\frac{1}{\sqrt{\mu_0\varepsilon'\left(1 - j\tan\delta - j\dfrac{\sigma}{\omega\varepsilon'}\right)}}, \tag{8.19}$$

$$\frac{\partial k}{\partial \omega} = \frac{\partial \alpha}{\partial \omega} + j\frac{\partial \beta}{\partial \omega}. \tag{8.20}$$

Finally, the derivative of R_{ohmic} is given by

$$\frac{\partial R_{ohmic}}{\partial \omega} = N\left(\frac{b}{a}\right)\left(\frac{R_p}{R_o}+1\right)\frac{\partial R_s}{\partial \omega} = N\left(\frac{b}{a}\right)\left(\frac{R_p}{R_o}+1\right)\frac{R_s}{2\omega}. \tag{8.21}$$

In calculating the above derivatives, variations in the electric parameters of the medium within the band of operation were neglected.

Figure 8.4 shows the VSWR of the antenna referenced to its real input impedance, which was calculated in Section 8.2.1 to be 30 Ω, hence Z_0 is assumed to be 30 Ω, as a function of frequency and centered at 405 MHz. Aiming for a VSWR≤1.3, the transmitting bandwidth of the antenna given in Table 8.1 is about 40 MHz assuming a tuning capacitor of 5.5 pF. This wide band of operation is due to the large radiation resistance in the medium, where the BW is inversely proportional to the antenna quality factor Q (BW=1/Q), which is given by

$$Q = X/(X + R_{ohmic}). \tag{8.22}$$

As can be concluded from the previous analysis, electrically small loop antennas operating at RF and radiating in a dissipative medium, have reasonable transmission bandwidths, which is desirable to allow for reliable communication from the implant.

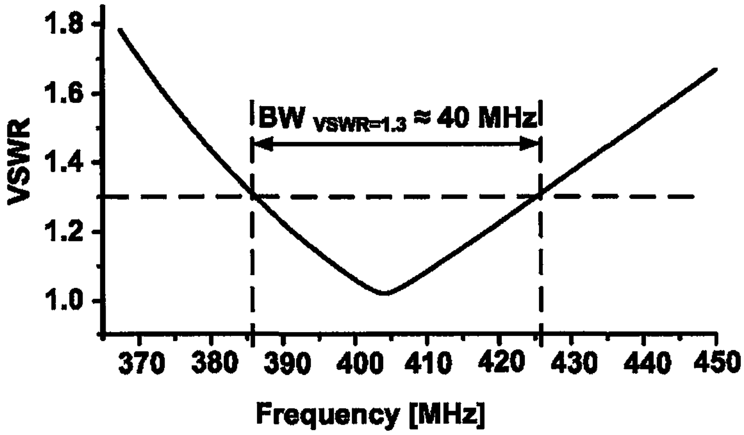

Fig. 8. 4. The VSWR of the loop antenna in Table 8.1 assuming it is tuned and matched to its real input impedance.

8.3 Numerical SAR Assessment of In-Body Loop Antennas

In this section, full-wave EM simulations were used to characterize the conformity of small loop antennas with the safety limits for 5 mW power feed. As stated in Chapter 7, the IEEE C95.1 standard specifies the peak local SAR averaged over 1 gram of tissue (1 cm^3) to be lower than 1.6 W/kg [61]. The local SAR distribution was estimated using FEKO, which is a method of moments (MoM) antenna solver [85]. The loop used in this section is a 7-turn loop antenna and has the geometry parameters described in Table 8.1.

In constructing the problem space, all discretization rules specified in FEKO's user manual were followed. The antenna was segmented into a number of copper segments as shown in Fig. 8.5. The human body was modeled as a homogeneous cylinder of 4 centimeters height and 2 centimeters radius constructed of dielectric volume cubes, or cuboids. Figure 8.6 shows a screen capture showing the simulation environment used in FEKO.

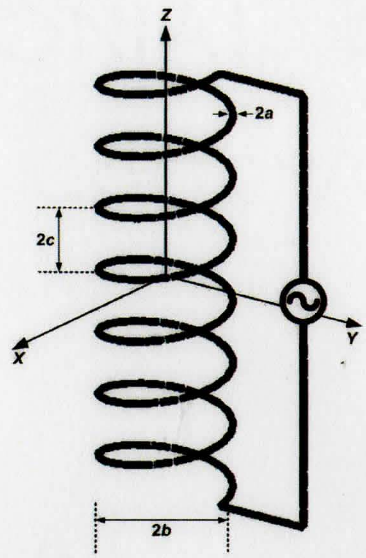

Fig. 8. 5. Segmented wire loop antenna as implemented in the simulations.

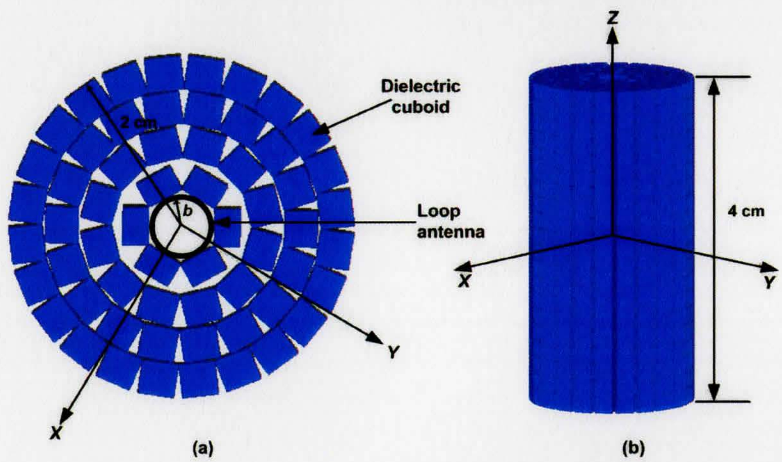

Fig. 8. 6. Simulation environment showing the dielectric cylinder (a) top view and (b) side view.

FEKO calculates the SAR in each of the dielectric cuboids[6] using the E-field data in the near field zone of the antenna using equation (7.8). Figure 8.7 shows the computed SAR distribution versus distance from the center of the loop for an input power of 5 mW. Values of the SAR in the dielectric cuboids were found in the output file generated by FEKO and were interpolated elsewhere. The figure clearly shows that the SAR values are well below the safety limit of 1.6 W/kg that is specified in the IEEE C95.1 standard. Also

---

[6] *FEKO evaluates the absorption rate averaged over the volume of one cuboid, not over 1 cm^3 as specified in the safety standard [15].*

to be noted from the figure, the EM fields are absorbed by the tissues surrounding the antenna; hence the SAR values are maximum at the periphery of the loop. The peak at about 8 mm distance from the center of the loop is due to the reflections at the dielectric/free space interface of the finite cylindrical model used in the simulations.

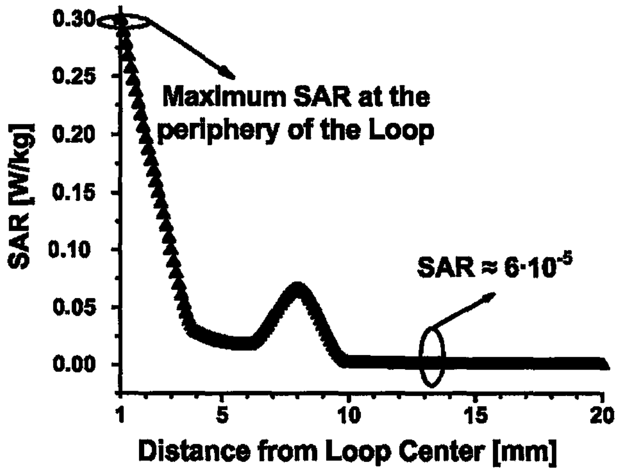

Fig. 8. 7. SAR distribution in the proximity of the loop showing that the values are well below the safety threshold (variation in one direction only was assumed).

The minimum discretization dimensions of the wire segments and the cuboids are given in terms of the wavelength in the medium, making the simulation time and the required memory resources frequency-dependent. The above results were produced for the loop antenna at 405 MHz. The simulations took about five hours and about four gigabyte of memory. At 2.4 GHz, however, the numerical simulations became so computational-resource intensive that it could not be performed on an ordinary computer. Thus, to develop the radiation performance of the loop at 2.4 GHz, only measurements were used.

8.4 Experimental Verification of the Suitability of Loop Antennas for Biomedical Implants

To experimentally develop the input impedance characteristics of implanted loop antennas, we have built a couple of loop antennas. The antennas were built using thin copper wires wound around two custom-made pill-like glass rods (Fig. 8.8). The antenna leads were then soldered to RF adaptors to be able to connect it to the RF cables and then to the measuring equipment. The multiturn antennas were designed to have the dimensions given in Table 8.1, resulting in an antenna size that complies with the physical constraint (24 mm x 7 mm for the 7-turn loop).

A loop antenna can be considered a 1-port differential device. To experimentally develop the radiation characteristics of loop antennas, they should be fed differentially. Differential feed (two feed currents with 180 degrees phase difference) can be provided to the antenna either using a 4-port vector network analyzer (VNA), or a 2-port VNA and a balun. However, to derive the input impedance, the way the antenna is fed is not significant, and practically, a traditional 2-port VNA with no balun can be used. There are two ways to do these measurements, either using one port of the VNA (1-port measurements) or using the two ports of the VNA (2-ports measurements). In the 1-port measurements, one lead of the antenna is connected to the VNA and the other to ground. In the 2-port measurements, each antenna lead is connected to one of the VNA ports, assuming a differential feed with both currents in the same direction rather than two currents of opposite directions.

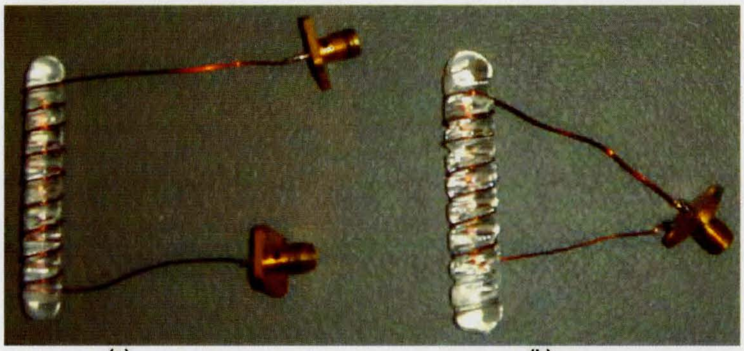

(a) (b)

Fig. 8. 8. Fabricated loop antennas for 2-port (a) and 1-port (b) VNA measurements.

We measured the antennas at 405 MHz and at 2.4 GHz using an Agilent-8722ES *S*-parameter network analyzer and two RF cables. One-port and two-port calibrations were performed on the VNA and the RF cables using a short-open-load (SOL) calibration kit.

To realize a radiation environment similar to the human abdomen, the antennas were dipped in a cylindrical plastic container filled with a homogeneous liquid with body-similar dielectric properties at the respective frequency. The two body-equivalent chemical solutions were prepared in-house in collaboration with the Chemical

Engineering Department at McMaster University. The recipes used to mix these solutions at 2.4 GHz and 405 MHz are given in Appendix A [69]. The complete measurement set-up including the VNA, the body-equivalent solution, the RF cables and the antenna is shown in Fig. 8.9.

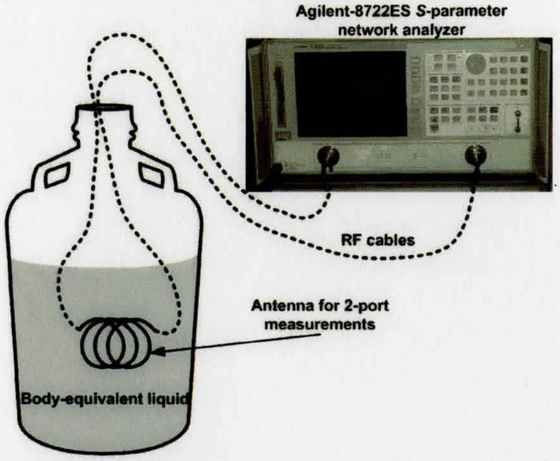

Fig. 8. 9. Measurement set-up used to evaluate the input impedance of in-body loop antennas.

Figures 8.10 and 8.11 show the return loss and the input impedance of the antenna using the 1-port measurement technique. Figures 8.10 (a) and 8.11 (a) show the return losses at 405 MHz and at 2.4 GHz, respectively, comparing both the antenna dipped in the medium and in free space. It is seen that the input impedance of the loop antenna in free space is slightly better at 2.4 GHz than at 405 MHz, since at the higher frequency the same antenna becomes electrically larger. The network transformation formulas given in Appendix B were used to transform the *S*-parameter data to *Z*-parameters. Figures 8.10 (b) and 8.11 (b) show the input impedance of the antenna at both frequencies. As can be seen from the figures, the antenna dipped in the liquid exhibits a good match to 50 Ω impedance, showing a reasonable radiation resistance at both frequencies. As shown in Fig. 8.10 (b) and 8.11 (b), the input reactance of the loop antenna of the dimensions given in Table 8.1 operating in a lossy medium is capacitive almost over the entire frequency range. Thus, a tuning inductor is needed for the loop tuning. The cusp in the 2.4-GHz return loss of the antenna in free space was not expected to exist. This could be due to the fact that the free-space measurements presented here were not preformed in an anechoic chamber as they are normally done. They were rather performed in an equipped and furnished laboratory, which could cause the antenna to resonate as shown.

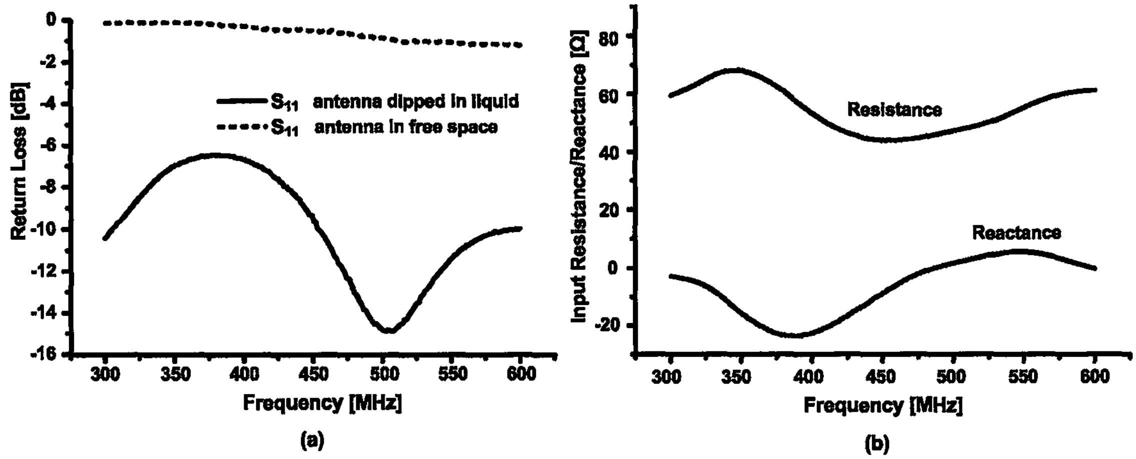

Fig. 8. 10. One-port measurements at 405 MHz: (a) return loss and (b) input impedance.

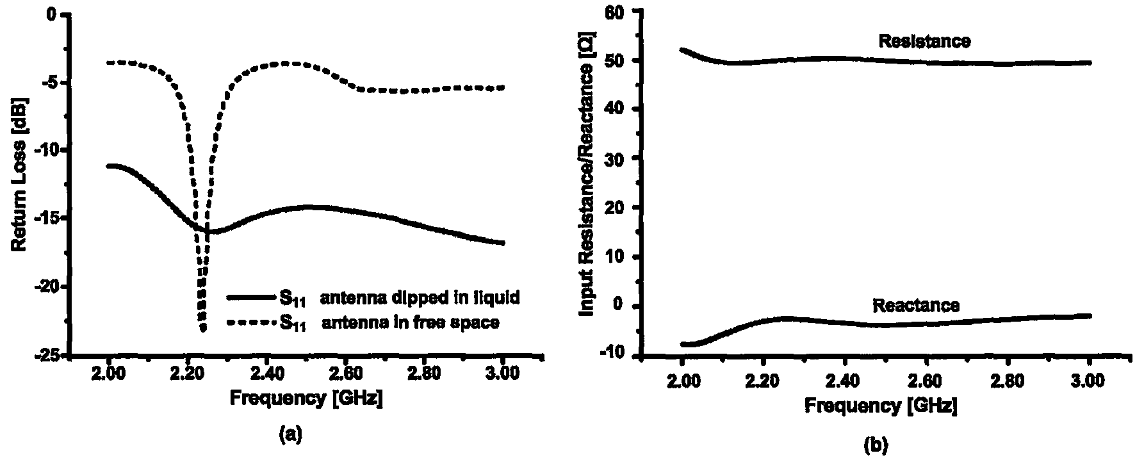

Fig. 8. 11. One-port measurements at 2.4 GHz: (a) return loss and (b) input impedance.

Figures 8.12 and 8.13 show the measurement results obtained by the 2-port measurements technique. Since the loop antenna itself is symmetric and is fed from its middle, one should expect S_{11} and S_{22} to be identical. However, in the practical case, there always exists some asymmetry in the measurement set-up, which caused S_{11} and S_{22} presented here to be different. However, the curves clearly show that the loop antenna is well matched to 50 Ω in the lossy medium at both frequencies. The calculated input resistances shown in Fig. 8.10 to 8.13 present the total antenna resistance, i.e. the radiation resistance and the loss resistance. To calculate R_{rad}, R_{ohmic} is estimated using (8.5). After estimating R_{ohmic}, the radiation efficiency can be calculated using (8.4).

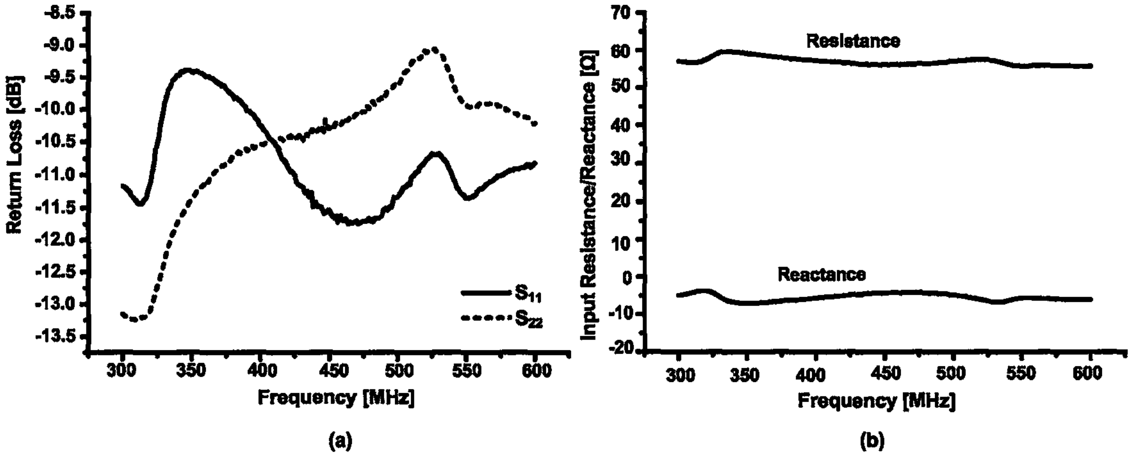

Fig. 8. 12. Two-port measurements at 405 MHz: (a) return loss and (b) input impedance.

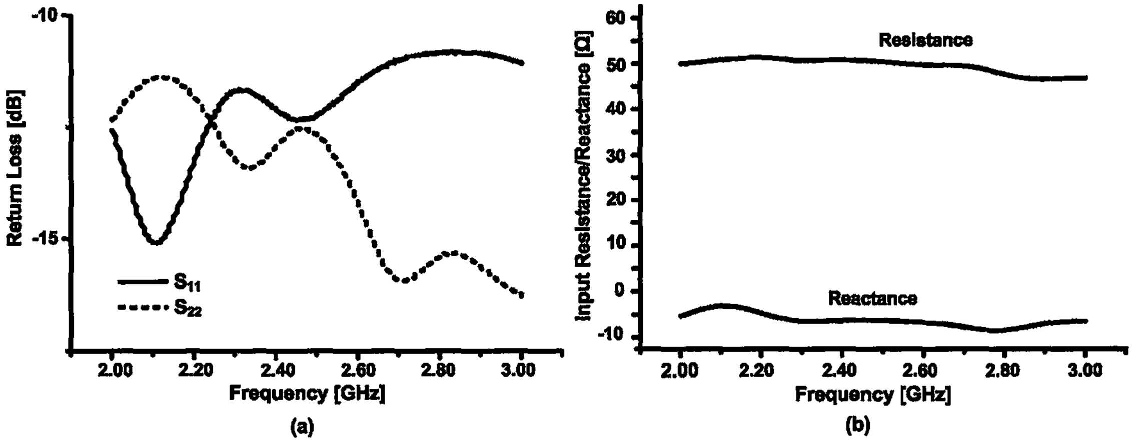

Fig. 8. 13. Two-port measurements at 2.4 GHz: (a) return loss and (b) input impedance.

8.5 SUMMARY

In this chapter, we investigated the suitability of loop antennas for in-body transceivers. The characteristics of loop antennas were developed in terms of their radiation resistance, radiation efficiency and transmitting bandwidth at the biomedical 402-405 MHz frequency band (MICS band). Also, their biocompatibility at 5 mW power feed was investigated by means of MoM numerical simulations. The SAR distribution in the body tissues surrounding the loop shows that these antennas comply well with the safety standards. Measurements were carried out at 405 MHz and at 2.4 GHz using in-house fabricated small loop antennas. Both, measurements and simulations show that, unlike in free space, physically small loop antennas in a highly dissipative medium such as the human body, are efficient radiators and provide sufficient transmission bandwidths. Hence, given that their physical structure is suitable for the application and they are of low weight and low cost, we conclude that loop antennas are good candidates for in-body transceivers. However, it should be noted that results presented here are only approximate guidelines. More detailed estimates require more complex phantoms and measurements set-ups.

CHAPTER 9

Conclusions and Future Work

9.1 SUMMARY

The primary goal of this work was to design, implement and test PAs and antennas suitable for deeply implanted biotelemetry systems. A major challenge was to meet the strict application requirements of such a wireless system, which are: high efficiency, low-power operation, small physical size and the compliance with the safety limits. Two frequency bands are suitable for operating this system, the 405-MHz MICS band and the 2.4-GHz ISM band. More specifically, the goal of this work was to investigate the operation of current-mode PAs and loop antennas at both frequency bands.

To meet the size requirement of the application, the whole transmitter has to be implemented in a standard CMOS process for full integration with the remaining subsystems. In the first part of this thesis, three fully integrated current-mode PA circuits have been designed and measured. The first PA was published in [88], it consists of two class AB stages and operates at 2.4 GHz. At 1.4 V supply, the circuit is capable of delivering 6.5 dBm of output power with a PAE of 28% and a current consumption of 11 mA. The second PA is similar to the first one in architecture and component values, however it was implemented using a thicker top metal layer and hence, showed a slightly improved performance. At the same supply, it delivers 7.2 dBm of output power with a PAE of 30.2% and a current consumption of 12 mA. The third PA operates at 405 MHz and has a single-stage class AB topology. At 1.4 V supply voltage, it provides 8 dBm of output power with a drain efficiency of 40% and 11 mA current consumption. Its PAE, however, is only 32.6% because of the reduced gain of the amplifier. The three circuits have demonstrated results that outperform previously published PA circuits. Thus, through this work it was shown that class AB PAs, if properly designed, are well-suited for biotelemetry applications and that between the two frequencies, the lower frequency is more suitable for the application, since it provides better efficiency performance.

Throughout the layout design stage of the first PA circuit, a need has been identified for a systematic layout design methodology that takes the layout parasitics into account. Thus, we have developed a simple layout design procedure that takes into account most of the high frequency parasitics arising from the layout of CMOS ICs. For verification of the usefulness of the approach, we have designed a 5-GHz LNA. The usefulness of the approach has been proven through the good match obtained between measurements and simulation. This approach allows for accurate prediction of the performance of the RF ICs, thus eliminating the need for iterative design and manufacture. At a current consumption of 3.8 mA, the designed LNA circuit has a gain of 10 dB and is matched to 50 Ω impedances at its input and output ($S_{11} \leq$ -9 dB and $S_{22} \leq$ -10 dB). This performance was achieved at a frequency of operation of 5 GHz and a supply voltage of 1.8 V. The proposed approach has also been applied to the layouts of the three PA circuits and was published in [89].

One last subject covered in this work was investigating the suitability of loop antennas for the use in biotelemetry implants. Analytical formulas, numerical simulations and measurements were carried out to characterize the radiation performance of in-body loop antennas in terms of their radiation resistance, transmitting bandwidth and biocompatibility at 405 MHz [90]. We have shown that at 405 MHz, implanted loop antennas are efficient over a wide band. Numerical simulations showed that at 5 mW power feed, the specific absorption rate (SAR) distribution in the vicinity of the implanted loop is well below the safety limits (< 1.6 W/kg) and hence, it complies with the human safety regulations. At 2.4 GHz, however, the antenna was only characterized using measurements, since at this frequency the antenna becomes electrically large and the simulations become unfeasible, since they require enormous computational resources. For measurement purposes, we prepared two chemical solutions that mimic the human body in its electrical properties at both frequencies. This work proves that small loop antennas are good candidates for in-body transceivers.

9.2 FUTURE WORK

The research work presented in this thesis has opened the way to several areas for future research and possible improvements on this work. For example, the operation of the PAs and the antenna were investigated in this work separately. A next step would be to bond the two blocks in a package and test their performance together, taking all the system design issues into account such as the matching between the stages, the use of a balun to transform from single-ended to differential input, etc. Regarding the latter issue, one might find that it is in fact preferable to realize a single-chip differential PA to feed the antenna differentially rather than using a balun, since the losses in the balun could be very significant. Furthermore, the suitability of the proposed layout design methodology can be applied on higher frequency designs and other circuit blocks to investigate its validity for a wider range of applications.

Also, since the application requires extremely low power consumption, alternative circuit design techniques and ultra-low voltage possibilities should be discovered, similar to what is reported in [91-93].

It was shown in this thesis that loop antennas are good candidates for in-body operation. An area for further research would be investigating the use of other candidate antennas such as mircostrip and slot antennas for the same application. Also, the numerical simulations of the antenna investigated in this thesis assumed a coarse representation of the human body as the radiation environment. To analyze the performance of implanted antennas more accurately, it is suggested that a more detailed tissue-segmented or semi-segmented model be used in the simulations. The FDTD technique is known to be capable of handling these simulations and is thus, a good numerical technique to be used in future work. Nevertheless, it should be noted that any numerical results, no matter how complicated the model used, are only best estimates and serve only as design guidelines.

Commercial wireless devices do not get approval from the regulating committees unless it is verified using experimental set-ups that these devices comply with the safety standards. Techniques to do these measurements are described in special documents [69].

For this reason, the investigation of the antenna would not be complete before the SAR is actually measured in a test environment that mimics the real situation.

To estimate the output power levels of the transmitter investigated in this thesis, we followed a simple power budget calculation. We started by assuming an output of 25 μW (-16 dBm) at the outer receiver, which is the maximum allowed value in free space according to the spectral regulations at the MICS band. Assuming the body losses to be 15-18 dB [13], the necessary output power was calculated to be in the range of few dBm. One last area that could be of interest for further research is characterizing the wireless transmission link from the implant to the outer receiver in greater detail, which was done here, using a rough calculation. This involves estimating the path losses through measurements.

APPENDIX A

Recipes for Tissue-Equivalent Liquids

This appendix gives the chemical ingredients that were used in preparation of the tissue-equivalent solutions used in the antenna measurements [69]. As mentioned in Chapter 7, these liquids are distinct for different frequencies. Table A.1 lists the ingredients used in the preparation of the 405-MHz solution and Table A.2 lists those used for the 2.4-GHz solution. The properties of the resulting solutions are given in Table A.3 [69]. The electrical properties of the prepared liquids were not measured relying on the fact that the recipes and the procedures were followed closely.

Table A. 1. Recipe for preparing the body-equivalent solution at 405 MHz [69].

Ingredient	Percentage by weight [%]
Deionized water	51.16
Salt (99^{+}% pure NaCl)	1.49
Sugar (98^{+}% pure Sucrose)	46.78
Hydroxyethyl Cellulose (HEC)	0.52
Bactericide (Sodium Azide)	0.05

Table A. 2. Recipe for preparing the body-equivalent solution at 2.4 GHz [69].

Ingredient	Percentage by weight [%]
Deionized water	73.2
Salt (99^{+}% pure NaCl)	0.04
Di-ethylene-glycol butyl ether (DGBE)	26.7

Table A. 3. Electrical parameters of the 405-MHz and the 2.4-GHz solutions [69].

	450 MHz	**2.45 GHz**
σ [S/m]	0.83	1.78
ε_r	58	52.5

In the measurements, we have prepared 20 liters of each solution. The following procedure was followed in preparing the 405-MHZ solution [86].

- For a volume of 20 liters, the mass of each of the ingredients is calculated assuming a density of 1000 kg/m^3.
- The water is heated to approximately 40 degrees Celsius.
- Appropriate quantities of salt and bactericide are prepared in separate containers.
- They are then added slowly to the water while stirring at a very low speed.
- After they are totally dissolved, the sugar is added slowly while stirring.
- After the sugar is totally dissolved, the HEC is added very slowly to avoid clumping.
- Stirring of the solution goes on until it thickens.

To prepare the 2.4-GHz solution, the following steps were followed.

- For a volume of 20 liters, the mass of each of the ingredients is calculated assuming a density of 1000 kg/m^3.
- The DGBE and the salt are added to the water and the solution is stirred for a short while. The DGBE is a liquid; hence it dissolves in water at no added heat.

APPENDIX B

Network Parameter Conversion Formulas

This appendix lists the formulas that were used to convert the measured *S*-parameters to the *Z*-parameters. These are given by [87]:

$$Z_{11} = Z_0 \frac{(1+S_{11})(1-S_{22})+S_{12}S_{21}}{\left[(1-S_{11})(1-S_{22})-S_{12}S_{21}\right]}, \tag{A.1}$$

$$Z_{12} = Z_0 \frac{2S_{12}}{\left[(1-S_{11})(1-S_{22})-S_{12}S_{21}\right]}, \tag{A.2}$$

$$Z_{21} = Z_0 \frac{2S_{21}}{\left[(1-S_{11})(1-S_{22})-S_{12}S_{21}\right]}, \text{ and} \tag{A.3}$$

$$Z_{11} = Z_0 \frac{(1+S_{22})(1-S_{11})+S_{12}S_{21}}{\left[(1-S_{11})(1-S_{22})-S_{12}S_{21}\right]}. \tag{A.4}$$

In the above equations, Z_0 is source characteristic impedance used in the *S*-parameter measurement, which is usually 50 Ω.

References

[1] A. Sivard, P. Bradley, P. Chadwick and H. Higgins, "The challenge of designing in-body communications," *Embedded Systems Programming*. Online: http://www.embedded.com/showArticle.jhtml?articleID=51200651.

[2] L. M. Brodsky, "Issues in emerging health technologies – wireless capsule endoscopy," *The Canadian Coordinating Office for Health Technology Assessment (CCOHTA)*, issue 53, Dec. 2003.

[3] D. G. Adler and C. J. Gostout, "Wireless capsule endoscopy," *Hospital Physician*, pp. 14-22, May 2003.

[4] D. Panescu, "Emerging technologies – an imaging pill for gastrointestinal endoscopy", *IEEE Engineering in Medicine and Biology Magazine*, pp. 12-14, July/Aug. 2005.

[5] "Wireless capsule endoscopy", Health Technology Literature Review prepared by the Medical Advisory Secretariat, Ministry of Health and Long-Term Care, Ontario, Canada, May 2003.

[6] P. Dario and R. Dillman, "Euron technology roadmaps", Apr. 2004.

[7] Endoscopic Capsule Norika System, RF System Lab., http://www.rfnorika.com.

[8] Online: www.dhpc.adelaide.edu.au/projects/vishuman2/VisibleHuman.html.

[9] "ERC recommendation 70-03 relating to the use of short range devices (SRD)," in *Conf. Eur. Postal Telecomm. Admin.*, CEPT/REC 70-03, Annex 12, Tromso, Norway, 1997.

[10] Code of Federal Regulations (CFR), USA, Title 47 Telecommunications, Part 95.601-95.673, Subpart E.
Online: http://www.access.gpo.gov/nara/cfr/waisidx_03/47cfr95_03.html.

[11] Online: http://wireless.fcc.gov/services/personal/medicalimplant/.

[12] J. R. Williams, "U.S. spectrum allocations 300-3000 MHz," *OPP/FCC*, Nov. 2002.

[13] W. G. Scanlon, B. Burns and N. E. Evans, "Radiowave propagation from a tissue-implanted source at 418 MHz and 916.5 MHz," *IEEE Transactions on Biomedical Engineering,* vol. 47, no. 4, pp. 527-534, Apr. 2000.

[14] A. A. Abidi, "RF CMOS comes of age," *IEEE Journal of Solid-State Circuits*, vol. 39, no. 4, pp. 549-561, Apr. 2004.

[15] H. Komurasaki, T. Sano, T. Heima, K. Yamamoto, H. Wakada, I. Yasui, M. Ono, T. Miwa, H. Sato, T. Miki and N. Kato, "A 1.8-V operation RF CMOS transceiver for 2.4-GHz-band GFSK applications," *IEEE Journal of Solid-State Circuits*, vol. 38, no. 5, pp. 817-825, May 2003.

[16] T. Melly A.-S. Porret, C. C. Enz and E. A. Vittoz, "An ultra low-power UHF transceiver integrated in a standard digital CMOS process: transmitter," *IEEE Journal of Solid-State Circuits*, vol. 36, no. 3, pp. 467-472, Mar. 2001.

[17] T. Melly, A-S. Porret, C. C. Enz, M. Kayal and E. Vittoz, "A 1.2 V, 430 MHz, 4 dBm power amplifier and a 25 μW front-end, using a standard digital CMOS process," *Proc. Low Power Electronics and Design Symp.*, pp. 233-237, 1999.

[18] P. Quinlan, P. Crowley, M. Chanca, M. Hudson, B. Hunt, K. Mulvaney, G. Retz, C. E. O'Sullivan and P. Walsh, "A multimode 0.3–200-kb/s transceiver for the 433/868/915-MHz bands in 0.25-μm CMOS", *IEEE Journal of Solid-State Circuits*, vol. 39, no. 12, pp. 2297-2310, Dec. 2004.

[19] M. M. El-Desouki, *Design of Integrated Power Amplifier Circuits for Biotelemetry Applications*, Master Thesis, Dept. of Electrical and Computer Engineering, McMaster University, Hamilton, Ontario, Jan. 2006.

[20] C. H. Diaz, D.D. Tang and J. Y. -C. Sun, "CMOS technology for MS/RF SoC," *IEEE Transactions on Electron Devices*, vol. 50, no. 3, pp. 557-566, Mar. 2003.

[21] J. J. Liou and F. Schwierz, "RF MOSFET: recent advances and future trends," *IEEE Conf. on Electron Devices and Solid-State Circuits,* pp. 185-192, Dec. 2003.

[22] 2003 Int. technology roadmap for semiconductors, Int. SEMATECH, Austin, TX. Online: http://public.itrs.net/Files/2003ITRS/Home2003.htm

[23] W. Liu, X. Jin, J. Chen, M-C. Jeng, Z. Liu, Y. Cheng, K. Chen, M. Chan, K. Hui, J. Huang, R. Tu, P. K. Ko and C. Hu, "BSIM3V3.2.2 MOSFET model users'

manual," Department of Electrical Engineering and Computer Sciences University of California, Berkeley, CA, 1999.

[24] C. Enz, "An MOS transistor model for RF IC design valid in all regions of operation," *IEEE Transactions on Microwave Theory and Techniques,* vol. 50, no. 1, part 2, pp. 342-359, Jan. 2002.

[25] Suet Fong Tin, A. A. Osman, K. Mayaram and C. Hu, "A simple subcircuit extension of the BSIM3v3 model for CMOS RF design," *IEEE Journal of Solid-State Circuits*, vol. 35, no. 4, pp. 612-624, Apr. 2000.

[26] M. J. Deen and T. A. Fjeldy, "Selected Topics in Electronics and Systems: CMOS RF Modeling, Characterization and Applications," *World Scientific Publishing, Singapore,* vol. 24, 409 pages, 2002.

[27] Yuhua Cheng, M. Jamal Deen and Chih-Hung Chen, "MOSFET Modeling for RFIC Design," *IEEE Transactions on Electron Devices (Special Issue on Integrated Circuit Technologies for RF Circuit Applications)*, vol. 52, no. 7, pp. 1286-1303, July 2005.

[28] "TSMC 0.18 μm mixed signal 1P6M salicide 1.8V/3.3V RF spice models," T-018-MM-SP-001, Dec. 2000.

[29] F. W. Grover, "Inductance calculations," *Princeton*, N. J.: Van Nostrand, 1946, reprinted by *Dover Publications*, New York, 1954.

[30] C. P. Yue, C. Ryu, J. Lau, T.H. Lee and S. S. Wong, "A physical model for planar spiral inductors on silicon," *Int. Electron Devices Meeting*, pp. 155-158, 1996.

[31] C. P. Yue and S. S. Wong, "Physical modeling of spiral inductors on silicon," *IEEE Transactions on Electron Devices*, vol. 47, no. 3, pp. 560-568, Mar. 2000.

[32] Z. Wang, M. J. Deen and A. Rahal, "Modeling of Integrated Inductors and Resistors for Microwave Applications in: Integrated Passive Component Technologies." R. K. Ulrich and L. W. Schapper, Chapter 11, pp. 247-291, *IEEE Press*, New York, ISBN 0-471-24331-7, 2003.

[33] J. M. Lopez-Villegas, J. Samitier, C. Cane, P. Losantos and J. Bausells, "Improvement of the quality factor of RF integrated inductors by layout optimization," *IEEE Transactions on Microwave Theory and Techniques*, vol. 48, no. 1, pp. 76-83, Jan. 2000.

[34] M. Danesh and J. R. Long, "Differentially driven symmetric microstrip inductors," *IEEE Transactions on Microwave Theory and Techniques*, vol. 50, no. 1, pp. 332-341, Jan. 2002.

[35] J. N. Burghartz, "Integrated multilayer RF passives in silicon technology," *Topical Meeting Silicon Monolithic Integrated Circuits in RF Systems*, pp. 141-147, Sep. 1998.

[36] M. C. Hsieh, Y. K. Fang, C. H. Chen, S. M. Chen and W. K. Yeh, "Design and fabrication of deep submicron CMOS technology compatible suspended high-Q spiral inductors," *IEEE Transactions on Electron Devices*, vol. 51, no. 3, pp. 324-331, Mar. 2004.

[37] Jun Zou, Chang Liu, D.R. Trainor, J. Chen, J. E. Schutt-Aine and P. L. Chapman, "Development of three-dimensional inductors using plastic deformation magnetic assembly (PDMA)," *IEEE Transactions on Microwave Theory and Techniques*, vol. 51, no. 4, pp. 1067-1075, Apr. 2003.

[38] Kyung-Wan Yu and M. F. Chang, "CMOS K-band LNAs design counting both interconnect transmission line and RF pad parasitics," *IEEE Symp. on Radio Frequency Integrated Circuits (RFIC)*, pp. 101-104, June 2004.

[39] Yu Cao, Xuejue Huang, D. Sylvester, Tsu-Jae King, and Chenming Hu, "Impact of on-chip interconnect frequency-dependent $R(f)L(f)$ on digital and RF design," *IEEE Transactions on Very Large Scale Integration (VLSI) Systems*, vol. 13, no. 1, pp. 158-162, Jan. 2005.

[40] Z. Wang, M. J. Deen and A. H. Rahal, in "Integrated passive component technology," *IEEE Press*, 2004.

[41] Steve C. Cripps, RF Power Amplifiers for Wireless Communications, *Artech House Publishers*, MA, 1999.

[42] A. Katz, "Linearization: reducing distortion in power amplifiers," *IEEE Microwave Magazine*, vol.2, no. 4, pp. 37-49, Dec. 2001.

[43] R. Gupta and D. J. Allstot, "Fully monolithic CMOS RF power amplifiers: recent advances," *IEEE Communications Magazine*, vol. 37, no. 4, pp. 94-98, Apr. 1999.

[44] I. Aoki, S. D. Kee, D. B. Rutledge and A. Hajimiri, "Fully integrated CMOS power amplifier design using the distributed active-transformer architecture," *IEEE Journal of Solid State Circuits*, vol. 37, no. 3, pp. 371-383, Mar. 2002.

[45] Y. Ding and R. Harjani, "A CMOS high efficiency +22 dBm linear power amplifier," *Proc. IEEE Custom Integrated Circuits Conf.*, pp. 557-560, Oct. 2004.

[46] P. Baoureis, H. Hein, M. Peter and F. Oehler, "A Fully Integrated 0.35-µm CMOS MMIC Amplifier for Short Range 433 MHz ISM Band Transceiver Applications," *Proc. Int. Conf. Microelectronics*, vol. 2, pp. 589-592, May 2004.

[47] Y. Eo and K. Lee, "A Fully Integrated 24-dBm CMOS Power Amplifier for 802.11a WLAN Applications," *IEEE Microwave and Wireless Components* Letters, vol. 14, no. 11, pp. 504-506, Nov. 2004.

[48] Y. H. Chee, J. Rabaey and A. M. Niknejad, "A Class A/B Low Power Amplifier for Wireless Sensor Networks," *Proc. IEEE Int. Sym. on Circuits and Systems*, vol. 4, pp. 409-412, May 2004.

[49] A. Zolfaghari and B. Razavi, "A Low-Power 2.4-GHz Transmitter/Receiver CMOS IC," *IEEE Journal of Solid State Circuits*, vol. 38, no. 2, pp. 176-183, Feb. 2003.

[50] T. H. Lee and S. S. Wong, "CMOS RF integrated circuits at 5 GHz and beyond," *Proc. of the IEEE*, vol. 88, no. 10, pp. 1560-1571, Oct. 2000.

[51] S. J. Yoo, H. J. Ahn, M.M. Hella and M. Ismail, "The design of 433 MHz class AB CMOS power amplifier," *Southwest Sym. Mixed-Signal Design*, pp. 36-40, Feb. 2000.

[52] T. Melly, A. -S. Porret, C. C. Enz, M. Kayal and E. Vittoz, "A 1.2 V, 430 MHz, 4 dBm Power Amplifier and a 250 µW Front-End, using a Standard Digital CMOS Process," *Proc. Int. Sym. on Low Power Electronics and Design*, pp. 233-237, Aug. 1999.

[53] K. Yamamoto, T. Heima, A. Furukawa, M. Ono, Y. Hashizume, H. Komurasaki, S. Maeda, H. Sato and N. Kato, "A 2.4-GHz-band 1.8-V operation single-chip Si-CMOS T/R-MMIC front-end with a low insertion loss switch," *IEEE JOURNAL Solid-State Circuits*, vol. 36, (8), pp. 1186-97, Aug. 2001.

[54] P. B. Khannur, "A CMOS Power Amplifier with Power Control and T/R Switch for 2.45-GHz Bluetooth/ISM Band Applications," *Proc. IEEE Radio Frequency Int. Circuits Sym.*, pp. 145-148, June 2003.

[55] K. Fukunaga, S. Watanabe and Y. Yamanaka, "Time dependence of dielectric properties of tissue-equivalent dielectric liquid materials" *Proc. Int. Symp. on Electrets*, pp. 92-95, Oct. 2002.

[56] C. Gabriel and S. Gabriel, "Compilation of the dielectric properties of body tissues at RF and microwave frequencies," *Armstrong Lab.*, 1996. Online: http://www.brooks.af.mil/AFRL/HED/hedr/reports/dielectric/home.html. Online Applet: http://niremf.ifac.cnr.it/tissprop/htmlclie/htmlclie.htm.

[57] C. Gabriel, S. Gabriel and E. Corthout, "The electric properties of biological tissues: I. Literature survey," *Phys. Med. Biol.*, vol. 41, no. 11, pp. 2231-2249, 1996.

[58] S. Gabriel, R. W. Lau and C. Gabriel, "The electric properties of biological tissues: II. Measurements in the frequency range 10 Hz to 20 GHz," *Phys. Med. Biol.*, vol. 41, no. 11, pp. 2251-2269, 1996.

[59] S. Gabriel, R. W. Lau and C. Gabriel, "The electric properties of biological tissues: III. Parametric models for the dielectric spectrum of tissues," *Phys. Med. Biol.*, vol. 41, no. 11, pp. 2271-2293, 1996.

[60] P. A. Mason, W. D. Hurt, T. J. Walters, J. A. D'Andrea, P. Gajsek, K. L. Ryan, D. A. Nelson, K. I. Smith and J. M. Ziriax, "Effects of frequency, permittivity, and voxel size on predicted specific absorption rate values in biological tissue during electromagnetic-field exposure," *IEEE Transactions on Microwave Theory and Techniques,* vol. 48, no. 11, part 2, pp. 2050-2058, Nov. 2000.

[61] *IEEE Standard for Safety Levels with Respect to Human Exposure to Radio Frequency Electromagnetic Fields, 3 kHz to 300 GHz*, IEEE Standard C95.1-1999, 1999.

[62] E. R. Adair and R. C. Petersen, "Biological effects of radio-frequency/microwave radiation," *IEEE Transactions on Microwave Theory Tech.*, vol. 50, no. 3, pp. 953-962, Mar. 2002.

[63] O. P. Gandhi, "Biological effects and medical applications of RF electromagnetic fields," *IEEE Transactions on Microwave Theory and Techniques,* vol. 82, no.11, pp. 1831-1847, Nov. 1982.

[64] P. Bernardi, M. Cavagnaro, S. Pisa and E. Piuzzi, "Specific absorption rate and temperature elevation in a subject exposed in the far-field of radio-frequency sources operating in the 10-900-MHz range," *IEEE Transactions on Biomedical Engineering,* vol. 50, no. 3, pp. 295-304, Mar. 2003.

[65] C. H. Durney, H. Massoudi and M. F. Iskandaer, *Radiofrequency Radiation Dosimetry Handbook*, 4th ed. Brooks AFB, TX: USAF School Aerosp. Med., 1986.

[66] T. Williams and D. Riley, "Standards for the management of potential health risks of EM fields," Online: http://64.70.157.146/archive/old_archive/031124.htm.

[67] T. Person and C. Tornevik, "Mobile communications and health," *Ericsson Review*, no. 2, pp. 48-55, 2003.

[68] C. Gabriel, "Phantom models for antenna design and exposure assessment," *IEE Colloquium on Design of Mobile Handset Antennas for Optimal Performance in the Presence of Biological Tissue*, pp. 6/1-6/5, Jan. 1997.

[69] D. L. Means and K. W. Chan, "Evaluating compliance with FCC guidelines for human exposure to radiofrequency electromagnetic fields," *Federal Communications Commission, Office of Engineering and Technology,* Supplement C (Edition 01-01) to OET Bulletin 65 (Edition 97-01), June 2001.

[70] M. R. Tofighi and A. S. Daryoush, "Characterization of biological tissues up to millimeter wave: test fixture design," *Int. IEEE Microwave Symp. MTT-S,* vol. 2, pp. 1041-1044, June 2000.

[71] P. Soontornpipit, C. M. Furse and You Chung Chung "Design of implantable microstrip antenna for communication with medical implants," *IEEE Transactions on Microwave Theory and Techniques,* vol. 52, no. 8, part 2, pp. 1944-1951, Aug. 2004.

[72] *Electromagnetic compatibility and radio spectrum matters (ERM); Radio equipment in the frequency range 402 MHz to 405 MHz for Ultra Low Power Active Medical Implants and Accessories; Part 1: Technical characteristics,*

including electromagnetic compatibility requirements, and test methods, final draft, ETSI EN 301 839-1 V.1.1.1, European standard telecommunications series, 2002-04.

[73] K. Jaehoon and Y. Rahmat-Samii, "Implanted antennas inside a human body: simulations, designs, and characterizations," *IEEE Transactions on Microwave Theory and Techniques,* vol. 52, no. 8, part 2, pp. 1934-1943. Aug. 2004.

[74] *The Visible Human Project*, United States National Library of Medicine, National Institute of Health.

[75] P. J. Dimbylow, "FDTD calculations of the whole-body averaged SAR in an anatomically realistic voxel model of the human body from 1 MHz to 1 GHz," *Phys. Med. Biol.*, vol. 49, pp. 479-490, 1997.

[76] G. Smith, "On the electrically small loop antenna in a dissipative medium," *IEEE Transactions on Antennas and Propagation,* vol. 24, no. 4, pp. 533-537, July 1976.

[77] J Wang and O. Fujiwara, "Modeling of electromagnetic interference to an implanted cardiac pacemaker due to mobile phones," *IEEE Int. Symp. on Electromagnetic Compatibility,* vol. 1, pp. 209-212, Aug. 2000.

[78] W. G. Scanlon, N. E. Evans and J. B. Burns, "FDTD analysis of close-coupled 418 MHz radiating devices for human telemetry," *Phys. Med. Biol.*, vol. 44, pp. 335-345, 1999.

[79] K. Gosalia, G. Lazzi and M. Humayun, "Investigation of a microwave data telemetry link for a retinal prosthesis," *IEEE Transactions on Microwave Theory and Techniques,* vol. 52, no. 8, part 2, pp. 1925-1933, Aug. 2004.

[80] L. C. Chirwa, P. A. Hammond, S. Roy and D. R. S. Cumming, "Electromagnetic radiation from ingested sources in the human intestine between 150 MHz and 1.2 GHz," *IEEE Transactions on Biomedical Engineering,* vol. 50, no. 4, pp. 484-492, Apr. 2003.

[81] W. G. Scanlon, N. E. Evans and Z. M. McCreesh, "RF performance of a 418-MHz radio telemeter packaged for human vaginal placement" *IEEE Transactions on Biomedical Engineering*, vol. 44, no. 5, pp. 427-430, May 1997.

[82] G. Smith, "Radiation efficiency of electrically small multiturn loop antennas," *IEEE Transactions on Antennas and Propagation,* vol. 20, no. 5, pp. 656-657, Sep. 1972.

[83] G. S. Smith, "Proximity effects in systems of parallel conductors," *Journal of Applied Physics*, vol. 43, no. 5, pp. 2196-2203, May 1972.

[84] A. D. Yaghjian and S. R. Best, "Impedance, bandwidth and Q of Antennas," *IEEE Transactions on Antennas and Propagation*, vol. 53, no. 4, pp. 1298-1324, Apr. 2005.

[85] EM Software and Systems – S. A. (Pty) Ltd. Online: http://www.feko.info/

[86] *Tissue Recipe and Calibration Requirements: Part of SAR Measurements Requirements SSI/DRB-TP-D01-030*, Spectrum Sciences Institute RF Dosimetry Research Board, Mar. 1998.

[87] D. M. Pozar, *Microwave Engineering*. Amherst, MA: Wiley, 1998.

[88] S. M. Abdelsayed, M. J. Deen and N. K. Nikolova, "A Fully-integrated low-power CMOS power amplifier for biomedical applications", *Proc. of the European Microwave Conf.*, pp. 1715-1718, Oct. 2005.

[89] S. M. Abdelsayed, M. J. Deen and N. K. Nikolova, "Parasitics-aware layout design of a low-power fully-integrated CMOS power amplifier", *Journal of Vacuum Science and Technology A (Special Issue for CSTC 2005)*, vol. A24, no. 3, In Press, May/June 2006.

[90] S. M. Abdelsayed, N. K. Nikolova and M. J. Deen, "Radiation characteristics of loop antennas for biomedical implants", *Proceeding of the XXVIIIth General Assembly of the Int. Union of Radio Science CDROM*, Oct. 2005.

[91] H. M. Jafari, W. Liu, S. Hranilovic and M. J. Deen, "Ultra-Wideband (UWB) Radar Imaging System for Biomedical Applications," *Journal of Vacuum Science and Technology A (Special Issue for CSTC 2005)*, vol. A24, no. 3, In Press, May/June 2006.

[92] M. J. Deen, S. Naseh, O. Marinov and M. H. Kazemeini, "Very Low-Voltage Operation Capability of CMOS Ring Oscillators and Logic Gates," *Journal of Vacuum Science and Technology A (Special Issue for CSTC 2005)*, vol. A24, no. 3, In Press, May/June 2006.

[93] M. J. Deen, R. Murji, A. Fakhr, N. Jafferali and W. L. Ngan, "Low Power CMOS Integrated Circuits for Radio Frequency Applications," *IEE Proc. - Circuits, Devices and Systems,* vol. 152, no. 5, pp. 502-508, Oct. 2005.